ISSN : 2372-0484

AIMS Materials science

Volume No. 12
Issue No. 2
May - August 2025

ENRICHED PUBLICATIONS PVT. LTD

S-9, IInd FLOOR, MLU POCKET,
MANISH ABHINAV PLAZA-II, ABOVE FEDERAL BANK,
PLOT NO-5, SECTOR-5, DWARKA, NEW DELHI, INDIA-110075,
PHONE: - + (91)-(11)-47026006

·ISSN : 2372-0484

AIMS Materials science

AIM AND SCOPE

AIMS Materials science is an international journal devoted to publishing peer-reviewed, high quality, original papers in the field of Materials science. We publish the following article types: original research articles, reviews, editorials, letters, and conference reports.

AIMS Materials Science welcomes, but not limited to, the papers from the following topics:

- Biological materials
- Ceramics
- Composite materials
- Magnetic materials
- Medical implant materials
- New properties of materials
- Nanoscience and nanotechnology
- Polymers
- Thin films

·ISSN : 2372-0484

Editor in Chief

Qing Hua Qin Department of Engineering, Shenzhen MSU-BIT University, 1 International University Park Road, Longgang, Shenzhen, Guangdong, 518172, China	**Bo Tang** Shandong Normal University, 88 East Wenhua Road, Jinan, Shandong, China

Founding Editor in Chief

Yaroslava G. Yingling
Department of Materials Science and Engineering, North Carolina State University,
Campus Box 7907, Raleigh, NC 27695-7907, USA

Managing Editor

Dr. Xu Guo
Managing and Operation (Journal)

Editorial Board

Maria Antonietta Aiello Department of Engineering for Innovation, University of Salento, 73100 Lecce, Italy	**Indika U. Arachchige** Department of Chemistry, Virginia Commonwealth University, United States
Mario Beiner Fraunhofer Institute for Microstructure of Materials and Systems IMWS, Walter-Hülse-Str. 1, 06120 Halle (Saale), Germany	**J. Paige Buchanan** US Army Corps of Engineers, Engineering Research and Development Center, Vicksburg, MS, USA
Detlef Bahnemann Institut fuer Technische Chemie, Gottfried Wilhelm Leibniz Universitaet Hannover, Callinstrasse 3, D-30167, Hannover, Germany; Saint-Petersburg State University, Ulyanovskaya str. 1, Peterhof, Saint-Petersburg, 198504, Russia	**Kaiyong Cai Key** Laboratory of Biorheological Science and Technology, Ministry of Education, College of Bioengineering, Chongqing University, Chongqing, 400044, China
Miguel A. Camblor Instituto de Ciencia de Materiales de Madrid, ICMM-CSIC, Sor Juana Inés de la Cruz, 3, 28039 Madrid, Spain	**Surojit Chattopadhyay** Institute of Biophotonics, National Yang Ming University, Taipei-112, Taiwan
Daolun Chen Department of Mechanical and Industrial Engineering, Ryerson University, 350 Victoria Street, Toronto, Ontario M5B 2K3, Canada	**Jian Chen** Department of Chemistry, Western University, 1511 Richmond Street, London, ON, N6A 5B7, Canada
Chong Cheng Department of Chemical and Biological Engineering, University at Buffalo, The State University of New York Buffalo, NY 14260-4200, USA	**Phillip Y. K. Choi** Donadeo Innovation Centre for Engineering, Department of Chemical & Materials Engineering, University of Alberta, Edmonton, Alberta, T6G 1H9, Canada
Amitava Choudhury Department of Chemistry, Missouri S & T, Rolla, MO 65409, USA	**John D. Clayton** Impact Physics Department, RDRL-WMP-C, US ARL Aberdeen Proving Ground, MD 21005-5066, USA
Pantaleo Davide Cozzoli Department of Mathematics and Physics, University of Salento, Via Arnesano-73100 Lecce, Italy; CNR NANOTEC-Institute of Nanotechnology, c/o campus Ecotekne, Via Monteroni-73100 Lecce, Italy	**A. Cremades** Departamento de Física de Materiales, Facultad de Ciencias Físicas, Universidad Complutense de Madrid, 28040 Madrid, Spain
Giuseppe Cruciani Department of Physics and Earth Sciences, University of Ferrara, Via Saragat 1, Bld B Room 209, I-44122 Ferrara, Italy	**NilY R. Dan** Chemical and Biological Engineering, Drexel University, 3141 Chestnut St., Philadelphia, PA 19104, USA

·ISSN : 2372-0484

Darren Sun Delai School of Civil and Environmental Engineering, Nanyang Technological University, Singapore 639798, Singapore	**Yubin Dong** College of Chemistry, Chemical Engineering and Material Science, Shandong Normal University, China
Antonio Facchetti Department of Chemistry and the Materials Research Center, Northwestern University, 2145 Sheridan Road, Evanston, IL 60208-3113, USA	**Chunhai Fan** Shanghai institute of applied physics, University of Chinese Academy of Sciences, China
Te-Hua Fang Department of Mechanical Engineering, National Kaohsiung University of Science and Technology, Kaohsiung 807, Taiwan	**Paulina Faria** Department of Civil Engineering, NOVA School of Science and Technology, Universidade NOVA de Lisboa, 2829-516 Caparica, Portugal
Peter Fischer Center for X-ray Optics, Lawrence Berkeley National Laboratory, 1 Cyclotron Road, Berkeley, CA 94720, USA	**Ines Flores-Colen** Construction Section, Department of Civil Engineering, Architecture and Georesources, Instituto Superior Técnico, University of Lisbon, Avenue Rovisco Pais, Lisbon 1049-001, Portugal
Francisco Gallego-Gómez Instituto de Ciencia de Materiales de Madrid, C/Sor Juana Inés de la Cruz 3, 28049 Madrid, Spain	**Xiaonan Gao** College of Chemistry, Chemical Engineering and Materials Science, Shandong Normal University, Jinan, Shandong, China
Elhem Ghorbel Université de Cergy Pontoise, 5 Mail Guy Lussac Neuville sur Oise, 95031 Cergy Pontoise Cedex, France	**Juan Cabanillas Gonzalez** Madrid Institute for Advanced Studies in Nanoscience, IMDEA Nanociencia, Calle Faraday 9, Ciudad Universitaria de Cantoblanco, 28049 Madrid, Spain
Fabrizio Greco Department of Civil Engineering, University of Calabria, 87036 Rende, Cosenza, Italy	**Anders Hagfeldt** Department of Physical and Analytical Chemistry, Uppsala University, Box 259, 75105 Uppsala, Sweden
Yang Han Harbin Engineering University, Nantong street, Nangang Distrit, Harbin, Heilongjiang, China	**Anming Hu** Department of Mechanical, Aerospace and Biomedical Engineering, University of Tennessee, 509 Dougherty Engineering Building, Knoxville, TN 37996-2210, USA
Xiaodong Huang Faculty of Science, Engineering and Technology, Swinburne University of Technology, Hawthorn, VIC 3122, Australia	**Christoph Janiak** Institut für Anorganische Chemie und Strukturchemie, Universitaet Duesseldorf, Universitaetsstrasse, D-40225 Düsseldorf, Germany
Animesh Jha The Institute for Materials Research, University of Leeds, Leeds, LS2 9JT, UK	**Yang Jiao** Materials Science and Engineering, School for Engineering and Matter, Transport and Energy, Arizona State University, Tempe, AZ 85287-6106, USA
Andrey P. Jivkov School of Mechanical, Aerospace and Civil Engineering (MACE), The University of Manchester (UoM), Oxford Road, Manchester M13 9PL, UK	**Kourosh Kalantar-zadeh** School of Engineering, RMIT University, Melbourne, VIC 3000, Australia
Susan M. Kauzlarich Department of Chemistry, University of California, One Shields Ave, Davis, California 95616, United States	**Guido Kickelbick** Inorganic Solid State Chemistry, Saarland University, Am Markt Zeile 3, 66125 Saarbrücken, Germany
Ji-Seon Kim Department of Physics & Centre for Plastic Electronics, Imperial College London, London SW7 2AZ, United Kingdom	**Khalid Lamnawar** Department of Mechanical Engineering, University of Lyon, 20 Avenue A. Einstein, F-69621 Villeurbanne, France

Yong Lei Fachgebietsleiter (Head), Fachgebiet 3D-Nanostrukturierung (Chair of 3D-Nanostructuring), Institute of Physics, Faculty of Mathemat-ics and Nature Sciences, Technical University of Ilmenau (Technische Universität Ilmenau), Germany	**Dawen Li** Electrical & Computer Engineering, Box 870286, University of Alabama, Tuscaloosa, AL 35487-0286, USA
Ping Li College of Chemistry, Chemical Engineering and Materials Science, Shandong Normal University, Jinan 250014, China	**Sean Li** School of Materials Science and Engineering, The University of New South Wales, Sydney, NSW 2052, Australia
Dongsheng Liu Department of Chemistry, Tsinghua University, China Kaohsiung 807, Taiwan	**Zhuang Liu** Functional Nano & Soft Materials Laboratory, Soochow University, China
Lin Liu Department of Materials Science and Engineering and State Key Lab for Materials Processing and Die & Mould Technology, Huazhong University of Science and Technology, Wuhan 430074, China	**Altino Loureiro** Department of Mechanical Engineering, University of Coimbra, Pinhal de Marrocos, 3030- 788 Coimbra, Portugal
It-Meng (Jim) Low Department of Imaging & Applied Physics, Curtin University, GPO Box U1987, Perth, WA 6845, Australia	**Enzo Martinelli** Department of Civil Engineering, University of Salerno, Via Giovanni Pallo II, 132 84084 Fisciano (SA), Italy
Tullio Monetta Department of Chemical Engineering, Materials and Industrial Production, University of Napoli Federico II, Piazzale Tecchio 80, 80125 Napoli, Italy	**Klaus Müllen** Max Planck Institute for Polymer Research Ackermannweg 10, D-55128 Mainz ,Germany
Franck Natali School of Chemical and Physical Sciences , Victoria University, Wellington, New Zealand	**Manashi Nath** Department of Chemistry, Missouri University of Science and Technology, Rolla, Missouri 65409, United States
Phuong Nguyen-Tri Department of Chemistry, Biochemistry and Physic, University of Quebec in Trois-Rivières, Québec, Canada	**Shigenobu Ogata** Department of Mechanical Science and Bioengineering, Graduate School of Engineering Science, Osaka University, Osaka 560-8531, Japan
Amir Pakdel School of Chemistry, University College Dublin (UCD), Belfield, Dublin, Ireland	**Dario Pasini** Department of Chemistry, University of Pavia, Via Taramelli, 10-27100, Pavia, Italy
Daiwen Pang College of Chemistry and Molecular Sciences, Wuhan University, China	**Srikanth Patala** Department of Materials Science and Engineering, North Carolina State University, 911 Partners Way, Engineering Building I, Room 3002, Raleigh, NC 27606, USA
Andrey P. Jivkov School of Mechanical, Aerospace and Civil Engineering (MACE), The University of Manchester (UoM), Oxford Road, Manchester M13 9PL, UK	**Kourosh Kalantar-zadeh** School of Engineering, RMIT University, Melbourne, VIC 3000, Australia
Durga Paudyal Division of Materials Sciences and Engineering, The Ames Laboratory, US Department of Energy, Iowa State University, Ames, IA 50011-3020, USA	**Jian Pei** College of Chemistry and Molecular Engineering, Peking University, China
Yong Pei Department of Chemistry, Xiangtan University, China	**Russo Pietro** Institute for Polymers, Composites and Biomaterials of National Research Council, Via Campi Flegrei 34, 80078 Pozzuoli, NA, Italy

·ISSN : 2372-0484

Gustavo Portalone Department of Chemistry, 'La Sapienza' University of Rome, 00185 Rome, Italy	**Sandipan Pramanik** Department of Electrical and Computer Engineering, University of Alberta, Canada
Faxiang Qin 1D Nanomaterials Group, National Institute for Materials Science, 1-2-1 Sengen, Tsukuba, Ibaraki 305-0047, Japan	**Bhakta B. Rath** US Naval Research Laboratory, Washington, DC 20375-5341, USA
Mauro Ricotta Department of Industrial Engineering, University of Padova, Italy	**Evgeny Rebrov** School of Engineering, University of Warwick, Library Road, CV4 7AL, Coventry, UK
Tomasz Sadowski Department of Solid Mechanics, Lublin University of Technology, 20-865 Lublin, Nadbystrzycka 40 Str., Poland	**Jacobo Santamaria** Applied Physics Department, Universidad Complutense de Madrid, Campus Moncloa, Madrid, 28040, Spain
Hua Song Department of Chemical and Petroleum Engineering, University of Calgary, 2500 University Drive, NW, Calgary, Alberta T2N 1N4, Canada	**Hélder Almeida Santos** Division of Pharmaceutical Technology, Faculty of Pharmacy, University of Helsinki, FI-00014, Finland
Atsushi Shishido Chemical Resources Laboratory, Tokyo Institute of Technology, R1-12, 4259 Nagatsuta, Midori-ku, Yokohama 226-8503, Japan	**Adam Z. Stieg** California NanoSystems Institute, University of California, Los Angeles, CA 90095, USA
Xuping Sun College of Chemistry, Sichuan University, China	**Mukundan Thelakkat** Applied Functional Polymers, Macromolecular Chemistry I, University of Bayreuth, 95440 Bayreuth, Germany
Alexander Umantsev Department of Chemistry/Physics, Fayetteville State University, Fayetteville, NC 28301, USA	**Kalman Varga** Department of Physics and Astronomy, Vanderbilt University, Nashville, USA
Pasquale Vena Department of Chemistry, Materials and Chemical Engineering, Giulio Natta, Laboratory of Biological Structure Mechanics (LaBS), Politecnico di Milano, Piazza Leonardo da Vinci, 32-20133 Milano, Italy	**Hao Wang** Institute of Metal Research, Chinese Academy of Sciences, Shenyang 110016, China
Qiang (David) Wang Department of Chemical and Biological Engineering and School of Biomedical Engineering, Colorado State University, USA	**Haiming Wen** Department of Physics, Nuclear and Electrical Engineering, Idaho State University, Idaho Falls, ID 83402, USA
Yiquan Wu Kazuo Inamori School of Engineering, New York State College of Ceramics, Alfred University, 2 Pine Street, Alfred, NY 14802-1296, USA	**Yu-Fei Wu** School of Engineering, RMIT University, 376-392 Swanston St, Melbourne GPO Box 2476V, Melbourne VIC 3001, Australia
Kai Xiao Center for Nanophase Materials Sciences, Oak Ridge National Laboratory, Bldg 8610, MS-6494, Oak Ridge, TN 37831-6494, USA	**Jun Yan** College of Material Science and Chemical Engineering, Harbin Engineering University, China
Yonggang Yang Department of Polymer Science and Engineering, College of Chemistry, Chemical Engineering and Materials Science, Soochow University, Suzhou 215123, China	**Bin Zhang** Department of Chemistry, Tianjin University, China

·ISSN : 2372-0484

AIMS Materials science

(Volume No. 12, Issue No. 2, May - August 2025)

Contents

·ISSN : 2372-0484

Molecular modeling studies of peptoid polymers

Laura J. Weiser and Erik E. Santiso *
Department of Chemical and Biomolecular Engineering, NC State University,
Campus Box 7905, Raleigh, NC 27695-7905, United States

ABSTRACT

Peptoids, or poly-N-substituted glycines, are synthetic polymers composed of a protein backbone with side chains attached to the nitrogen atoms rather than the α-carbons. Peptoids are biomimetic and protease resistant and have been explored for a variety of applications including pharmaceuticals and coatings. They are also foldamer-type materials that can adopt diverse structures based on the sequences of their side chains. Design of new peptoid sequences may lead to the creation of many interesting materials. Given the large number of possible peptoid side chains, computer models predicting peptoid structure-side chain relationships are desirable. In this paper, we provide a survey of computational efforts to understand and predict peptoid structures. We describe simulations at several levels of theory, along with their assumptions and results. We also discuss some challenges for future peptoid computational research.

Keywords: peptoids; foldamer; molecular simulation; biomimetic

Abbreviations

AMBER	Assisted Model Building with Energy Refinement
B3LYP	Becke, 3-parameter, Lee-Yang-Parr hybrid functional
CHARMM	Chemistry at Harvard Macromolecular Mechanics
BCC	Bond-Centered Charges
CD	Circular Dichroism
GAFF	General AMBER Force Field
GBSA	Generalized Born Surface Area implicit solvent model
HF	Hartree-Fock
IEFP	CM Integral Equation Formalism for the Polarizable Continuum Model
MF-CG-TOID	Molecular Foundry Coarse-Grained Peptoid model
MFTOID	Molecular Foundry Peptoid Force Field
Mp2	Møller-Plesset perturbation theory
NMR	Nuclear Magnetic Resonance spectroscopy
PCM	Polarizable Continuum Model
PPI	Helix Polyproline type I Helix
PPII	Helix Polyproline type II Helix
REMD	Replica Exchange Molecular Dynamics

1. Introduction

Peptoids are synthetic, protein-like polymers composed of poly-glycine backbones with side chains attached to their backbone nitrogen atoms [1,2] (See Figure 1). Peptoids are protease resistant and biocompatible and can be designed to mimic peptides [3], diffuse through membranes [4], and bind biological targets [5]. They have potential applications as drug molecules [6], antimicrobials [7], lung surfactants [8], and catalysts [9]. Peptoids can be synthesized with specific sequences in a step by-step approach. Their synthesis, applications, and experimental characterizations have been extensively reviewed elsewhere [1,2].

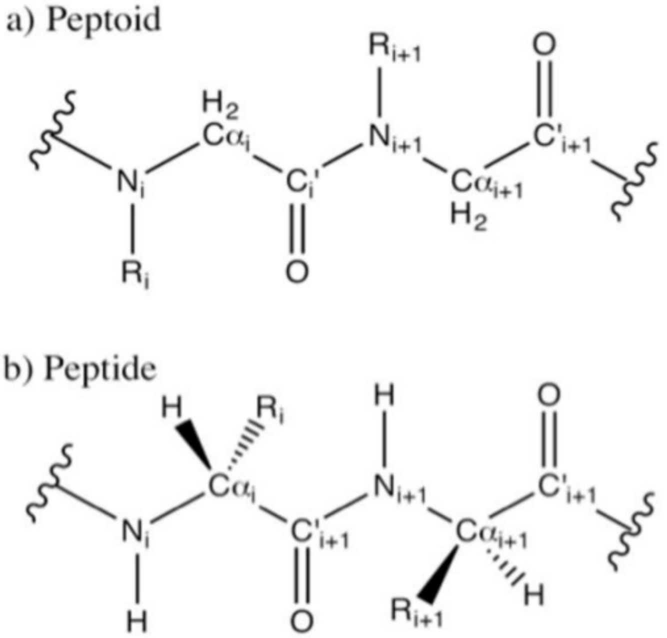

Figure 1. A Peptoid (a) and a peptide (b) Peptoids and peptides share the same backbone, but peptoids have side chains attached to their nitrogen atoms. This removes backbone chirality and backbone hydrogen bonding capability. The repeat unit of the peptoid backbone resembles the amino acid glycine, with a side chain replacing the nitrogenbound hydrogen atom. Due to this, peptoids are also called poly-N-substituted glycin

Peptoids are a kind of foldamer [10], i.e., linear polymers that fold into diverse 3D structures depending on the sequence of their attached side chains—just as amino acids combine to yield a diverse library of proteins. Single peptoid chains have been shown to adopt ordered structures including polyproline type I helices (PPI) [11], polyproline type II helices (PPII) [12], a threaded loop [13], flat “ribbons” [14] and “Σ-strands” [15], which are shown in Figure 2. Groups of peptoid chains can further self-assemble into nanostructures including microspheres [16], superhelices [17], and thin, bilayered nanosheets [18]. The chief focuses of this review are simulation studies that enhance our understanding of peptoids as foldamers, i.e., those studies that describe the relation between side chains and backbone conformations.

As researchers attempt to develop peptoids into useful materials, a key challenge is identifying side chains, and combinations of side chains, that drive backbone folding in a predictable way. This challenge is closely related to the well-known protein folding problem [19], whereby researchers aspire to predict folded protein structures from sequences of amino acids. Peptoid researchers have mainly approached this problem by identifying side chains expected to exert local structural preferences through sterics [11,12], electrostatics [20], hydrogen bonding [21], or n–π* bonding [22].These candidates are then synthesized into peptoid polymers and characterized using experimental methods such as X-ray crystallography [23], circular dichroism [24], and NMR [25]. Molecular modeling has played a prominent role in understanding the folding behavior of peptoids. Modeling studies have helped characterize and even predict some of the structures described above. Given the large number of possible peptoid side chains (potentially synthesized from over 300 commercially available primary amines [2]), and thus the astronomical number of possible combinations of side chains, molecular simulations will continue to play a crucial role in peptoid development, and will benefit from the extensive body of work devoted to the protein folding problem. Computational approaches to the protein folding problem consist of methods, models, and algorithms that read in amino acid sequences and return 3-D structure predictions. These predictions can be based on physical, force field models with parameters derived from theory or tuned to experimental data [26,27], and/or they can be heuristically scored according to similarity with existing sequences [28,29,30].

We focus our discussion on the former approach, as it is most transferrable to peptoids: little experimental data exists for most side chains and theoretical data is easier to obtain.Protein folding can be studied at several scales of complexity. Quantum mechanical modeling can determine small molecule, monomer-level energy preferences, at high resolution but also high computational costs. All-atom methods model molecules as combinations of atoms that interact viapotential energy functions (“force fields”), whose parameters describe atomic-scale interactions such as covalent bonds, hydrogen bonds, van der Waals forces, electrostatics, and solvent effects. These force fields may be tuned to both ab initio and experimental data. They are utilized with computer algorithms that intensively search for favorable folded structures. Finally, coarse-grained models blend multiple atoms into a single sub unit or “bead” and define force field parameters that describe interactions of these beads. Coarse-grained studies have reduced resolution compared to all-atom studies but are also less computationally intensive. Because of this, they are more practical to study larger simulations involving multiple chains, such as aggregation. More details on the different levels of molecular models can be found in [31] and [32].

Peptoid modeling can be approached using a similar framework: using quantum methods to characterize monomer subunits, and building these into force fields that can describe longer chains, or systems of chains. Protein force fields may sometimes be used for peptoid simulation because the backbones of peptides and peptoids are composed from the same atoms. However, some key differences between peptoids and peptides can limit this transferability. Force fields for peptoids should be carefully verified and parameterized when appropriate.

Three key features of peptoid backbones can grant them local folding behavior significantly different from that of proteins: (1) peptoid backbones do not form hydrogen bonds, (2) their backbones are achiral, and (3) the peptoid sp^2 amide bond can isomerize and exist as both a cis or a trans conformer. In proteins, hydrogen bonding between nearby backbone amide and carboxyl groups stabilizes highly ordered, localized secondary structures, including α-helices and β-sheets. Because the peptoid side chain replaces the amide hydrogen, peptoids do not form the same secondary structures. Furthermore, in proteins, each Cα atom (with the exception of glycine) is a chiral center with (L) chirality, granting the rotational directionality to the backbone seen in the handedness of α-helices and the twists of β-sheets.

Peptoid backbones resemble glycine, the only achiral amino acid. Therefore, unless chirality is added via a chiral side chain, peptoids do not favor a specific twist. Moreover, it is possible to build peptoids with side chains of alternating handedness, leading to unique secondary structures [15]. Finally, in proteins, the sp^2 amide bond is almost always in a trans configuration, where the carboxyl oxygen and amide hydrogen rest on opposite sides of the peptide bond, as the cis conformation leads to a steric clash between side chains. The peptoid amide bond, in contrast, can exist as a cis or a trans conformer, generally determined by the size of the side chain residue. The differences mentioned above must be addressed when developing peptoid models. In the case of chirality and hydrogen bonding differences, this can be achieved by careful adaption of protein models. Protein force field parameters can be tuned to favor secondary structures not present in peptoids [33], so protein force fields transferred to peptoids should be verified and tuned against peptoid experimental data. Addressing the amide bond isomerization can be more challenging.

The effect of a side chain on a peptoid secondary structure can differ depending on the isomerization state of the peptide bond. Due to this issue, all ab initio characterizations of side chain energetics should be examined in both the cis and the trans states. Ideally, parameters in all-atom and coarse-grained force fields should be tuned to accurately represent both configurations. Properly sampling peptoid cis/trans isomerization is an unsolved challenge. Isomerization itself is a rare event that can have an activation barrier of 15 kcal/mol [34] and characteristic times slower than a microsecond [35]. The physical mechanism of isomerization involves breaking the peptoid double bond and rotating through a partial-sp^3 transition structure [36]. Force field parameters enforce this high energy barrier, and in molecular dynamics, a simulation method where Newton's equations of motion are integrated in time to explore the conformational space [31], the high-energy peptide bond isomerization is unlikely to occur at room temperature. Therefore, to make comparisons between cis and trans structures, this isomerization must be studied through enhanced sampling techniques that force the system across the barrier. These include umbrella sampling [37]and replica exchange molecular dynamics [38].

In this paper, we survey the literature on modeling studies of peptoids in light of the issues discussed above. We have organized this review as follows: In section 2.1, we describe insights into monomer-level backbone energetics found from ab initio studies. These include studies that describe differences between peptoid and peptide structures, and studies characterizing the effects of specific side chains on the peptoid backbone. In section 2.2, we discuss the predictive power of peptoid modeling using combined all-atom/semi-empirical and combined all-atom empirical techniques. Section 2.3 describes studies using all-atom simulations of peptoid chains. These studies have two goals: to characterize the transferability of protein force field models to peptoid systems and to identify peptoids that form local secondary structures. In section 2.4, we review a coarse-grained model for peptoids. Section 2.5 describes how peptoid residues were added to the protein structure prediction program ROSETTA. Finally, we summarize the current state of peptoid modeling, and suggest future directions for computational studies of peptoids.

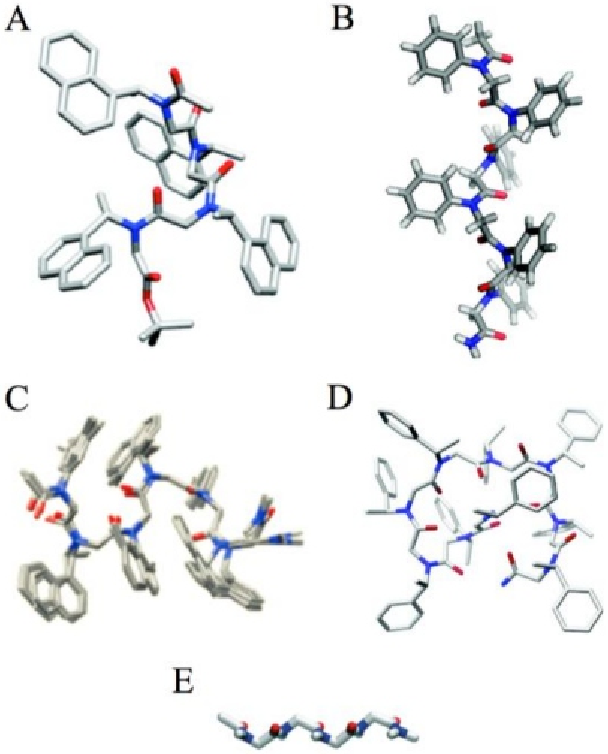

Figure 2. Known Peptoid Secondary Structures. (A) The PPI helix (shown here as (S)-–(1-napthylethyl)glycine) [11,39], (B) the N-(phenyl)glycine PPII helix [12], (C) the peptoid ribbon [14], (D) the threaded loop [13], and (E) the Σ-strand [15]. A, C, and D are shown without their backbone hydrogen atoms, and E is shown without its side chains. The secondary structures are characterized by their patterns of φ and ω dihedrals defined in Figure 3. The PPI and PPII helices have repeating (φ = (−)75°, ω ~ 0°) and (φ= (−)75°,ω = 180°) dihedrals, respectively. The threaded loop (D) is created by 9-mer NSPE peptoids and is stabilized by a hydrogen bonding interaction between side chains and their NH2 groups. The ribbon (C) has alternating ω = 0° and ω = 180° dihedrals and the Σ-strand (E) has ω = 180° and alternating φ = −90°, ψ = 120° and φ = −120°, ψ = 90°dihedrals. Structure A Reprinted with permission from Stringer et al. [39]. Structure B reprinted with permission from Shah et al. [12]. Structure C reprinted with permission from Crapster et al. [14]. Structure D Reprinted (adapted) with permission from Huang et al. [13]. Structure E reproduced with permission from Mannige et al. [15]. Copyright (A: 2011, B: 2008, D: 2006) American Chemical Society.

2. Modeling Studies of Peptoids

2.1. Ab Initio Studies of Peptoids

Ab initio simulations can be used to calculate highly accurate energy minimized structures for small molecules and have been used to characterize monomer-level structural preferences for peptoids. An advantage to this approach is that ab initio calculations are based wholly on quantum theory and do not rely on system-specific force field parameters or tuning to experimental data. A disadvantage is that ab initio simulations are computationally expensive for all but the smallest molecules. Therefore, ab initio peptoid modeling has mostly been used to characterize short-range energy preferences of peptoid monomers and to refine structure predictions from all-atom simulations (see section 2.2). This section focuses on ab initio characterization of peptoid monomers, but also describes the ab initio characterization of the binding structure of a peptoid trimer.

ab initio peptoid simulations frequently describe peptoid backbone energetics by calculating Ramachandran plots. Widely used to visualize protein secondary structure preferences, Ramachandran plots describe peptoid conformations in terms of the backbone dihedrals φ and ψ [40]. These dihedrals, a peptoid Ramachandran plot, and the locations of key peptoid structures are shown in Figure 3. Peptoid Ramachandran plots can look different from those of proteins due to structuraldifferences between peptoids and peptides and due to plotting conventions. Because of their achiral backbones, peptoid Ramachandran plots can have energy minima with both positive and negative φ.Protein φ dihedrals are almost always in the −180°–0° range because almost all amino-acids are (L) chiral. Additionally, peptoid Ramachandran plots should be plotted in pairs, with separate φ–ψ plots for the cis and trans conformers. A 3rd backbone dihedral, ω, describes the cis/trans isomerization. To compare cis (ω = 0°) and trans (ω = 180°) probabilities in the same figure, plots of ω versus φ orω versus ψ, may be more appropriate (See Figure 4) [41]. By convention, peptoid Ramachandran plots may also be plotted on 0°–360° axes rather than −180°–180° axis so that the αD minimum is centered.

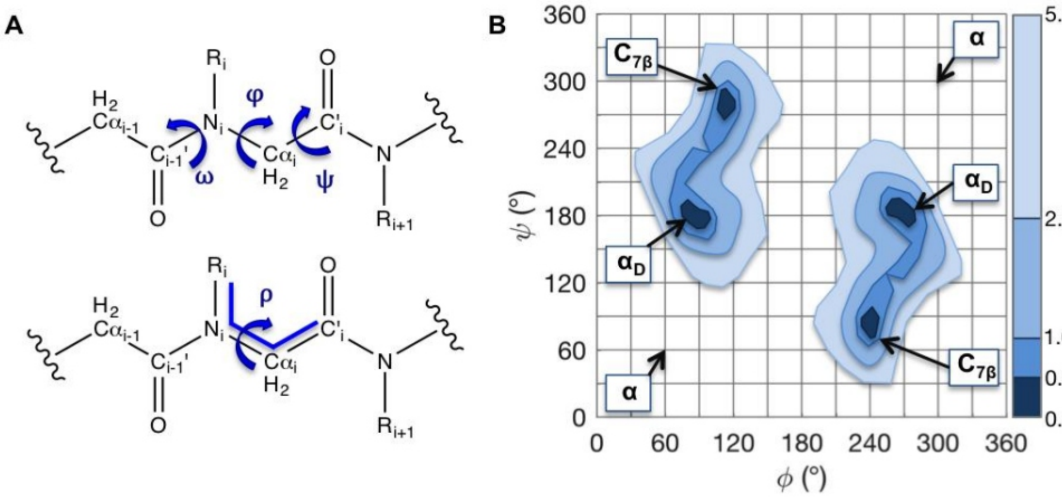

Figure 3. The peptoid backbone dihedrals and a peptoid Ramachandran plot. (A) Peptoid backbone conformations can be described by the dihedrals φ, ψ, and ω. The dihedral ω describes the isomerization of the planar peptoid bond. In the cis (ω = 0°) configuration, the side chain and the carbonyl oxygen are on the same side of the bond. In the trans(ω = 180°) configuration (shown) the side chain and the oxygen lie on opposite sides of the amide bond. The ρ dihedral, closely related to φ, is an additional parameter used to parameterize peptoid force fields, and is also shown. Ramachandran plots (B) are used to show backbone (φ–ψ) conformational preferences. Ramachandran plots are 2-D histograms that graph either the probability or the conformational energy of each φ/ψ pair of dihedrals. The figure shown corresponds to the trans isomer. This figure is based on data from Butterfoss [41].

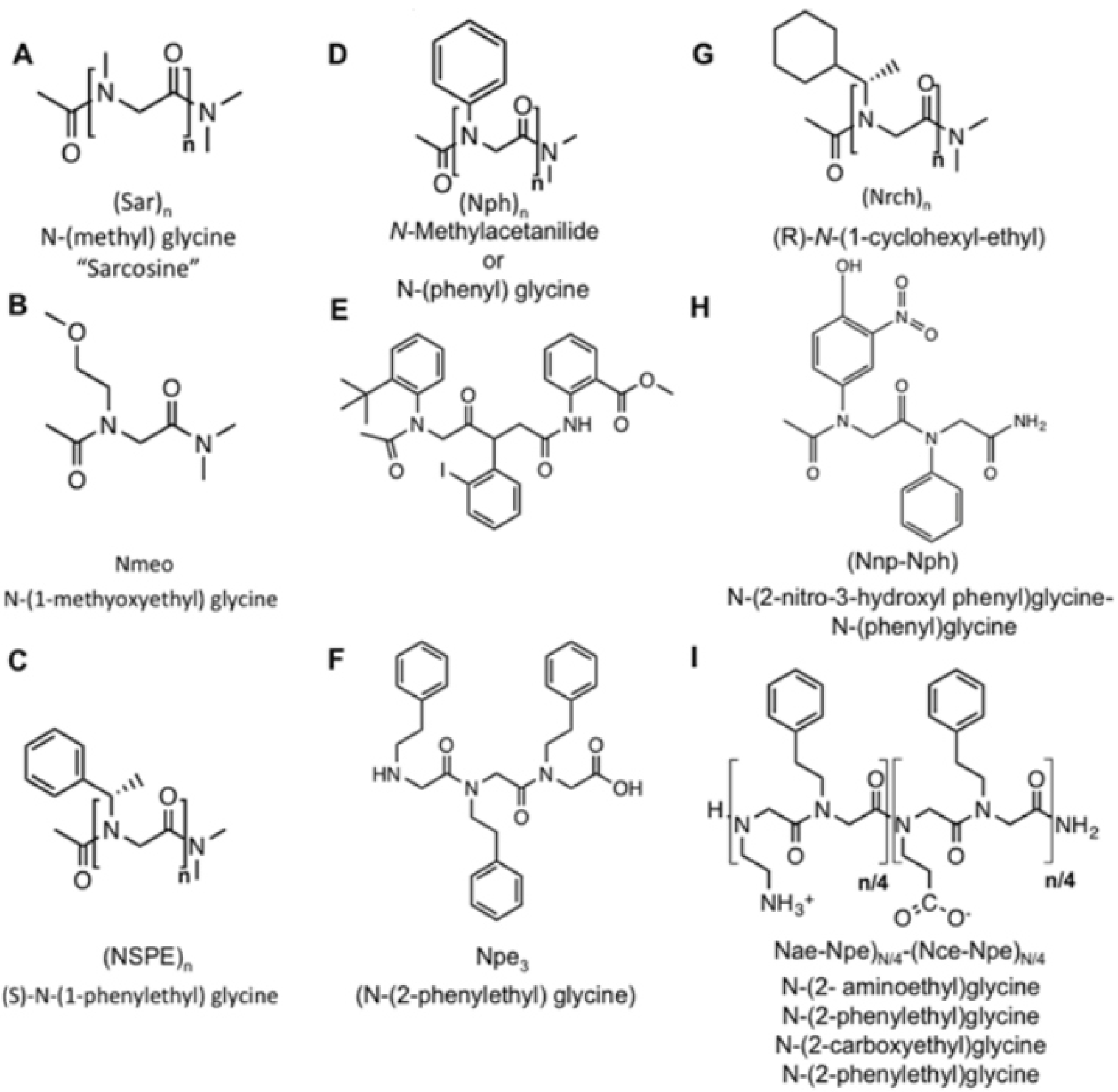

Figure 4. A partial summary of the peptoids described in this work. (A) Sarcosine (B) –(1-methoxyethyl)glycine, (C) (S)-N-(1-phenylethyl)glycine, (D) N-Methylacetanlide or N-(phenyl)glycine, (E) The aryl trimer studied by Butterfoss et al., (F) (N-(2-phenylethyl) glycine)3, (G) (R)-N-(1-cycloheyl-ethyl), (H) N-(2-nitro-3-hydroxyl phenyl)glycine-N-(phenyl)glycine, (I) (N-(2-aminoethyl)glycine-N-(2-phenylethyl) glycine)N/4-(N-(2-carboxyethyl)glycine-N-(2-phenylethyl)glycine).

Möhle and Hoffman [42] performed the first ab initio studies of a peptoid in 1996, comparing monomer conformations of the peptoid sarcosine (N-methylamide) to the small peptides glycine and alanine. Using HF-6-31G* and MP2-6-31G* calculations, they identified and named two vacuumphase minimum energy conformations that are unique to peptoids, $C_{7\beta}$ (φ ~ 130°, ψ ~ 78°) and α_D (φ ~ 75°, ψ ~ 170°), and observed a local minimum at the α-helical (α) dihedrals (φ ~ 55°, ψ ~ 55° and φ ~ 305°, ψ ~ 305°, ω ~ 180°) or (φ ~ 55°, ψ ~ 55°and φ ~ 305°, ψ ~ 305°, ω ~ 0°). All three minima exist for both the cis and trans sarcosine conformers. Möhle and Hoffman found that $C_{7\beta}$ and α_D are the lowest energy conformations for trans sarcosine, and cis αD is the global minimum in the vacuum phase. Using a polarized continuum model [43,44] to represent solvation effects, they showed that the solvation stabilizes the αD minimum in both cis conformations and that the cis and trans configurations are equally favorable in polar solvents.

Butterfoss et al. expanded on Möhle and Hoffman's work by exploring how longer backbones and more complex side chains affect the features of the peptoid energy surface [41]. Using the B3LYP//HF-6-31G* level of theory, they created Ramachandran plots for a sarcosine dimer and for monomers with N-(methoxyethyl) (Nmeo) and (S)-N-(1-phenylethyl) (NSPE) side chains. Chemical structures of these side chains are shown in Figure 4B and 4C. They overlaid these plots withexperimental dihedral measurements from X-ray crystallographic and NMR studies of a variety of peptoid oligomers. To ensure that the Ramachandran energies were calculated with sufficient accuracy, Butterfoss et al. compared minimum energy surfaces calculated at the MP2-6-31G*//HF-6-31G* and B3LYP/6-31G*//HF/6-31G* levels of theory. They found that these scans were very similar, particularly around the energy minima, suggesting that B3LYP/6-31G* calculations are sufficient for calculating peptoid structure energies.

Butterfoss et al.'s results showed that peptoid side chains exert strong control over the peptoid backbone dihedrals. As in Möhle and Hoffman's work, Butterfoss et al.'s sarcosine Ramachandran plot featured $C_{7\beta}$ and α_D minima. These same minima were present for the NSPE and Nmeo monomers, however, with the larger side chains, the α_D minimum was increasingly favored over $C_{7\beta}$. The chiral N side chain imparts a twisting structural preference on the peptoid backbone. This causes the Ramachandran plot to become asymmetric, as shown in Figure 5. In accordance with Möhle and Hoffman's solvated simulations, the experimental dihedrals summarized in Butterfoss et al. were largely localized to the α_D minima, confirming that it is the most common solvated conformation. In fact, the trans $C_{7\beta}$ minimum was only observed experimentally as part of a strained turn in a cyclic tetramer.

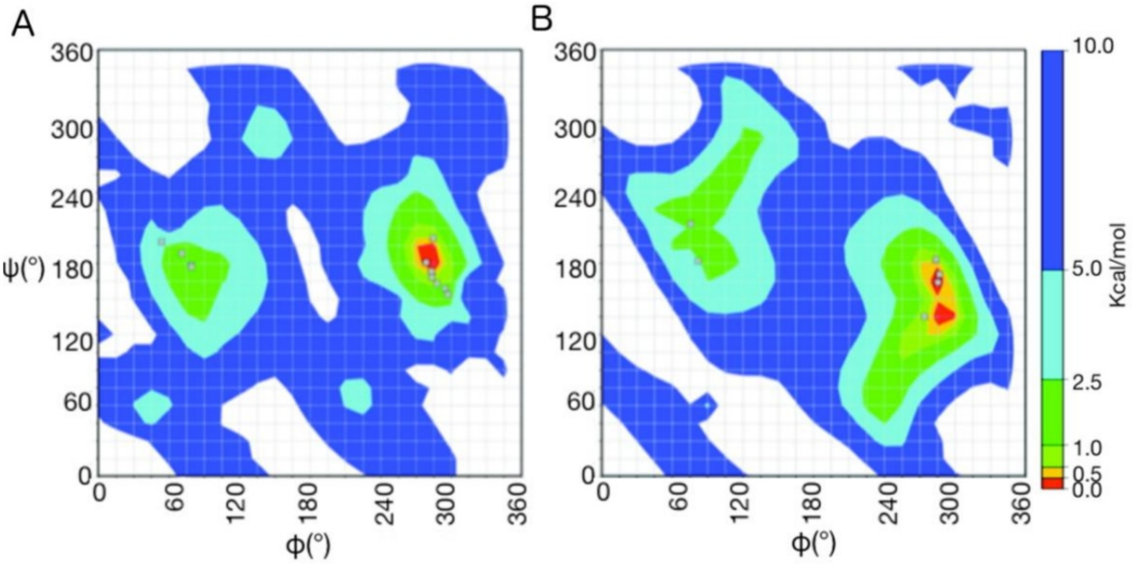

Figure 5. ab initio Ramachandran plot for cis (A) and trans (B). Both plots represent data at the HF-6-31G* level of theory. The "o" and "+" markers represent cyclic and linear experimental data. Adapted with permission from Butterfoss et al. [41].

Both Butterfoss and Möhle found that the peptoid nitrogen is slightly pyramidal, causing the ω dihedral to deviate from 0°or 180°in these cis and trans configurations. Butterfoss and coworkersobserved this aplanarity in both their experimental and computational results. This flexibility can be seen in traditional

Ramachandran plots in the form of wider, flatter contours, or it can be plotted explicitly in φ–ω and ψ–ω plots as shown in Figure 6.

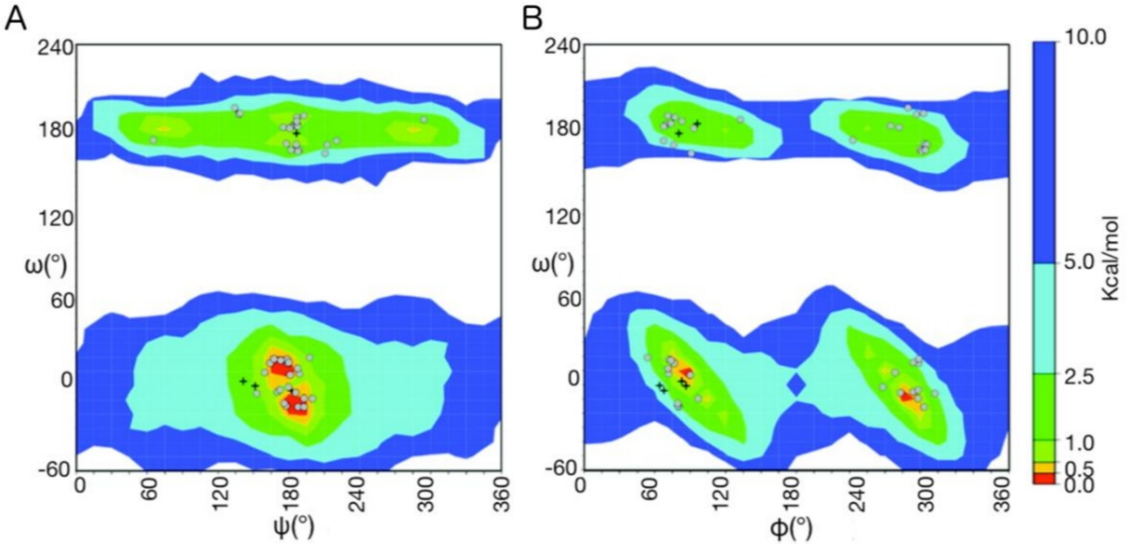

Figure 6. ψ–ω and φ–ω ab initio Ramachandran plots. φ–ψ Ramachandran plots are unable to describe isomerization of the ω dihedral. Butterfoss generated these (A) ψ–ω and (B) φ–ω plots as an alternative (ab initio HF-6-31G* data). ω dihedrals whichdeviate from 0° or 180° describe pyramidal nitrogen atoms. The “o” and “+” markers represent cyclic and linear experimental data. Adapted with permission from Butterfoss et al. [41], copyright (2009) American Chemical Society.

While most ab initio peptoid simulations have been used to characterize backbone energies, Parker et al. [45] used ab initio imulations for a different purpose: to understand the binding structures of a uranyl chelating peptoid. Parker et al. sought to identify peptoids that could selectively bind and extract uranyl (Uo_2^{2-}) ions from seawater. Using a combinatorial screening approach, they identified peptoids with three consecutive carboxyl side chains as strong uranyl binders. They then used B3LYP/6-31G(d,g) calculations to find energy minimized structures, and the integral equation formalism for the polarizable continuum model (IEFPCM) to calculate solvation free energies [46]. Parker et al. identified several possible uranyl binding conformations for a carboxyl peptoid trimer. Two of them are shown in Figure 7. Carboxyl groups and water molecules can bind to uranyl around the linear ion’s equatorial plane. Parker et al. identified and minimized binding configurations where the trimer binds uranyl through 1, 2, or 3 carboxyl groups. They suggested that the binding free energy of these complexes results from a tradeoff between binding enthalpy of each group and lost chain entropy due to conformational restriction.

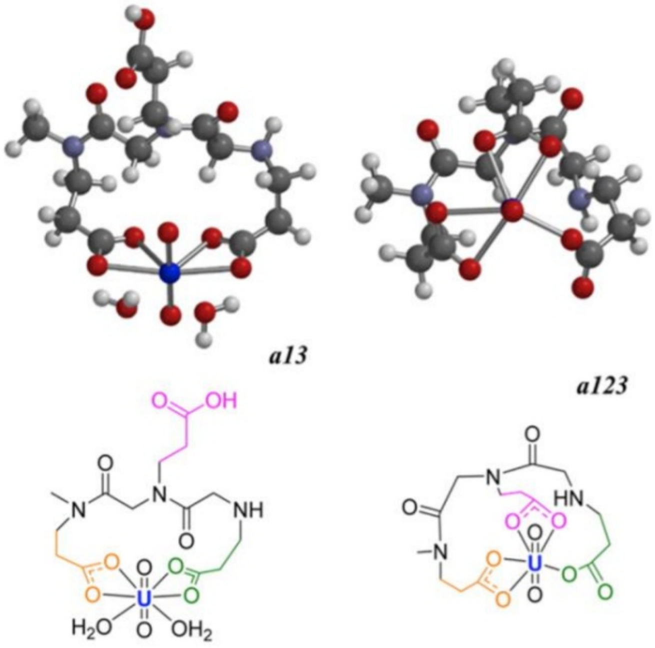

Figure 7. Two possible binding configurations for a uranyl chelating peptoid. The peptoid can bind the uranyl ion with one, two, or three carboxyl groups. The binding enthalpy released on additional carboxyl binding is counteracted by the entropy loss in the restricted backbone chain. Adapted with permission from Parker et al. [45].Copyright (2016) American Chemical Society.

2.2. Peptoid Structure Prediction with Combined Methods

Attempts to study longer peptoid chains with available models pose a problem: ab initio methods are computationally expensive for all but the smallest molecules, while existing all-atom force fields may not adequately model peptoid energetics. A productive solution has been to conduct simulation studies combining different levels of theory. In this approach, existing all-atom force fields are used to explore many possible conformations and identify potential minima, then semiempirical or ab initio methods are used to more precisely characterize these minimum energy structures. This kind of approach has played a role in the prediction and discovery of novel peptoid secondary structures, including the (S)-N-(1-phenylethyl)glycine (NSPE)-induced polyproline I helix (PPI) [11] and the N-(phenyl)-glycine-induced polyproline II helix (PPII) [12], and in the NMR characterization of the peptoid ribbon [14].

Armand et al. [11] predicted the structure of the NSPE PPI helix in 1997, using the AMBER all atom force field [47], and the AMSOL [48] semi-empirical force field with the AM1 parameter set. Previous experimental studies of peptoids with repeating NSPE side chains had resulted in Circular Dichroism (CD) spectra consistent with helical secondary structures [24]. With this knowledge, Armand et al. performed conformational searches of NSPE octamers by varying each of the φ and ψ dihedrals over a range of 0–360°. They calculated conformational energies using the torsional and nonbonded parameters of the AMBER force field, holding the molecule's angles and bond lengths fixed. To refine their structure characterization, they used AMSOL to minimize NSPE dimers.

Armand et al. showed that (NSPE)8 favored a PPI structure with cis ($\omega = 0°$) peptoid bonds and a negative ($-120° < \varphi < -75°$) twist, and identified the steric interactions that stabilize this conformation.

In particular, they suggested that steric clashes between the bulky side chain and the peptoid backbone enforce a preference for the cis isomer, and that the chiral center orients to minimize steric clashes between its bulky benzene and methyl groups and the neighboring carbonyl oxygen. Through these interactions, the chiral side chain stabilizes a negative φ for NSPE but positive φ for its isomer (R)-N-(1-phenylethyl)glycine (NRPE).

In a later paper, Shah et al. used a combination of all-atom and semi-empirical studies to show that peptoids with simple benzene side chains (Figure 4D) form PPI helices (Figure 2) [12].Experimental studies show that phenyl side chains promote the trans isomer of peptoid monomers [49]. Shah et al. were interested in other possible structural preferences imparted by this side chain. They generated an ab initio Ramachandran plot at the B3LYP/6-311+G(2d,p)//HF/6-31G* level of theory for an N-methylacetanilide dimer in the trans configuration. This scan identified minima in the φ–ψ energy surface at (φ = 60°, ψ = −150°) (+φ) and (φ = −60°, ψ = 150°)(−φ). To understand if these local energy preferences resulted in long-range order, Shah studied N methylacetanilide hexamers whose units had different combinations of these minima. The structures of these hexamers were then optimized using the Sigma simulation package [50] with the cedar all atom potential [51]. These calculations showed that steric clashes prohibited sequences with mixtures of residues in the +φ and −φ conformations. The minimum energy structures were helices with repeating −φ or +φ turns.

In a similar study, Butterfoss et al. attempted blind structure prediction for three peptoid oligomers [52]. Each oligomer, (E, F, and C in Figure 4) contained side chains that stabilized its crystals via different forces: (E) a trimer with three bulky, ortho-substituted benzene side chains that stabilize its structure via side chain steric effects, (F) (Npe)3, a trimer with three N-2-phenylethyl side chains whose crystals are stabilized by π–π interactions between benzene rings in neighboring molecules and by end group effects, (C) a cyclic (NSPE)9 molecule that forms needle like crystals whose side chains encage a single ethanol molecule. Prior to simulations, newly solved crystal structures for these chains were hidden from the modelers. Butterfoss et al. ran all-atom simulations, using parameters from the generalized amber force field (GAFF) [53] and represented solvent effects using the Generalized Born implicit solvent model [54]. To overcome cis/trans barriers and allow sampling of all ω conformations, they used replica exchange molecular dynamics (REMD) [38]. For the trimers, quantum structure calculations were performed, independent of the REMD, at the HF/3-21G* level with energies calculated at the M052X/6-311G** level. For the nonamer characterization, REMD and low-level quantum mechanics calculations were performed sequentially,using quantum mechanics to optimize the minimum energy structures identified by REMD.

Butterfoss et al. showed that the success of computational structure predictions with GAFF depends heavily on the particular forces that stabilize a peptoid structure. Both REMD and QM successfully predicted the crystal structure of the aryl trimer but identified a highly degenerate set of low energy conformations for (Npe)3. This is likely because the crystal structure of (E) is stabilized by its own side chains, while that of (Npe)3 is stabilized by interchain interactions. The cyclic (NSPE)9 simulations predicted the correct cis/trans patterning of the backbone ω dihedrals but failed to predict trends in the φ dihedrals and the orientations of the side chain dihedrals. Butterfoss re-ran a DFT calculation of NSPE including an explicit ethanol molecule, and showed that this predicted the correct structure. This suggests that, in this case, and other cases where complexation between solvent molecules and the peptoid side chains may be possible, the solvent must be explicitly included in the structure calculation.

2.3. All-atom Molecular Dynamics Studies of Peptoids

Quantum studies can precisely describe the properties of very small peptoids, but all-atom molecular dynamics (MD) studies are necessary to characterize longer peptoid chains. The quantum studies described previously were able to use monomer level energy preferences to predict structures for peptoids composed of the same repeated side chain. The next step in rational peptoid design is to predict how sequences composed of differing side chains combine to lead to folded structures or nanomaterials. All-atom simulations can build upon quantum work by making such predictions.All-atom force fields extend the range of size and length scales accessible to simulation by using effective interaction potentials between the atoms in the system. The parameters in these effective potentials can be fitted to experimental data and also to reproduce the results of quantum calculations, thus bridging the gap between the electronic and the atom-wise description of the system. The literature on force field development is extensive and methods vary depending on the force field, for an introduction to the subject the reader is referred to force field specific references [53,55,56,57].

The quality of all-atom simulation results is dictated by the quality of the all-atom force field used. Most peptoid MD simulations have been performed with either protein-specific force fields such as those of CHARMM [55] or AMBER [56], or generalized force fields such as OPLS [57] or GAFF [53]. A priori, both of these classes of force fields should not be expected to represent peptoidstructures accurately, as protein force fields may result in an unrealistic preference for proteinspecific secondary structures, such as α-helices, and general force fields may need extra tuning to correctly predict peptoid-specific structures. More recently, newer, peptoid-specific force fields have been developed to address these concerns.

Möhle and Hoffman ran the first all-atom simulations of sarcosine monomers, comparing these MD calculations against their ab initio results described in section 2.1 [58]. Using the CHARMM22 force field, they simulated sarcosine molecules both in vacuum and explicitly solvated with TIP3P water [59], and used holonomic constraints [60] to calculate relative free energies for the sarcosine minimum energy structures. In these simulations, CHARMM22 replicated the ab initio transvacuum phase minima α_D and $C_{7\beta}$ but overstabilized cis α. In spite of this, both cis and transsimulations in water replicated the ab initio results. The solvated simulations showed that both transand cisconformers preferred the α_D minimum when solvated in explicit water.

Voelz et al. sought to determine whether the GAFF all-atom force field [53] could simulate the dihedral preferences of small peptoids. Their work targeted the ab initio and experimental data published by Butterfoss et al. [41] and described in section 2.1. They parameterized GAFF forpeptoids using Antechamber automatic typing [61] and AM1-BCC charge fitting [62]. To ensure that both cis and trans configurations of the amide bond were explored, they used REMD to overcome high energy barriers [38]. GAFF's ability to recreate the ab initio peptoid dihedrals was compared to other AMBER force fields and to the OPLS force field in implicit and explicit solvent. GAFF simulations using the generalized Born surface area (GBSA) solvent model [54] predicted peptoid dihedrals better than other force fields and better than explicitly solvated simulations. GAFF recreated most of the ab initio dihedrals well but failed to reproduce the −φ preference observed for NSPE. GAFF was able to successfully reproduce the cis/trans patterning of the peptoid oligomers $(Sar)_8$, a (R)-N-(1-cyclohexyl-ethyl)glycine pentamer $(Nrch)_5$, and an N-(2-nitro-3-hydroxyl phenyl)glycine-N-(phenyl)glycine (Nnp–Nph) dimer (Figure 4A, G, and H).

Following up on Voelz's study, Mukherjee et al. developed a tuned force field, called GAFF-φ, to improve GAFF's sampling of the NSPE peptoid helix [63]. To create GAFF-φ, Mukherjee et al. added a single additional φ dihedral parameter to GAFF. This was sufficient to fix the φ distributions for NSPE residues. REMD simulations of chains of 3 to 15 NSPE residues showed that, in addition to improving the φ sampling, the ratio of cis and trans ω orientations was closer to experiment for GAFF-φ than for unfitted GAFF. This suggests that peptoid φ and ω energies are correlated.

Using GAFF-φ, Mukherjee et al. characterized the cooperative folding of the NSPE helix. To do this, they adapted the Lifson-Roig helix-coil theory [64] to describe peptoid helix formation. Briefly, the Lifson-Roig theory for proteins categorizes a chain's residues, based on their dihedrals, as either α-helical helical or non-helical coiled. A statistical weight for nucleation or elongation is then assigned to each helical residue. Which type of weight is assigned depends on whether one or both of the residue's neighbors are also helical. The combination of residue weights can then be used to calculate a chain's thermodynamic properties including the enthalpy of helix formation. Mukherjee sought to study the formation of PPI helices by NSPE peptoids, and defined helical conformationsusing the PPI dihedrals ($|\omega| < 90^{\circ}$with the $-\varphi$ conformation defined in section 2.2). They then fit LR nucleation and elongation weights to their GAFF-φ simulation data and used these weights to calculate the enthalpies and entropies of helix formation. The results showed that helix formation of 1-NSPE is entropically favorable, likely driven by steric interactions between the bulky side chains. More recently, Mirijanian et al. [65] developed the MFTOID (short for Molecular Foundry Peptoid) force field, a CHARMM-based all-atom force field parameterized specifically for peptoids.CHARMM [55] is an additive force field, whose energy function includes contributions from charges, van der Waals forces, and bonded terms including bonds, angles, dihedrals, and improper dihedrals. Mirijanian transferred most MFTOID parameters from the CHARMM22 force field by assigning peptoid atoms parameters from similar atoms in the peptide backbone. The Lennard-Jones, bond, and angle parameters for the peptoid nitrogen were transferred from the secondary peptide backbone nitrogen. Mirijanian et al. fit the charges of the amide nitrogen and carboxyl carbon, as well as the Lennard-Jones parameters of the carboxyl carbon. They also refit the ω dihedral potentialto allow cis/trans isomerization of the amide bond, and the ρ dihedral potential, which is closely related to φ (see Figure 3A). All other bonded parameters, including the φ and ψ dihedral potential terms were left unchanged.

To validate MFTOID, Mirijanian et al. carried out two different types of simulations. First, they used umbrella sampling [37] to create solvated and unsolvated free energy Ramachandran maps of sarcosine dipeptoids. These maps showed qualitative agreement with previous studies of sarcosine: the vacuum phase minima included α_D, $C_{7\beta}$ and α-helix, and the trans α_D configuration was stable in solvent. Unfortunately MFTOID over-stabilizes the cis α-helical conformation, the same effect observed by Möhle et al. [42] in their vacuum phase, CHARMM22 simulations of sarcosine. In MFTOID, the α conformation is also a global minimum in solvent. Mirijanian et al. also ran molecular dynamics simulations of N-2-phenylethyl trimer crystals. These simulations used experimental crystal structures composed of 256 trimers as starting configurations. They showed that after a 10 ns simulation at 300 K, MFTOID reproduces the starting crystal structure with a Root Mean Square Deviation (RMSD) of approximately 1.0 Å.

MFTOID parameters were tuned exclusively to sarcosine, and the transferability of the parameters to other peptoids is a potential issue. Prior work suggests that transferability should be high: Butterfoss's quantum results show that side chains bound to the backbone through a methylene group have similar dihedral minima to sarcosine. Additionally, Voelz's work with GAFF showed that many sterically dominated peptoid structures may not require precisely-tuned parameters to reproduce the correct minimum energy structures. However, peptoids with certain side chains, for example N-alkoxy-glycines [66] whose side chains attach to the backbone through a nitrogen-oxygen bond, exhibit different backbone behavior than sarcosine, and will likely need to be reparameterized.Mannige et al. [15] used MFTOID in combination with experimental data to explore the structure of bilayered peptoid microsheets. The work focused on microsheets previously described by Nam et al. [67] composed of diblock peptoid oligomers of alternating charged and hydrophobic side chains of the form (Nae–Npe)n/4–(Nce–Npe)n/4) (Figure 4I). In water, these peptoids form large sheets, two chains thick, with the hydrophobic phenyl-ethyl side chains sequestered inside. MFTOID quantitatively and qualitatively reproduced the features of these sheets. It reproduced X-ray and NMR data describing sheet thickness and strand separation to an RMSD within 1 Å.

In the same work, Mannige et al. recognized a novel peptoid secondary structure defined by residues with an alternating pattern of dihedrals. They dubbed this structure a "Σ-strand" and suggested that it was the first of a class of possible peptoid secondary structures described by the alternating conformations of two residues rather than a single repeating dihedral motif. A Ramachandran scheme for this type of secondary structure is shown in Figure 8.

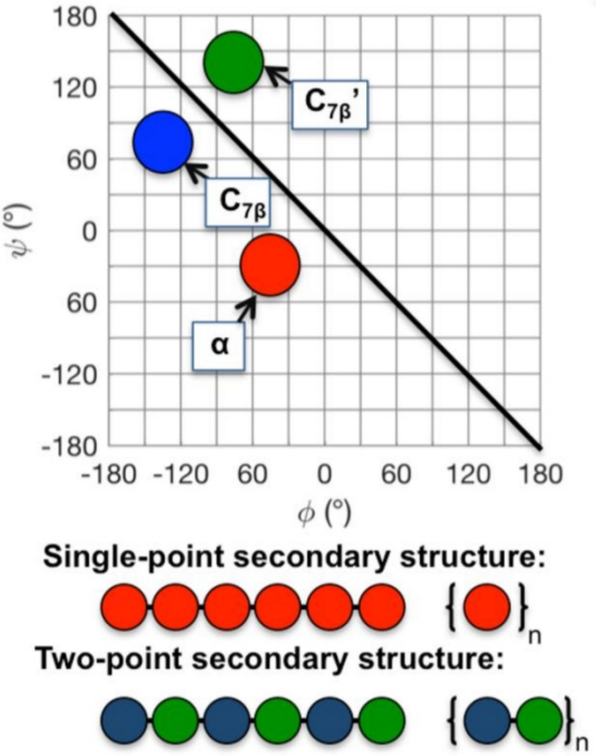

Figure 8. The Σ-strand alternating motif. Mannige et al. [15] described a secondary structure of alternating residues with alternating rotational states. Single-point secondary structures, like α-helices, contain a single repeating dihedral conformation. Two-point or Σ-strand motifs have alternating dihedral pairs, in this example they alternate between the $C_{7\beta}$ and $C_{7\beta}$' conformations. This figure is based on a scheme by Mannige [15].

In subsequent work, Mannige, Kundu, and Whitelam derived a new order parameter called the “Ramachandran Number” (R) to describe alternating structures such as Σ-strands [68]. Using a thoughtfully chosen gridding of the Ramachandran space, they derived an expression for R that combines information about the φ and ψ dihedrals and the radius of r_g of the structure. The number is obtained by defining a grid of values of φ and ψ in the Ramachandran plot, which is rotated, shifted and rescaled so that the important secondary structures are mapped onto unique integer numbers. The Ramachandran Number can be plotted as a histogram “barcode” or as a per residue graph allowingvisualization of patterned peptoid structures including Σ-strands. This is shown in Figure 9.

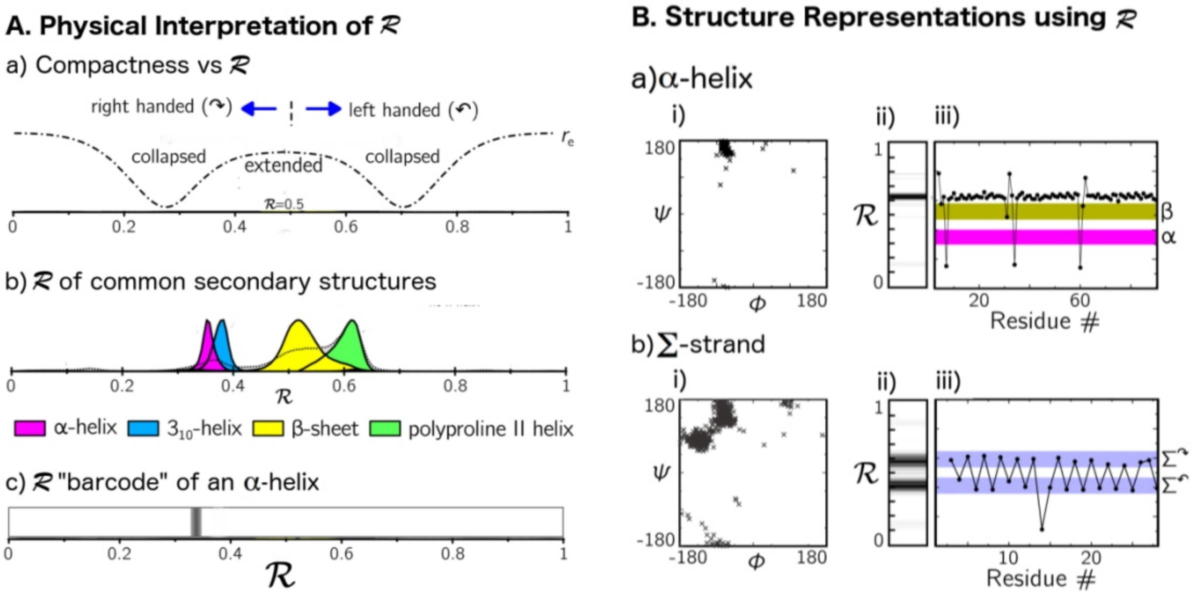

Figure 9. The Ramachandran Number. The Ramachandran Number R is a parameter derived by Mannige et al. which combines a residue’s φ and ψ dihedrals and chain compactness into a single number. (A) (a) shows the physical information encoded in R. R > 0.5 describes a left handed twist, R < 0.5 describes a right handed twist. R = 0, R =0.5, and R = 1.0 describe fully extended backbones, while intermediate values are more compact. (b) The distribution of R values for common peptide secondary structures. (C) A Ramachandran number histogram or “barcode” representation of the α-helix, (the distribution in (b) shown as a heat map). (B) shows different structure visualizations for an α-helix (a) and for the alternating Σ-strand (b). (i) A Ramachandran plot, (ii) a barcodeof the Ramachandran number, (iii) An R versus residue # plot, which, unlike thehistograms, can show the alternating pattern of dihedrals in the Σ-strand. This figure is reproduced from figures in [68].

2.4.Coarse-grained Peptoid Simulations

All-atom simulations are useful for studying the conformational energies of individual peptoid chains, however, they are too computationally demanding for studying slow processes involving the interactions of many chains. All-atom simulations are best for simulations up to a few microseconds,and up to a few million atoms. Simulations of self-assembling peptoid nanomaterials, such as peptoid sheets, require force fields usable across millisecond time scales or longer for many hundreds of peptoid chains. One way this type of simulation can be achieved is by using coarse-grained models that incorporate many peptoid atoms into a single bead.

Coarse-grained models extend the range of length and time scales that can be simulated beyond the limits of all-atom models by defining larger entities (“beads”) that encompass groups of atoms, as the basic building blocks of the system. The interactions between these effective building blocks are then fitted to reproduce the results of all-atom simulations of smaller cognate systems. Some of the methods used to develop these models include Boltzmann Inversion [69], which builds effective potentials by fitting to the all-atom pair distribution functions, Force Matching [70], which fits the effective potential to the net forces acting between the building blocks in the all-atom simulations, and Relative Entropy Minimization [71], which seeks to minimize the information loss in replacing the atomistic description with the coarse grained one. A detailed description of these approaches is beyond the scope of this paper, for a recent exhaustive review the reader is referred to [32]. It is also possible to build coarse-grained models by directly fitting to experimental data in what is called “top-down” coarse-graining, but such approaches have not, to our knowledge, been used for peptoids.

Haxton et al. [72] developed the first coarse-grained model for peptoids and named it MF-CG TOID (short for Molecular Foundry-Coarse-Grained-Peptoid). They developed this model specifically to study (Nca–Npe)n/4–(Nae–Npe)n/4 self assembly into bilayered sheets. The (Nca–Npe)n/4–(Nae–Nce)n/4 polymers are described in the review of Mannige’s work above. Haxton et al. deliberately avoided a coarse-graining scheme based on beads with radially-symmetric Lennard-Jones potentials and their bonded interactions, arguing that this way of partitioning the model’s potential energy is artificial and non-ideal. Instead, each MF-CG-TOID bead was represented by a location($\vec{r}$)and an orientation parameter($\hat{x}$).Figure 10 contains a scheme showing $\vec{r}$ and $\hat{x}$ parameter for a pair of peptoid side chains.

Haxton et al. parameterized 4 coarse-grained beads: one bead representing a backbone unit, and one for each of the 3 side chains in the (Nca–Npe)n/4–(Nae–Npe)n/4 system. Most of the force field interaction potentials are functions of these parameters: backbone–backbone and backbone–sidechain bonded parameters, and nonbonded interactions between like-side chains. Nonbonded interactions between unlike-beads and between backbone-beads were represented by hard-sphere potentials, which depend only on a size parameter. Parameterization involved fitting 115 parameters through direct Boltzmann Inversion of MFTOID and published all-atom data, with 4 parameters fit to the target system (phenylethyl side chain size, interaction strength and bonded interaction with the backbone, and the backbone bead size). Haxton et al. performed Monte Carlo simulations using their force field to model structures in different stages of (Nae–Npe)n/4–(Nce–Npe)n/4 bilayered sheet formation [73]. MF-CG-TOID qualitatively represented the globular structure of individual peptoids in water, and their unfolding when exposed to an air surface. Using the model, they were able to match X-Ray spectroscopy data, such as chain spacing for single layer sheets at the air-water interface, and free floating peptoid bilayers. MF-CG-TOID has been used for an additional study of (Nae–Npe)n/4–(Nce–Npe)n/4 sheet formation [74].

MF-CG-TOID reproduces (Nca–Npe)n/4–(Nae–Npe)n/4 sheets with excellent precision, but using it to simulate other peptoid side chains may be challenging, particularly due to the number of parameters that must be fit for each new side chain. Its direct Boltzmann inversion scheme requires an accurate all-atom peptoid model. Therefore, adding novel peptoids to MF-CG-TOID would potentially require two parameterization steps: one adding the new side chain to MFTOID, and a second parameterization using the Boltzmann inversion procedure.

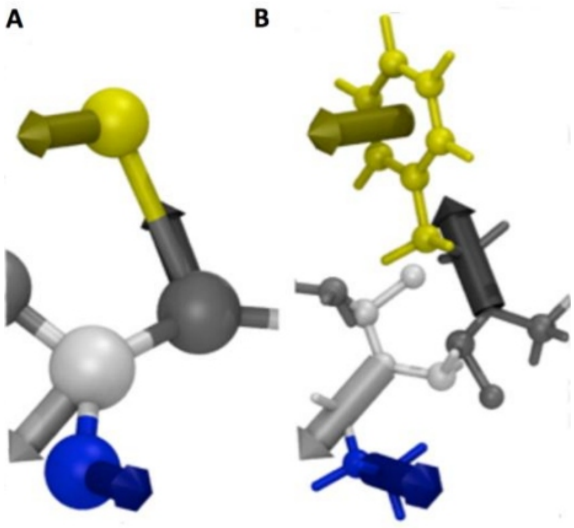

Figure 10. MF-CG-TOID coarse-grained peptoid model. (A) The MF-CG-TOID coarse-grained model for an (Nae)–(Npe) unit. Each peptoid monomer is represented by two coarse-grained sites. Each site is described by two degrees of freedom: a position $\vec{\boldsymbol{r}}$ represented in the diagram by spheres and a director $\hat{\boldsymbol{x}}$ represented by the arrows. All bonded and nonbonded interaction parameters in MF-CG-TOID are functions of both parameters ($\boldsymbol{X}(\vec{r_i}, \hat{x}_i)$). (B) The all atom structure upon which this model was based. Figure reproduced with permission from Haxton et al. [72]. Copyright (2014) American Chemical Society.

2.5. Peptoid Simulations in Rosetta

For researchers looking to study peptoids with existing protein structure prediction software, Drew et al. added peptoids to the Rosetta framework [75]. Rosetta [76] is a molecular modeling and protein design utility with broad functionality, including algorithms for de novo protein structure prediction. Rosetta's folding algorithm differs from the all-atom and coarse-grained approaches described above, which use physics-based models and long simulations (or enhanced-sampling methods) to identify minimum energy configurations. Instead, Rosetta identifies thousands of possible folded structures through a conformational search algorithm based on Metropolis Monte Carlo, first sampling large backbone (φ–ψ) motions and then refining the local side chain structure based on a pre-calculated "rotamer library" of allowable side chain (χ) dihedral conformations. These structures are then minimized using physics-based molecular mechanics models. Candidate structures are those with the lowest minimized energies.To incorporate peptoids into ROSETTA, functions for use in the Monte Carlo search and energy parameters for the molecular mechanics minimization are needed. Drew defined a peptoid backbone unit to have the same backbone atoms as a peptide subunit, determined molecular mechanics parameters for over 50 side chains, and modified Rosetta's conformational search algorithms to allow sampling of backbone cis/trans isomerization and nitrogen flexibility. Peptoid molecular mechanics parameters were taken from CHARMM. A CHARMM proline nitrogen atom was used to represent the peptoid backbone nitrogen, and dihedral energy parameters were tuned to quantum data. To enable conformational search of both cis and trans isomers, Drew et al. modified the rotamer creation function to sample both isomers. They then added two types of Monte Carlo moves to the search algorithm: one sampling cis/trans flips and one sampling small backbone nitrogen pyramidalization by making small adjustments to the ω dihedral.

In subsequent work, Renfrew et al. [77] developed a peptoid rotamer library for use with Drew's framework and validated Rosetta-derived peptoid structure predictions against known experimental structures. Rosetta's peptide rotamer libraries include sterically allowed configurationsfor the side chain χ1 and χ2 dihedrals (shown in Figure 11). For peptides, these libraries are defined with respect to (φ,ψ) conformations and each (χ1,χ2) rotamer is weighted with a probability derived from data from the Protein Data Bank. Renfrew showed that peptoid rotamer libraries should be defined with respected to (φ,ψ,ω) combinations, to account for peptoid nitrogen pyramidalization. They also compensated for the lack of peptoid experimental data by deriving rotamer weights based on the Rosetta molecular mechanics force field and quantum mechanical calculations. Renfrew et al. validated their model against experimental data for the common peptoid side chains Nph, Nspe, Nmeo, and N-(S)-1-Napthylethyl (Ns1e), and showed that the rotamer library was able to represent the preferred rotamers of the peptoid within a RMSD of 0.5 Å.

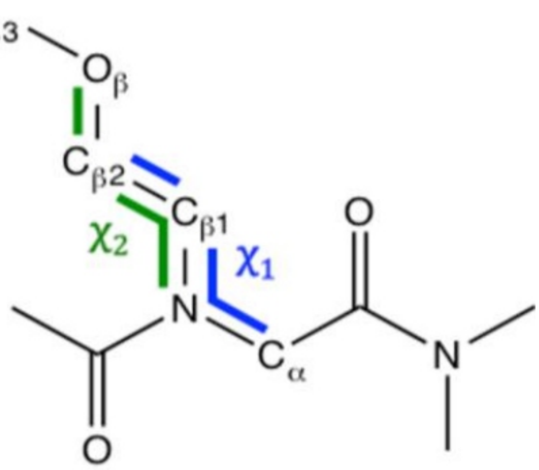

Figure 11. The rotamer dihedrals. Rosetta rotamer libraries describe the side chain conformation in terms of the dihedrals χ1 and χ2. Renfrew developed rotamer libraries for 54 peptoid side chains.

The peptoid residues included in Rosetta can be used to predict peptoid structures or structures of polymers combining peptoid and peptide residues.

3. Conclusions and Future Directions

In recent years, computational studies of peptoids have multiplied and progress has been made towards predicting peptoid conformations based on the sequence of side chains attached to their backbones. Approaches to predict folded peptoid structures depend on the nature of the side chains and the length of the chain under study. From quantum chemistry, we can obtain fundamental understanding of the peptoid backbone and the influence of individual side chains on its conformation, but longer chains cannot be studied due to computational constraints. All-atom models can partially overcome these limitations and predict the folding behavior of several short peptoid chains, however they are limited by the quality of the all-atom force field used. Existing protein andgeneral force fields have been shown to adequately predict the backbone dihedrals of several solved crystal structures, and new peptoid-specific force fields have been developed in the last few years. However, peptoid force fields are only parameterized for a limited set of side chains. Finally, coarsegrained models have shown promise in the study of (Nae–Npe)n/4–(Nce–Npe)n/4 bilayer sheet formation. While peptoid modeling studies have made much progress in the last 20 years, there is still a need to develop and improve peptoid models. This will require expanding the number of side chains parameterized for all-atom and coarse-grained peptoid force fields and, at the same time, expanding the number of experimentally solved structures available to tune and verify these force fields. Additionally, it will require developing simulation techniques that encourage peptoids to explore both the cis and the trans peptide bond conformations. This may involve use of enhanced sampling techniques such as REMD, umbrella sampling, and metadynamics [78]. Nevertheless, in recent years there has been a big improvement in the simulation models available for peptoids, and we expect to see much better tools to predict peptoid structure and properties in the near future.

Conflict of Interest

All authors declare no conflict of interest in this paper.

References

1. *Sun J, Zuckermann RN (2013) Peptoid Polymers: A Highly Designable Bioinspired Material.ACS Nano 7: 4715–4732.*
2. *Seo J, Lee BC, Zuckermann RN (2011) Peptoids: Synthesis, Characterization, and Nanostructures. Compr Biomater 2: 53–76.*
3. *Chongsiriwatana NP, Patch JA, Czyzewski AM, et al. (2008) Peptoids that mimic the structure, function, and mechanism of helical antimicrobial peptides. Proc Natl Acad Sci USA 105: 2794–2799.*
4. *Vollrath SBL, Fürniss D, Schepers U, et al. (2013) Amphiphilic peptoid transporters—synthesis and evaluation. Org Biomol Chem 11: 8197–8201.*
5. *Li N, Zhu F, Gao F, et al. (2010) Blockade of CD28 by a synthetical peptoid inhibits T-cell proliferation and attenuates graft-versus-host disease. Cell Mol Immunol 7: 133–142.*
6. *Dohm MT, Kapoor R, Barron AE (2011) Peptoids: Bio-Inspired Polymers as Potential Pharmaceuticals. Curr Pharm Design 17: 2732–2747.*
7. *Statz AR, Park JP, Chongsiriwatana NP, et al. (2008) Surface-immobilised antimicrobial peptoids. Biofouling 24: 439–448.*
8. *Seurynck SL, Patch JA, Barron AE (2005) Simple, helical peptoid analogs of lung surfactant protein B. Chem Biol 12: 77–88.*
9. *Maayan G, Ward MD, Kirshenbaum K (2009) Folded biomimetic oligomers for enantioselective catalysis. Proc Natl Acad Sci USA 106: 13679–13684.*
10. *Gellman SH (1998) Foldamers: A Manifesto. Accounts Chem Res 31: 173–180.*
11. *Armand P, Kirshenbaum K, Falicov A, et al. (1997) Chiral N-substituted glycines can form stable helical conformations. Fold Design 2: 369–375.*
12. *Shah NH, Butterfoss GL, Nguyen K (2008) Oligo(N-aryl glycines): A New Twist on Structured Peptoids. J Am Chem Soc 130: 16622–16632.*

13. Huang K, Wu CW, Sanborn TJ, et al. (2006) A threaded loop conformation adopted by a family of peptoid nonamers. J Am Chem Soc 128: 1733–1738.

14. Crapster JA, Guzei IA, Blackwell HE (2013) A Peptoid Ribbon Secondary Structure. Angew Chem Int Ed 52: 5079–5084.

15. Mannige RV, Haxton TK, Proulx C, et al. (2015) Peptoid nanosheets exhibit a new secondary structure motif. Nature 526: 415–420.

16. Hebert ML, Shah DS, Blake P, et al. (2013) Tunable peptoid microspheres: effects of side chain chemistry and sequence. Org Biomol Chem 11: 4459–4464.

17. Murnen HK, Rosales AM, Jaworski JN, et al. (2010) Hierarchical Self-Assembly of a Biomimetic Diblock Copolypeptoid into Homochiral Superhelices. J Am Chem Soc 132: 16112–16119.

18. Sanii B, Kudirka R, Cho A, et al. (2011) Shaken, Not Stirred: Collapsing a Peptoid Monolayer To Produce Free-Floating, Stable Nanosheets. J Am Chem Soc 133: 20808–20815.

19. Dill KA, MacCallum JL (2012) The Protein-Folding Problem, 50 Years On. Science 338: 1042–1046.

20. Gorske BC, Blackwell HE (2006) Tuning peptoid secondary structure with pentafluoroaromatic functionality: A new design paradigm for the construction of discretely folded peptoid structures. J Am Chem Soc 128: 14378–14387.

21. Stringer JR, Crapster JA, Guzei IA, et al. (2010) Construction of Peptoids with All Trans-Amide Backbones and Peptoid Reverse Turns via the Tactical Incorporation of N-Aryl Side Chains Capable of Hydrogen Bonding. J Org Chem 75: 6068–6078.

22. Gorske BC, Nelson RC, Bowden ZS, et al. (2013) “Bridged” n→π* Interactions Can Stabilize Peptoid Helices. J Org Chem 78: 11172–11183.

23. Wu CW, Kirshenbaum K, Sanborn TJ, et al. (2003) Structural and spectroscopic studies of peptoid oligomers with alpha-chiral aliphatic side chains. J Am Chem Soc 125: 13525–13530.

24. Kirshenbaum K, Barron AE, Goldsmith RA, et al. (1998) Sequence-specific polypeptoids: A diverse family of heteropolymers with stable secondary structure. Proc Natl Acad Sci USA 95: 4303–4308.

25. Armand P, Kirshenbaum K, Goldsmith RA, et al. (1998) NMR determination of the major solution conformation of a peptoid pentamer with chiral side chains. Proc Natl Acad Sci USA 95: 4309–4314.

26. Dill KA (1990) Dominant forces in protein folding. Biochemistry 29: 31.

27. Dill KA, Ozkan SB, Shell MS, et al. (2008) The protein folding problem. Annu Rev Biophys 37: 289–316.

28. Sali A, Blundell TL (1993) Comparative protein modeling by satisfaction of spatial restraints. J Mol Biol 234: 779–815.

29. Shen MY, Sali A (2006) Statistical potential for assessment and prediction of protein structures.Protein Sci 15: 2507–2524.

30. Rohl CA, Strauss CEM, Misura KMS, et al. (2004) Protein structure prediction using Rosetta. Method Enzymol 383: 66–93.

31. Leach AR (2001) Molecular modelling : principles and applications, England: Pearson/Prentice Hall.

32. Shell MS (2016) Coarse-Graining with the Relative Entropy, In: Rice SA, Dinner AR, Advances in Chemical Physics, Malden: Wiley-Blackwell, 395–441.

33. Mackerell AD, Feig M, Brooks CL (2004) Extending the treatment of backbone energetics in protein force fields: Limitations of gas-phase quantum mechanics in reproducing protein conformational distributions in molecular dynamics simulations. J Comput Chem 25: 1400–1415.

34. Feigel M (1983) Rotation barriers of amides in the gas phase. J Phys Chem 87: 3054–3058.

35. Sui Q, Borchardt D, Rabenstein DL (2007) Kinetics and equilibria of cis/trans isomerization of backbone amide bonds in peptoids. J Am Chem Soc 129: 12042–12048.
36. Duffy EM, Severance DL, Jorgensen WL (1992) Solvent effects on the barrier to isomerization for a tertiary amide from ab initio and Monte Carlo calculations. J Am Chem Soc 114: 7535–7542.
37. Torrie GM, Valleau JP (1977) Nonphysical sampling distributions in Monte Carlo free-energy estimation: Umbrella sampling. J Comput Phys 23: 187–199.
38. Sugita Y, Okamoto Y (1999) Replica-exchange molecular dynamics method for protein folding. Chem Phys Lett 314: 141–151.
39. Stringer JR, Crapster JA, Guzei IA, et al. (2011) Extraordinarily Robust Polyproline Type I Peptoid Helices Generated via the Incorporation of alpha-Chiral Aromatic N-1-Naphthylethyl Side Chains. J Am Chem Soc 133: 15559–15567.
40. Ramachandran GN, Ramakrishnan C, Sasisekharan V (1963) Stereochemistry of polypeptide chain configurations. J Mol Biol 7: 95–99.
41. Butterfoss GL, Renfrew PD, Kuhlman B, et al. (2009) A Preliminary Survey of the Peptoid Folding Landscape. J Am Chem Soc 131: 16798–16807.
42. Mohle K, Hofmann HJ (1996) Peptides and peptoids—A systematic structure comparison. J Mol Model 2: 307–311.
43. Miertuš S, Scrocco E, Tomasi J (1981) Electrostatic interaction of a solute with a continuum. A direct utilizaion of AB initio molecular potentials for the prevision of solvent effects. Chem Phys55: 117–129.
44. Pascual-Ahuir JL, Silla E, Tomasi J, et al. (1987) Electrostatic interaction of a solute with a continuum. Improved description of the cavity and of the surface cavity bound charge distribution. J Comput Chem 8: 778–787.
45. Parker BF, Knight AS, Vukovic S, et al. (2016) A Peptoid-Based Combinatorial and Computational Approach to Developing Ligands for Uranyl Sequestration from Seawater. Ind Eng Chem Res 55: 4187–4194.
46. Cancès E, Mennucci B, Tomasi J (1997) A new integral equation formalism for the polarizable continuum model: Theoretical background and applications to isotropic and anisotropic dielectrics. J Chem Phys 107: 3032–3041.
47. Cornell W, Cieplek P, Bayly CI, et al. (1995) A Second Generation Force-Field for the Simulation of Proteins, Nucleic-Acids, and Organic-Molecules. J Am Chem Soc 117: 5179–5197.
48. Hawkins GD, Cramer CJ, Truhlar DG (1998) Universal Quantum Mechanical Model for Solvation Free Energies Based on Gas-Phase Geometries. J Phys Chem B 102: 3257–3271.
49. Bradley EK, Kerr JM, Richter LS, et al. (1997) NMR Structural Characterization of Oligo-N Substituted Glycine Lead Compounds from a Combinatorial Library. Mol Divers 3: 1–15.
50. Mann G, Yun RH, Nyland L, et al. (2002) The Sigma MD Program and a Generic Interface Applicable to Multi-Functional Programs with Complex, Hierarchical Command Structure, In:Schlick T, Gan HH, Computational Methods for Macromolecules: Challenges and Applications,Springer, Berlin, Heidelberg, 129–145.
51. Hermans J, Berendsen HJC, Van Gunsteren WF, et al. (1984) A consistent empirical potential for water–protein interactions. Biopolymers 23: 1513–1518.
52. Butterfoss GL, Yoo B, Jaworski JN (2012) De novo structure prediction and experimental characterization of folded peptoid oligomers. Proc Natl Acad Sci USA 109: 14320–14325.
53. Wang JM, Wolf RM, Caldwell JW, et al. (2004) Development and testing of a general amber force field. J Comput Chem 25: 1157–1174.
54. Onufriev A, Bashford D, Case DA (2004) Exploring protein native states and large-scale conformational changes with a modified generalized born model. Proteins 55: 383–394.

55. MacKerell AD, Bashford D, Bellott M, et al. (1998) All-atom empirical potential for molecular modeling and dynamics studies of proteins. J Phys Chem B 102: 3586–3616.

56. Case DA, Cheatham TE, Darden T, et al. (2005) The Amber biomolecular simulation programs.J Comput Chem 26: 1668–1688.

57. Jorgensen WL, Maxwell DS, TiradoRives J (1996) Development and testing of the OPLS all atom force field on conformational energetics and properties of organic liquids. J Am Chem Soc118: 11225–11236.

58. Moehle K, Hofmann HJ (1996) Peptides and peptoids—A quantum chemical structure comparison. Biopolymers 38: 781–790.

59. Jorgensen W, Chandrasekhar J, Madura J, et al. (1983) Comparison of Simple Potential Functions for Simulating Liquid Water. J Chem Phys 79: 926–935.

60. Tobias DJ, Brooks CL (1988) Molecular dynamics with internal coordinate constraints. J Chem Phys 89: 5115–5127.

61. Wang J, Wang W, Kollman PA, et al. (2006) Automatic atom type and bond type perception in molecular mechanical calculations. J Mol Graph Model 25: 247–260.

62. Jakalian A, Jack DB, Bayly CI (2002) Fast, efficient generation of high-quality atomic charges. AM1-BCC model: II. Parameterization and validation. J Comput Chem 23: 1623–1641.

63. Mukherjee S, Zhou G, Michel C, et al. (2015) Insights into Peptoid Helix Folding Cooperativity from an Improved Backbone Potential. J Phys Chem B 119: 15407–15417.

64. Lifson S, Roig A (1961) On the Theory of Helix—Coil Transition in Polypeptides. J Chem Phys34: 1963–1974.

65. Mirijanian DT, Mannige RV, Zuckermann RN, et al. (2014) Development and use of an atomistic CHARMM-based forcefield for peptoid simulation. J Comput Chem 35: 360–370.

66. Jordan PA, Bishwajit P, Butterfoss GL, et al. (2011) Oligo(N-alkoxy glycines): trans substantiating peptoid conformations. J Pept Sci 96: 617–626.

67. Nam KT, Shelby SA, Cho PH, et al. (2010) Free-floating ultrathin two-dimensional crystals from sequence-specific peptoid polymers. Nat Mater 9: 454–460.

68. Mannige RV, Kundu J, Whitelam S (2016) The Ramachandran Number: An Order Parameter for Protein Geometry. PLoS One 11: e0160023.

69. Reith D, Putz M, Muller-Plathe F (2003) Deriving effective mesoscale potentials from atomisticsimulations. J Comput Chem 24: 1624–1636.

70. Izvekov S, Voth GA (2005) Multiscale coarse graining of liquid-state systems. J Chem Phys 123: 134105.

71. Shell MS (2008) The relative entropy is fundamental to multiscale and inverse thermodynamic problems. J Chem Phys 129: 144108.

72. Haxton TK, Mannige RV, Zuckermann RN, et al. (2015) Modeling Sequence-Specific Polymers Using Anisotropic Coarse-Grained Sites Allows Quantitative Comparison with Experiment. JChem Theory Comput 11: 303–315.

73. Sanii B, Haxton TK, Olivier GK, et al. (2014) Structure-Determining Step in the Hierarchical Assembly of Peptoid Nanosheets. ACS Nano 8: 11674–11684.

74. Haxton TK, Zuckermann RN, Whitelam S (2016) Implicit-Solvent Coarse-Grained Simulation with a Fluctuating Interface Reveals a Molecular Mechanism for Peptoid Monolayer Buckling. J Chem Theory Comput 12: 345–352.

75. Drew K, Renfrew PD, Butterfoss GL (2013) Adding Diverse Noncanonical Backbones to Rosetta: Enabling Peptidomimetic Design. PLoS One 8: e67051.

76. Kaufmann KW, Lemmon GH, DeLuca SL, et al. (2010) Practically Useful: What the Rosetta Protein Modeling Suite Can Do for You. Biochemistry 49: 2987–2998.

77. Renfrew PD, Craven TW, Butterfoss GL, et al. (2013) A Rotamer Library to Enable Modeling and Design of Peptoid Foldamers. J Am Chem Soc 136: 8772–8782.

78. Laio A, Gervasio FL (2008) Metadynamics: a method to simulate rare events and reconstruct the free energy in biophysics, chemistry and material science. Rep Prog Phys 71: 126601.

·ISSN : 2372-0484

Coherent spin dynamics in a helical arrangement of molecular dipoles

Elena D´ıaz 1, Rafael Gutierrez ´2, Christopher Gaul 1,3, Gianaurelio Cuniberti 2,4,5, andFrancisco Dom´ınguez-Adame 1,*
1 GISC, Departamento de F´ısica de Materiales, Universidad Complutense, E-28040 Madrid, Spain
2 Institute for Materials Science, Dresden University of Technology, 01062 Dresden, Germany
3 Cognitec Systems GmbH, Großenhainer Str. 101, 01127 Dresden, Germany
4 Dresden Center for Computational Materials Science (DCMS), TU Dresden, 01062 Dresden,Germany
5 Center for Advancing Electronics Dresden, TU Dresden, 01062 Dresden, Germany

ABSTRACT

Experiments on electron transport through helical molecules have demonstrated the appearance of high spin selectivity, in spite of the rather weak spin-orbit coupling in organiccompounds. Theoretical models usually rely on different mechanisms to explain these experiments,such as large spin-orbit coupling, quantum dephasing, the role of metallic contacts, or the interplaybetween a helicity-induced spin-orbit coupling and a strong dipole electric field. In this work weconsider the coherent electron dynamics in the electric field created by the helical arrangement ofdipoles of the molecule backbone, giving rise to an effective spin-orbit coupling. We calculate the spinprojection onto the helical axis as a figure of merit for the assessment of the spin dynamics in a verylong helical molecule. We prove that the spin projection reaches a steady state regime after a shorttransient. We compare its asymptotic value for different initial conditions, aiming to better understandthe origin of the spin selectivity found in experiments.

Keywords: spin polarized transport; helical molecules; spin sensitivity; nanoscale materials;spin-orbit

1. Introduction

Exploiting the spin degree of freedom to transfer information or perform logic operations builds the basis of spintronics. Currently, the majority of existing spintronic devices are based on inorganicmaterials. However, using organic molecules in spintronics, though very challenging, would offermany advantages such as the possibility for chemically tuning the spin-dependent response as well astheir inexpensive synthesis in large amounts. For molecules lacking a magnetic response, we mightnot expect any strong spin-dependent properties. Surprisingly, it has been experimentally shown undera variety of conditions that double-stranded DNA oligomers, bacteriorhodopsin, oligopeptides, andhelicene molecules can act as strong spin filters [1–10]. Since the only common feature of all thesesystem is their helical symmetry, the hypothesis has been suggested—and meanwhile there is strongexperimental evidence supporting it—that the observed spin selectivity is tightly related to the chiralityof the probed molecules. These results can have profound implications not only for the design of novelorganic or bio-inspired spintronic devices, but also shed a new light on electron transfer in biologicallyrelevant molecules.

On the theoretical side, several approaches related to spin selective transport in helical systems have been proposed [11–19]. They are based both on tight-binding-like models as well as on continuumapproaches. Their common denominator—an exception is Ref. [17]—is the assumption that a nonconventional spin-orbit coupling (SOC) in a helical system can lead to the blocking of one type of spincomponent. Although it has been shown in these different studies that spin selectivity is possible, thereis still in our view a lack of a unifying microscopic picture allowing to connect the specific features ofthe electronic structure of helical molecules to model parameters.In this study, we investigate the coherent dynamics of an electronic wave packet propagating inthe electric field created by a helical arrangement of dipoles. This field induces an effective SOC thatresembles the Rashba-type spin-orbit interaction in semiconductors. However, here the SOC mirrorsthe global helical symmetry of the system. The model is inspired by previous studies reported inRefs. [13, 15]. We compute the spin projection onto the helical axis and consider it as a figure ofmerit for the assessment of the spin dynamics in a long helical molecule. We prove that the spinprojection reaches a steady state regime after a quick transient and compare its asymptotic value fordifferent initial conditions, aiming at a better understanding of the origin of the spin selectivity foundin experiments. It is worth mentioning that we focus on the coherent electron dynamics only andneglect dissipation hereafter. Nevertheless, dissipation may play a key role in experiments on electrontransport through helical molecules and more realistic models need to consider its impact [14, 20–22].

2. Model Hamiltonian

Electric dipoles are common in the backbone of helical molecules, like the alpha helix. The backbone with a helical arrangement of peptides dipoles wraps the cylindrical structure of themolecule. Therefore, an electron moving along the axis of the helical molecule interacts with theelectric field created by the dipoles. In the reference frame of the moving electron, the electric fieldinduces a magnetic field, thus leading to a Rashba-like SOC.

We are concerned with a very long helix of radius R directed along the Z axis with axially oriented dipoles, as depicted in Figure 1. The point dipoles are labeled by an integer index n running from $-\infty$ to ∞. They are located at $\boldsymbol{r}_n = n\Delta z\,\hat{\boldsymbol{e}}_z + R\,\hat{\boldsymbol{\rho}}_n$ and their dipole moments are $\boldsymbol{d}_n = d\,\hat{\boldsymbol{e}}_z$. Δz is the spacing of the z component of the position vector of the dipoles and the pitch of the helix is $b = N_d\Delta z$, where N_d is the number of dipoles per turn. Here, we have used cylindrical coordinates so that $\hat{\boldsymbol{\rho}}_n = (\cos\varphi_n, \sin\varphi_n, 0)$ with $\varphi_n = 2\pi n/N_d + \pi$. The constant angle π added to φ_n is only introduced for convenience. It represents a π-rotation about the molecule axis that does not affect the physical magnitudes.

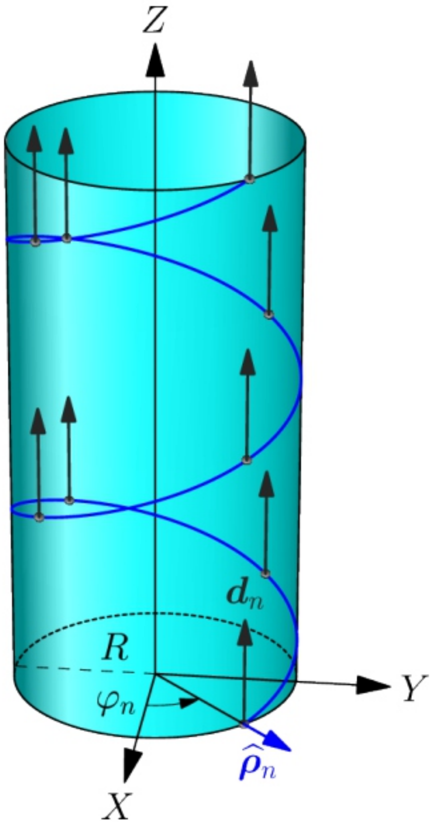

Figure 1. An electron in a given spin state is moving along the axis Z of a helical arrangement of electric dipoles $\boldsymbol{d}_n$. The electric field created by the dipoles induces a magnetic field in the rest frame of the electron and hence influences its spin dynamics.

Each dipole contributes to the total electric field of the molecule as follows [23]

$$\boldsymbol{E}(\boldsymbol{r}) = \frac{1}{4\pi\epsilon_0}\sum_{n=-\infty}^{\infty}\left[3\,\frac{(\boldsymbol{r}-\boldsymbol{r}_n)\cdot\boldsymbol{d}_n}{|\boldsymbol{r}-\boldsymbol{r}_n|^5}\,(\boldsymbol{r}-\boldsymbol{r}_n)-\frac{\boldsymbol{d}_n}{|\boldsymbol{r}-\boldsymbol{r}_n|^3}\right]. \tag{1}$$

Now we calculate the components of the electric field (1) in the XY plane for they are needed to obtain the SOC. Since the dipoles are parallel to the molecule axis, we get

$$\begin{aligned} E_x(\boldsymbol{r}) &= \frac{3d}{4\pi\epsilon_0}\sum_{n=-\infty}^{\infty}\frac{z-n\Delta z}{|\boldsymbol{r}-\boldsymbol{r}_n|^5}\,(x-x_n)\,, \\ E_y(\boldsymbol{r}) &= \frac{3d}{4\pi\epsilon_0}\sum_{n=-\infty}^{\infty}\frac{z-n\Delta z}{|\boldsymbol{r}-\boldsymbol{r}_n|^5}\,(y-y_n)\,. \end{aligned} \tag{2}$$

We will neglect the electron motion out of the molecular axis hereafter. In this case, the position vector is $\boldsymbol{r} = z\,\hat{\boldsymbol{e}}_z$ when the electron moves along the Z axis. Setting $x = y = 0$ in Eq. (2) yields

$$E_x(z) = -\frac{3Rd}{4\pi\epsilon_0}\sum_{n=-\infty}^{\infty}\frac{(z-n\Delta z)\cos\varphi_n}{\left[R^2+(z-n\,\Delta z)^2\right]^{5/2}}\,,$$
$$E_y(z) = -\frac{3Rd}{4\pi\epsilon_0}\sum_{n=-\infty}^{\infty}\frac{(z-n\Delta z)\sin\varphi_n}{\left[R^2+(z-n\,\Delta z)^2\right]^{5/2}}\,. \tag{3}$$

For the calculation of the SOC, we will need to evaluate $\mathcal{E}(z) = -i\,[E_x(z) - iE_y(z)]$(see Ref. [15] for further details). From Eq. (3) we obtain

$$\mathcal{E}(z) = -i\,\frac{3Rd}{4\pi\epsilon_0}\sum_{n=-\infty}^{\infty}\frac{(z-n\,\Delta z)\,e^{-i2\pi n/N_d}}{\left[R^2+(z-n\,\Delta z)^2\right]^{5/2}}\,. \tag{4}$$

For the typical values of the parameters found in helical molecules, it turns out that $\Delta z \ll b$, namely $N_d \gg 1$. Under this premise, we can replace the sum over n in Eq. (4) by an integral. To this end, we introduce the dimensionless variable $u = (z - n\Delta z)/b$ and make the formal substitution $\sum_n \to (b/\Delta z)\int du$ in the summation appearing in Eq. (4). Thus

$$\sum_{n=-\infty}^{\infty}\frac{(z-n\,\Delta z)\,e^{-i2\pi(z-n\Delta z)/b}}{\left[R^2+(z-n\,\Delta z)^2\right]^{5/2}} \simeq \frac{1}{b^3\Delta z}\int_{-\infty}^{\infty}du\,\frac{u\,e^{i2\pi u}}{(u^2+R^2/b^2)^{5/2}}\,. \tag{5}$$

After performing the integration we obtain

$$\mathcal{E}(z) = \frac{2\pi d}{\epsilon_0\Delta z b^2}\,K_1(2\pi R/b)\,e^{-i2\pi z/b} \equiv \mathcal{D}_0\,e^{-i2\pi z/b}\,, \tag{6}$$

where K_1 is the modified Bessel function of the second kind. Taking $R/b = 1/4$ as a typical value in helical molecules, then $K_1(2\pi R/b)$ ' 1/4. It is worth mentioning that a similar result appears when theelectric dipoles are contained in the XY plane but with a different constant D_0. Therefore, the preciseorientation of the dipoles do not affect qualitatively our conclusions.

The SOC Hamiltonian arises as a relativistic correction to the electron motion along the molecular axis Z [24]. Heuristically it can be understood as the result of the interaction between the electronspin and the magnetic field induced by the electric field **E** in the rest frame of the electron. The SOC Hamiltonian is expressed as $\hat{\mathcal{H}}_{\mathrm{SO}} = \lambda\boldsymbol{\sigma}\cdot(\hat{\boldsymbol{p}}\times\boldsymbol{E})$ symmetrized such that the Hamiltonian is Hermitian. Here $\lambda = e\hbar/(2mc)^2$ and $\boldsymbol{\sigma}$ is a vector whose components are the Pauli matrices σ_x, σ_y, and σ_z. For $\hat{\boldsymbol{p}} = \hat{p}\,\hat{\boldsymbol{e}}_z$ the SOC Hamiltonian reduces to

$$\hat{\mathcal{H}}_{\mathrm{SO}} = \frac{\lambda}{2}\left[\hat{p}_z\begin{pmatrix}0 & \mathcal{E}(z)\\ \mathcal{E}^*(z) & 0\end{pmatrix} + \begin{pmatrix}0 & \mathcal{E}(z)\\ \mathcal{E}^*(z) & 0\end{pmatrix}\hat{p}_z\right]. \tag{7}$$

The total Hamiltonian of the electron moving along the molecular axis subject to the SOC is $\hat{\mathcal{H}} = \hat{p}^2/2m + \hat{\mathcal{H}}_{\mathrm{SO}}$. The electrostatic potential due to the helical arrangement of dipoles is constant along the molecular axis and it can then be neglected. Taking Eq. (6) into account, the Hamiltonian can be cast in the form $\hat{\mathcal{H}} = E_b\hat{H}$ where the dimensionless Hamiltonian $\hat{H}$ reads

$$\hat{H} = -\frac{\partial^2}{\partial\xi^2} - 2\pi\gamma \begin{pmatrix} 0 & e^{-i2\pi\xi}\left(i\frac{\partial}{\partial\xi} + \pi\right) \\ e^{i2\pi\xi}\left(i\frac{\partial}{\partial\xi} - \pi\right) & 0 \end{pmatrix} . \qquad (8)$$

For the sake of simplicity we have defined $E_b = \hbar^2/2mb^2$, $\xi = z/b$, and the dimensionless spin-orbit parameter $\gamma = \hbar\lambda\mathcal{D}_0/(2\pi b E_b)$. Previous models in the literature have estimated a phenomenological SOC to be of the order of $\hbar\lambda\mathcal{D}_0 = 4 - 12\,\text{meV nm}$ [13], what defines a reasonable range for our dimensionless SOC parameter as $\gamma = 0.06 - 0.2$.

3. Steady States in a Helical Molecule

The dimensionless Hamiltonian (8) is not translation invariant but it commutes with the helical operator $\hat{q} = \hat{p} + \pi\sigma_z$, which has the eigenstates

$$\chi(\xi) = \begin{pmatrix} \chi_1 e^{i(q-\pi)\xi} \\ \chi_2 e^{i(q+\pi)\xi} \end{pmatrix} . \qquad (9)$$

Inserting the ansatz (9) into the dimensionless Schrodinger equation $\hat{H}\chi(\xi) = \varepsilon\chi(\xi)$ yields the following eigenenergies

$$\varepsilon_{qs} = q^2 + \pi^2 - 2\pi s\sqrt{1+\gamma^2}\,q \equiv (q-q_s)^2 - \pi^2\gamma^2 , \qquad s = \pm 1 . \qquad (10)$$

The energy as a function of the helical momentum splits into two parabolas (free electrons)displaced by an amount $q_s = s\pi\sqrt{1+\gamma^2}$ from the origin. Thus, the helical conformation of the electric dipoles brings in the additional effective momentum qs . The additional momentum arising from the helical geometry of organic molecules can have an impact on the optical transitions as well [25].

The corresponding normalized eigenfunctions of the dimensionless Hamiltonian (8) are easily found to be

$$\chi_{qs}(\xi) = \frac{1}{2}\begin{pmatrix} [(1+s)\cos\phi + (1-s)\sin\phi]e^{i(q-\pi)\xi} \\ [(1-s)\cos\phi - (1+s)\sin\phi]e^{i(q+\pi)\xi} \end{pmatrix} , \qquad (11)$$

with

$$\tan\phi = \frac{\gamma}{1+\sqrt{1+\gamma^2}} . \qquad (12)$$

4. Coherent Spin Dynamics

We turn to the problem we are interested in, namely the dynamics of an electron wave packet with a given spin state. To proceed, we expand any arbitrary solution to the time-dependent Schrodinger equation $i\partial_t\chi(\xi,t) = \hat{H}\chi(\xi,t)$ in terms of the eigenvectors of the Hamiltonian (8) as follows

$$\chi(\xi,t) = \sum_s \int_{-\infty}^{\infty} \frac{dq}{2\pi}\, C_{qs}\chi_{qs}(\xi)\, e^{-i\varepsilon_{qs}t} \,, \tag{13}$$

where time is expressed in units of $\hbar/E_b$ and

$$C_{qs} = \int_{-\infty}^{\infty} d\xi\, \chi^{\dagger}_{qs}(\xi)\cdot\chi(\xi,0) \,. \tag{14}$$

Consider an initial wave packet $f(\xi)$ of dimensionless width W given as

$$\chi(\xi,0) = f(\xi)\left(\cos(\theta)\,\boldsymbol{u}_{\uparrow} + e^{i\varphi}\sin(\theta)\,\boldsymbol{u}_{\downarrow}\right) \,, \tag{15}$$

where $\boldsymbol{u}_{\sigma}$ with $\sigma = \uparrow, \downarrow$ denotes an eigenvector of σ_z. For the sake of concreteness we set $\varphi = 0$ hereafter. When $\theta = 0$ ($\theta = \pi/2$), the spin of the initial wave packet is parallel (antiparallel) to the molecule axis and we will refer to as *fully polarized state*. Similarly, when $\theta = \pi/4$, the spin of the initial wave packet is directed along the X axis. We will name such state as *fully unpolarized* in the sense that the initial spin is out of the molecule axis.

Notice that we assume the same spatial function $f(\xi)$ for both components of the initial wave packet $\chi(\xi,0)$. This is not a serious limitation but calculations are largely simplified. We take a Gaussian spatial function of the form

$$f(\xi) = \left(\frac{1}{2\pi W^2}\right)^{1/4} \exp\left(ik\xi - \frac{\xi^2}{4W^2}\right) \,, \tag{16}$$

where k is the initial momentum and W is the standard deviation. A lengthy but straightforward calculation from Eq. (13) yields

$$\begin{aligned} \chi_{\uparrow}(\xi,t) = e^{-i\pi(\xi+\pi t)}\Big\{ &\cos\theta\,\cos^2\phi\, G_{-}(\xi+\omega t,t) + \cos\theta\,\sin^2\phi\, G_{-}(\xi-\omega t,t) \\ &- \frac{1}{2}\sin\theta\sin(2\phi)\left[G_{+}(\xi+\omega t,t) - G_{+}(\xi-\omega t,t)\right]\Big\} \,, \end{aligned} \tag{17}$$

$$\begin{aligned} \chi_{\downarrow}(\xi,t) = e^{i\pi(\xi-\pi t)}\Big\{ &\sin\theta\,\sin^2\phi\, G_{+}(\xi+\omega t,t) + \sin\theta\,\cos^2\phi\, G_{+}(\xi-\omega t,t) \\ &- \frac{1}{2}\cos\theta\sin(2\phi)\left[G_{-}(\xi+\omega t,t) - G_{-}(\xi-\omega t,t)\right]\Big\} \,, \end{aligned} \tag{18}$$

where $\omega = 2\pi\sqrt{1+\gamma^2}$ and

$$G_{\pm}(y,t) = \left(\frac{W^2}{2\pi}\right)^{1/4} \frac{1}{\sqrt{W^2+it}} \exp\left\{-\frac{y^2/4 + i(\pi\mp k)\left[(\pi\mp k)t \pm y\right]W^2}{W^2+it}\right\} \,. \tag{19}$$

As an example, Figure 2 depicts the short-time ($0 < t < 1$) behavior of $|\chi_{\uparrow}(\xi,t)|^2$ and $|\chi_{\downarrow}(\xi,t)|^2$ of an initially fully polarized ($\theta = 0$) Gaussian wave packet of width $W = 1$ and $k = 1$ when the dimensionless SOC is $\gamma = 0.2$. Although initially the lower component vanishes $\chi_{\downarrow}(\xi,0) = 0$ (hard to see in Figure 2), it grows very quickly but remains much smaller than the upper component $\chi_{\uparrow}(\xi,t)$. Therefore, the SOC leads to a partial depolarization of the initially fully polarized Gaussian wave packet.

5. Spin Projection

We now focus on the spin projection (SP) onto the direction of the electron momentum, i.e., along the molecule axis

$$\mathrm{SP}(t) = \int_{-\infty}^{\infty} d\xi\, \boldsymbol{\chi}^{\dagger}(\xi,t)\sigma_z\boldsymbol{\chi}(\xi,t) = \cos(2\phi)\int_{-\infty}^{\infty}\frac{dq}{2\pi}\left[|C_{q,+1}|^2 - |C_{q,-1}|^2\right]$$
$$+\, 2\sin(2\phi)\int_{-\infty}^{\infty}\frac{dq}{2\pi}\,\mathrm{Re}\left[C^{*}_{q,+1}C_{q,-1}e^{i(\varepsilon_{q,+1}-\varepsilon_{q,-1})t}\right] . \tag{20}$$

This magnitude, also known as helicity, becomes time-dependent because the operator σ_z does not commute with the Hamiltonian (8). In other words, the spin projection onto the direction of the electron momentum is not conserved. Nevertheless, we will show that the last term in Eq. (20) vanishes after aquick transient and SP(t) reaches an asymptotic value as time evolves.

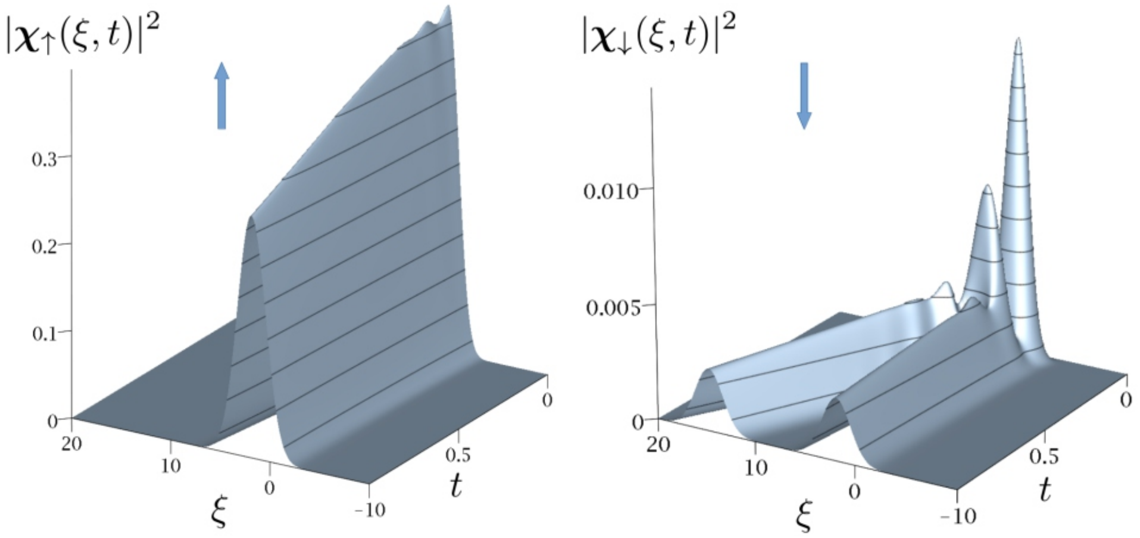

Figure 2. Short-time dynamics of an initially fully polarized (θ = 0) Gaussian wave packet of width W = 1 and k = 1 when the dimensionless SOC is $\gamma = 0.2$. Notice the differentvertical scale for the upper and lower components.

Let us consider an initially fully polarized (θ = 0 or θ = π/2) Gaussian wave packet as that shown in Figure 2. We can calculate SP(t) from Eq. (20) to obtain

$$\mathrm{SP}(t) = \pm\cos^2(2\phi) + \mathrm{Re}\left[e^{\mp i2\omega\pi t}\int_{-\infty}^{\infty} d\xi\, f^{*}(\xi)f(\xi+2\omega t)\right]\sin^2(2\phi) . \tag{21}$$

The upper and lower sign refers to spin up ($\theta = 0$) and down ($\theta = \pi/2$), respectively. After a straightforward calculation, one obtains a closed expression for SP(t) that has a transient contribution which vanishes at large times $t \gg W/\omega$. A transient time $W/\omega \sim 40$ fs is roughly estimated for a highly localized initial state with $W = 1$ passing through a helical molecule with a SOC parameter of $\gamma = 0.1$. Thus, after a quick transient regime, the spin projection reaches the asymptotic value given as $\mathrm{SP}_{\infty} = \mathrm{SP}(t \to \infty)$ with

$$\mathrm{SP}_{\infty} = \pm\cos^2(2\phi) = \pm\frac{1}{1+\gamma^2} . \tag{22}$$

Therefore, the larger the SOC parameter, the smaller the asymptotic spin projection. The result above mentioned is not surprising. An initial wave packet with a well defined spin projection such that $|\mathrm{SP}(0)| = 1$ get their components mixed as time evolves because of the presence of the SOC. At long time, the spin projection diminishes and finally $|\mathrm{SP}_{\infty}| < 1$.

The dynamics of a wave packet with vanishing initial spin projection is more interesting because it becomes spin polarized along the molecule axis after being transmitted through the molecule.Therefore, we now consider a fully unpolarized initial wave packet with $\theta = \pi/4$. From Eq. (21) wefind that the asymptotic spin projection is non zero, given as

$$\mathrm{SP}_\infty = -\frac{\gamma}{1+\gamma^2}\int_{-\infty}^{\infty} d\xi\,|f(\xi)|^2\cos(2\pi\xi) = -\frac{\gamma}{1+\gamma^2}\,e^{-2\pi^2W^2}\,. \tag{23}$$

For a narrow initial wave packet ($W \ll 1$), the integral in Eq. (23) becomes unity and then $\mathrm{SP}_\infty \simeq -\gamma/(1+\gamma^2)$. In this case $|\mathrm{SP}(0)| = 0$ but the spin projection becomes nonzero with time and reaches a finite value such that $|\mathrm{SP}_\infty| \neq 0$.

Figure 3 depicts the absolute value of the asymptotic spin projection as a function of the dimensionless SOC parameter γ for initially polarized ($\theta = 0$) and fully unpolarized ($\theta = \pi/4$) wave packets. In the former case, $|\mathrm{SP}_\infty|$ monotonously decreases on increasing γ, as expected. However, the behavior of $|\mathrm{SP}_\infty|$ for an initially fully unpolarized wave packet is more complex. At low values of γ the asymptotic $|\mathrm{SP}_\infty|$ increases upon increasing the SOC and reaches a maximum value of 50% at $\gamma = 1$. On the contrary, a further increase of γ above unity yields smaller $|\mathrm{SP}_\infty|$.

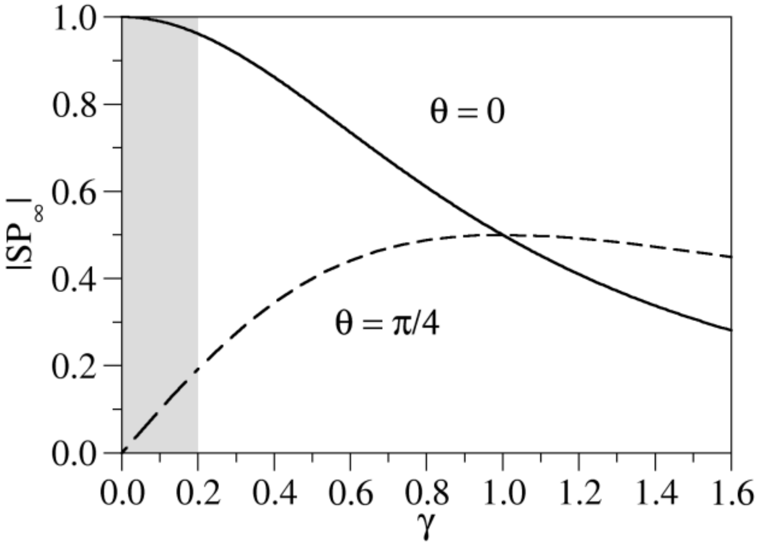

Figure 3. Absolute value of the asymptotic spin projection as a function of the dimensionless SOC parameter for initially polarized ($\theta = 0$) and fully unpolarized ($\theta = \pi/4$) wave packets.The gray area highlights the region with realistic values of γ according to our estimations.

Finally, let us discuss how the particular chirality of the molecule would affect our main results. The chirality in our model is directly related to the sign of the magnitude b, the pitch of the helix. If $b > 0$ ($b < 0$) we will be dealing with a right (left)-handed helix. In addition, the SOC parameter γ isinversely proportional to b, so the chirality of the molecule will define a particular sign of γ. Therefore,chirality will not affect the asymptotic SP_∞ of an initial state which is fully polarized [see Eq. (22)].Remarkably, for the most interesting situation, namely the polarization of an initially unpolarized state,SP_∞ is completely reversed, as a clear signature related to the molecular chirality [see Eq. (23)].

6. Conclusion

In summary, we have considered the coherent spin dynamics of electrons subject to the electric field created by a helical arrangement of dipoles. The electric field induces a Rashba-like SOC of electronsmoving along the helical axis. This coupling can be understood as the result of the interaction betweenthe electron spin and the magnetic field induced by the electric field in the rest frame of the electron.Once the model was presented, we were able to solve it exactly and to obtain a closed expressionfor the electron wave packet. We also calculated the spin projection onto the helical axis as a figureof merit to assess the spin dynamics in the molecular system. Remarkably, we found that the spinprojection reaches a steady state regime after a quick transient. We then obtained the asymptoticvalue for a fully spin-polarized initial wave packet and concluded that the electron becomes partiallydepolarized as time evolves. Similarly, an initially unpolarized wave packet gets partially polarized along the molecule axis due to the SOC induced by the helical arrangement of dipoles.

Acknowledgments

Work in Madrid was supported by the Spanish MINECO under Grants MAT2013-46308 and MAT2016-75955. RG and GC acknowledge financial support from the Volkswagen Stiftung via grantNo. 88366 (Spintronic Components based on Chiral Molecules). This work has also been partlysupported by the German Research Foundation (DFG) within the Cluster of Excellence "Center forAdvancing Electronics Dresden". We acknowledge the Center for Information Services and HighPerformance Computing (ZIH) at TU Dresden for computational resources.

Conflict of Interest

The authors declare that there is no conflict of interest regarding the publication of this manuscript.

References

1. Gohler B, Hamelbeck V, Markus TZ, et al. (2011) Spin selectivity in electron transmission through ¨self-assembled monolayers of double-stranded DNA. Science 331: 894–897.
2. Xie Z, Markus TZ, Cohen SR, et al. (2011) Spin specific electron conduction through DNAoligomers. Nano Lett 11: 4652–4655.
3. Mishra D, Markus TZ, Naaman R, et al. (2013) Spin-dependent electron transmission throughbacteriorhodopsin embedded in purple membrane. Proc Nat Acad Sci USA 110: 14872–14876.
4. Kettner M, Gohler B, Zacharias H, et al. (2015) Spin filtering in electron transport through chiraloligopeptides. J Phys Chem C 119: 14542–14547.
5. Mondal PC, Fontanesi C, Waldeck DH, et al. (2015) Field and chirality effects on electrochemicalcharge transfer rates: Spin dependent electrochemistry. ACS Nano 9: 3377–3384.
6. Rosenberg RA, Mishra D, Naaman R (2015) Chiral selective chemistry induced by naturalselection of spin-polarized electrons. Angew Chem Int Edit 54: 7295–7298.
7. Einati H, Mishra D, Friedman N, et al. (2015) Light-controlled spin filtering in bacteriorhodopsin.Nano Lett 15: 1052–1056.
8. Ben Dor O, Yochelis S, Mathew SP, et al. (2013) A Chiral-based magnetic memory device without a permanent magnet. Nat Commun 4: 2256.

9. *Michaeli K, Varade V, Naaman R, et al. (2017) A new approach towards spintronics—Spintronics with no magnets. J Phys-Condens Mat 29: 103002.*
10. *Kiran V, Mathew SP, Cohen SR, et al. (2016) Helicenes—A new class of organic spin filter. Adv Mater 28: 1957–1962.*
11. *Yeganeh S, Ratner MA, Medina E, et al. (2009) Chiral electron transport: Scattering through helical potentials. J Chem Phys 131: 014707.*
12. *Medina E, Lopez F, Ratner M, et al. (2012) Chiral molecular films as electron polarizers and polarization modulators. EPL 99: 17006.*
13. *Gutierrez R, D ´ ´ıaz E, Naaman R, et al. (2012) Spin-selective transport through helical molecular systems. Phys Rev B 85: 081404.*
14. *Guo AM, Sun QF (2012) Spin-selective transport of electrons in DNA double helix. Phys Rev Lett 108: 218102.*
15. *Gutierrez R, D´ıaz E, Gaul C, et al. (2013) Modeling Spin transport in helical fields: Derivation of an effective low-dimensional Hamiltonian. J Phys Chem C 117: 22276–22284.*
16. *Vager D, Vager Z (2012) Spin order without magnetism: A new phase of spontaneously broken symmetry in condensed matter. Phys Lett A 376: 1895–1897.*
17. *Gersten J, Kaasbjerg K, Nitzan A (2013) Induced spin filtering in electron transmission through chiral molecular layers adsorbed on metals with strong spin-orbit coupling. J Chem Phys 139: 114111–114130.*
18. *Guo AM, D´ıaz E, Gaul C, et al. (2014) Contact effects in spin transport along double-helical molecules. Phys Rev B 89: 205434.*
19. *Matityahu S, Utsumi Y, Aharony A, et al. (2016) Spin-dependent transport through a chiral molecule in the presence of spin-orbit interaction and nonunitary effects. Phys Rev B 93: 075407.*
20. *Guo AM, Sun QF (2012) Sequence-dependent spin-selective tunneling along double-stranded DNA. Phys Rev B 86: 115441.*
21. *Guo AM, Sun QF (2014) Spin-dependent electron transport in protein-like single-helical molecules. Proc Natl Acad Sci USA 111: 11658.*
22. *Pan TR, Guo AM, Sun QF (2016) Spin-polarized electron transport through helicene molecular junctions. Phys Rev B 94: 235448.*
23. *Jackson JD (1999) Classical Electrodynamics, Third Edition, New York: Wiley, 146.*
24. *Greiner W (2000) Relativistic Quantum Mechanics, Berlin: Springer.*
25. *D´ıaz E, Malyshev AV, Dom´ınguez-Adame F (2007) Interband optical transitions in DNA-like systems. Phys Rev B 76: 205117.*

·ISSN : 2372-0484

Ionic polymer-metal composites (IPMCs) and ionic polymer-polymer composites (IP²Cs): Effects of electrode on mechanical, thermal and electromechanical behaviour

Giovanna Di Pasquale 1, Salvatore Graziani 2, Chiara Gugliuzzo 1, and Antonino Pollicino 3,*
1 Dipartimento di Scienze Chimiche, Universitàdi Catania, V.le A.Doria 6, Catania, I-95125, ITALY
2 Dipartimento di Ingegneria Elettrica Elettronica e Informatica (DIEEI), Università di Catania, Viale A. Doria 6, Catania, I-95125, ITALY
3 Dipartimento di Ingegneria Civile e Architettura, Università di Catania, Viale A. Doria 6, Catania, I-95125, ITALY

ABSTRACT

Electro-active polymers (EAPs) are soft polymers that develop mechanical strain if subjected to electrical stimuli or, on the contrary, produce voltages if mechanically deformed. Their discovery has led to take into account their possible use as sensor-actuator for both bio-mimetic applications and traditional robotics. Ionic polymer-metal composites (IPMCs) and ionic polymer-polymer composites (IP^{2}Cs) belong to EAPs. Both of them are fabricated starting from an ionic polymer (typically Nafion$^{®}$117) but while in IPMCs the electrode is based on a metal (Ag, Au or Pt), IP2Cs are all-organic devices: in fact a conducting polymer (e.g.,poly(3,4-ethylendioxytiophene)-polystyrenesulfonate, PEDOT/PSS) is used as the electrode. In this work, a comparison has been done among the fabrication processes and the mechanical, thermal and electromechanical behaviour of IPMCs and IP^{2}Cs. The objective is to investigate the influence of the kind of electrode on the final properties of the devices, taking, also, into account the effect of different solvents, used for realizing the actuation process (H_2O or Ethylene Glycol). Reported results show that the performance of the obtained devices are function of manufacture parameters, the kind of electrode and solvent; consequently, taking into account the possible application, it is possible to choose the device that better meets specific requirements.

Keywords: electroactive polymers (EAPs); ionic polymer-metal composites (IPMCs); ionic polymer-polymer composites (IP^{2}Cs); thermal and mechanical analyses; electromechanical

1. Introduction

In recent years, much interest has been devoted to the research of innovative materials for the development of flexible electromechanical transducers and electroactive polymers (EAPs) have been extensively investigated because of their flexibility and lightness. Ionic Polymer-Metal Composites (IPMCs) are classified among EAPs [1–13]. They have been proposed for applications in various fields (soft robotic actuators and artificial muscles, dynamic sensors in the micro to macro-size range) due to the fact that they are light, soft, resilient, flexible, can be cut into any shape and size and are envisaged for biomedical applications. IPMCs show large bending deformation under low driving voltages, due to their capabilities to exhibit sensing and actuation properties; in fact, they bend if an electric field is applied across their thickness and, vice versa, they generate an electric reaction when subjected to a mechanical deformation. IPMCs (Figure 1) consist of an ionic polymer membrane (e.g., Nafion®117), metallized on both sides with a noble metal (e.g., silver (Ag), gold (Au) or platinum (Pt)). These metals are characterized by high cost and require complex deposition techniques in order to obtain the electrodes. For these reasons, a novel class of all-organic electroactive polymers, called Ionic Polymer-Polymer Composites (IP^2Cs) have been fabricated realizing the electrodes by organic conductors (e.g., polyanyline, polypyrrole, poly(3,4-ethylendioxytiophene)-polystyrenesulfonate (PEDOT/PSS)), (Figure 1) [14–19]: they can operate, as IPMCs, both as electromechanical actuators and as sensors. This new kind of systems has a huge potential because develops flexible substrates by low production costs and maintains electromechanical coupling capability, low required voltage, high compliance, lightness and softness.While in IPMC the electro-mechanical transduction capability is due only to the migration inside the Nafion membrane of mobile ions (H_3O^+) and of the cation hydration shell water molecules (due to hydration of the sample) (Figure 1b), in IP^2C, besides to these phenomena, the presence of the conductive polymer based electrodes, that can deform during red-ox reactions, can contribute to the electro-mechanical transduction. In both systems device actuation is obtained by the application of an electric field to the electrodes that mainly generates the motion of free cations through the membrane.

In this work, the authors compare the fabrication processes and properties of IPMCs and IP^2Cs, manufactured starting from Nafion®117 as the ionic polymer. While in IPMCs the electrode is based on Pt as metal, in IP^2Cs, the electrode element has been obtained directly polymerizing a conducting polymer (PEDOT/PSS) on Nafion®117. At present, the prevailing method to fabricate IPMCs requires depositing noble metals onto a cation-exchange film through chemical deposition technology in an electroless plating process. Moreover to improve the performances, additional post-processes have been utilized such as several cycles of Pt electroless plating [3] and using of dispersing agents [2,4,12,20–24]. In fact, an increase in the number of Pt electroless plating steps determines an increase in the thickness of the electrode and it is known that the amount of particles and the interfacial area increase proportionally to the thickness of the electrode. A larger conductor–polymer interface area influences the capacitance of the electric double layer and, adding more particles to the electrode, the performance of the device increases. Regarding the effect of dispersing agents, it is known that, to achieve high efficiency for IPMCs, it is necessary to reduce or eliminate the water leakage out of the surface electrode so water transport within the IPMC can be more effectively utilized for actuation. The decreasing of water contained in the polymer membrane is due to leakage out of the electrode’s porous surface and electrolysis and, to avoid this loss, it is necessary to obtain a uniform surface of the electrode. Due to a platinum particles coagulation process, in the IPMC, the surface of the electrode is not uniform but the use of dispersing agents, (introduced during chemical reduction processes) alleviates this phenomenon, enhancing the dispersion of platinum particles within the ionic polymer, controlling their size and reducing coagulation. By this procedure a better metallic particle dispersion in the polymer (the better the distribution, the lower the surface resistance) with smaller average particle sizes and more uniform distribution can be obtained. Obviously, if the distribution is uniform, it will be more difficult for water to pass through the electrode layer and the water leakage out of the surface electrode will be reduced.

Relatively to manufacture of IP^2Cs, poly(3,4-ethylenedioxythiophene)-poly(styrenesulfonate) (PEDOT:PSS) has been used as organic conductor, because it is one of the best known conducting polymers. In fact, it shows excellent electrical conductivity as well as processability. At first, drop-casting deposition techniques were used starting from Nafion®117 using different commercial formulations of PEDOT/PSS as electrode material (CLEVIOS ™ PH500, CLEVIOS ™ PHCV4, CLEVIOS ™ PH510, all by Baytron®) [17]. As for IPMCs, problems raised both because of loss of water by decomposition and evaporation when these devices operated in air [2,4]. The problem could be overcome rehydrating the device. Unfortunately, in IP²Cs manufactured by this technique, the organic electrodes delaminated and degraded during the hydration with the solvent. In a previous work [19], to improve the adhesion between Nafion®117 and conducting polymer and avoid the degradation of the electrode during the rehydration, the organic conducting polymer (PEDOT/PSS) was directly polymerized on the Nafion®117 surface by oxidative polymerization of the monomer 3,4-ethylendioxytiophene, EDOT.

As already mentioned, the actuation behaviour of IPMCs and IP2Cs is driven by the solvent movement inside the membrane [25] and, consequently, it is fundamental the electrochemical stability of the solvent. Water is widely utilized as inner solvent but during the applications it can evaporate or decompose in hydrogen and oxygen due to electrolysis process when applied voltages are higher than 1.3 V. Both phenomena result in a deterioration of the actuation performances. This problem can be overcome by using solvents other than water as, e.g., Ethylene Glycol (EG) [26–29]: in fact, it consists of polar molecules, like water, but has a high boiling point (197.6 °C) and can be subjected to relatively high voltages, without electrolysis. Consequently, the devices can show higher durability than the ones with water, even if the actuation response can be slower due to higher viscosity (16.1×10^{-3}Pa·s) and lower conductivity (1.07 mS·cm^{-1}) of EG with respect of water (1.00×10^{-3} Pa·s and 5.5 mS·cm^{-1}). Moreover, it is known that an improvement of the properties of PEDOT/PSS can be obtained by chemical treatment that involves the addition of co-solvent. It has been reported [30] that the strong electron-phonon coupling of PEDOT/PSS, that results in a low carrier mobility at room temperature, can be modified using EG as co-solvent. The incorporation of EG in PEDOT/PSS makes it possible to decouple electrons and phonons, enhancing the electrical properties of the conducting polymer. It can be argued therefore that by using EG in IP²Cs, instead of water, a beneficial effect on the actuation properties of the devices can be obtained.

All the obtained IPMCs and IP²Cs, manufactured using different solvents (H_2O and EG), have been characterized by scanning electron microscopy (SEM), dynamical mechanical (DMA) andthermogravimetric (TGA) analyses and electromechanically tested as actuators. A study of structure-property relationships in these devices has been done in function of the different kind of electrode and solvent and, finally, a comparison of different advantages and disadvantages in the application of IPMCs and IP²Cs concludes the work.

The paper is organized as follows: in Materials and Method section, we present IPMC and IP²C fabrication procedures and the techniques adopted for their morphological, dynamical mechanical, thermogravimetric and electromechanical characterization. In the Results and discussion section, we comment and compare the obtained data and analyse advantages and disadvantages in the use of IPMCs and IP²Cs. The last section is left for conclusions.

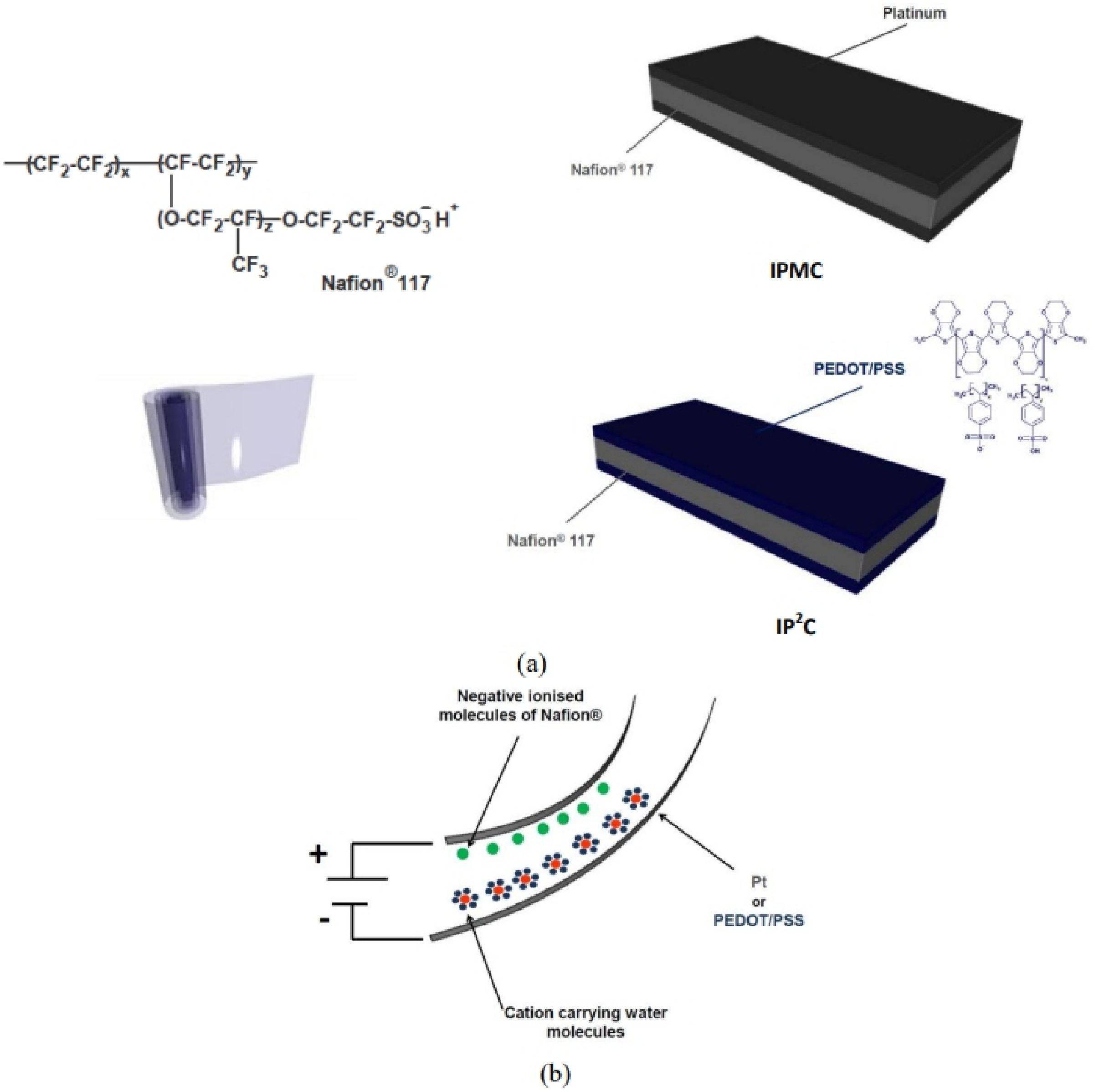

Figure 1. IPMC and IP^{2}C fabrication technique (a) and interaction of charges within the IPMC and IP2C (b).

2. Materials and Method

2.1. Membrane Preparation

All devices have been realized starting from Nafion®117 (a fluorocarbon membrane (thickness 178 µm), produced by Dupont and distributed by Sigma-Aldrich Group) (Figure 1a). All other reagents are commercial materials (Alfa Aesar Company) and were used without purification. A scheme of IPMC and IP^{2}C fabrications is reported in Figure 1a. To manufacture IPMCs, the experimental procedure is well documented [1–4,12,13] and includes roughening and cleaning of the Nafion® film, ion-exchange with tetrammineplatinum chloride ($Pt(NH_3)_4Cl_2$) and double chemical reduction (respectively a primary plating by sodium borohydride ($NaBH_4$) and a secondary plating by hydroxylamine hydrochloride, NH_2OH-HCl, and hydrazine, NH_2NH_2). In particular, IPMCs have been manufactured in presence, as dispersing agent, of polyvinylpyrrolidone (PVP10, M_w = 10000, 0.001 M, added either during the primary and the secondary plating) and by 3 sequential primary platings (adsorption for 20 hours in $Pt(NH_3)_4Cl_2$ solution/reduction by NaBH4). The formation of reduced platinum resulted in metallic grey layers deposited on both surfaces of the Nafion®membrane.

Regarding fabrication of IP^2Cs, a typical film deposition experiment [19,31,32,33] is based on the formation of the organic conductor electrode by polymerization in situ (1 h) of PEDOT on Nafion®117 film starting from 3,4-ethylendioxytiophene (EDOT) and sodium polystyrene sulfonate (NaPSS, added to improve the solubility of EDOT). Upon addition of $Fe(NO_3)_3 \cdot 9H_2O$, EDOT polymerized leading to a dark blue layer deposited on both sides of the membrane piece. The membrane, rinsed with double distilled water, has been boiled in H_2SO_4 1 M (1 h), to perform the exchange of Fe^{3+} with H_3O^+ions, and then in H_2O (1 h). In order to obtain IPMC and IP^2C with EG as solvent, water has been removed drying the devices at 100 °C for 24 h, then the devices have been soaked overnight in a beaker containing EG and, at last, heated to 60 °C for 1 h. All manufactured samples are listed in Table 1 (as references, pure Nafion®117 membranes, soaked with the H_2O and EG, have been used).

Table 1. Manufactured samples.

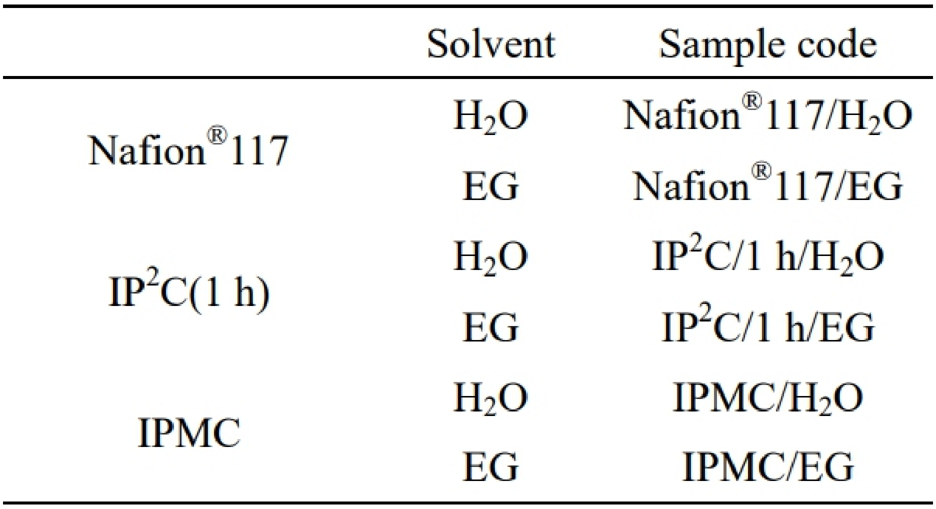

	Solvent	Sample code
Nafion®117	H_2O	Nafion®117/H_2O
	EG	Nafion®117/EG
IP^2C(1 h)	H_2O	IP^2C/1 h/H_2O
	EG	IP^2C/1 h/EG
IPMC	H_2O	IPMC/H_2O
	EG	IPMC/EG

2.2. Characterization

The solvent uptake level of the films, determined to find out the water absorbing capacity, has been calculated by the difference between the weight of the swollen membrane (W_1) and the dried sample (100 °C for 24 h) (W0) using the following equation:

$$\text{Solvent uptake (\%)} = [(W_1 - W_0)/W_0] \times 100\% \tag{1}$$

SEM (Scanning Electron Microscopy) micrographs have been obtained using a Cambridge 90 instrument equipped with an energy dispersive X-ray microanalysis (EDX) facility. The surface morphology and cross-sectional view (obtained on frozen-fractured samples) of the electrode layers

(PEDOT/PSS in IP^2C and Pt in IPMC) have been examined. The dynamical mechanical analyses (DMA) of all samples have been performed by a 2000 TA DMA produced by Triton Technology Ltd. The frequency dependence of the modulus of the membranes has been evaluated, in tension mode, by applying a sinusoidal force in the range 0.1–100 Hz (T = 25 °C). All the tested specimens have rectangular shape. The analyses have been performed on membranes fully solvent saturated. Solventon the surfaces of specimens has been wiped off with absorbent paper to remove the adhering excess before the measurements.

Thermogravimetric analyses (TGA) have been carried out on a Shimadzu model DTG-60 instrument. TGA curves have been recorded at a heating rate of 10 $°C·min^{-1}$ under a nitrogen atmosphere (20 $ml·min^{-1}$) from 35 to 700 °C, in hydrated conditions. Analyzed sample mass varied between 8.0 and 11.0 mg.

To compare and analyze the device performances as actuators, the samples have been cut in strips of size 2.6 cm ×0.5 cm; a swept signal of amplitude 2 V and a growing frequency (from 0.1 to 50 Hz) have been applied through the measurement setup. Absorbed current and the sample free deflection have been measured through a conditioning circuit and by means of a laser proximity sensor, respectively. The Bode diagrams of sample displacement and sample resonance frequency have been evaluated.

3. Results and Discussion

In the obtained devices, Nafion®117 has been used as base material, while the electrode has been realized by metallic platinum in IPMC and PEDOT/PSS in IP^2Cs (by polymerization in situ). Regarding the manufacturing procedures, the one required to produce IPMC is complex, long and expensive while for IP^2C it is easier, faster and cheaper. In fact, only 1 day is required for fabricating IP_2C instead of 5 days necessary for IPMC; moreover the manufacturing cost is 0.37 €/cm^2 for IP^2C against 7.55 €/cm^2 for IPMC. The adhesion of the electrode on Nafion matrix it is very good in both devices: the electrodes adhere strongly giving a grey metallic layer of platinum in IPMC and a blue-black appearance of PEDOT/PSS in IP^2C, respectively. The very good adhesion has been confirmed by the possibility of rehydrating both the devices after their use without any evidence of degradation. In the case of IPMC, platinum particles, deposited on both the surfaces of Nafion®117, fill some parts of the membrane channels and the measured electrode layer is about 15–20 μm [2,27]. In the case of IP^2Cs, probably, the sulfonic acid groups of Nafion®117 may serve as counter-ions in the PEDOT polymerization process so that the polymerization inside the Nafion membrane, also in this case, cannot be excluded [33]; the film is uniform and compact and the thickness is about 8 μm (Figure 2).

It is known that the actuation in IPMCs and IP^2Cs is driven by the migration of solvent and ions. In Figure 3, the solvent uptake of the devices with different inner solvent (calculated as weight percentage) is reported. Relatively to the influence of electrode, in IPMCs, the layer of platinum is hicker than PEDOT/PSS in IP^2Cs but, as it is possible to observe in Figure 2, the surface shows some fractures, consequently the devices can absorb an higher quantity of solvent. Regarding the kind of solvent, due to a strong chemical interaction between Nafion®117 and EG [26,27] and to the high molecular weight of EG, it is possible to observe that IPMCs and IP2Cs absorb more EG than H_2O.

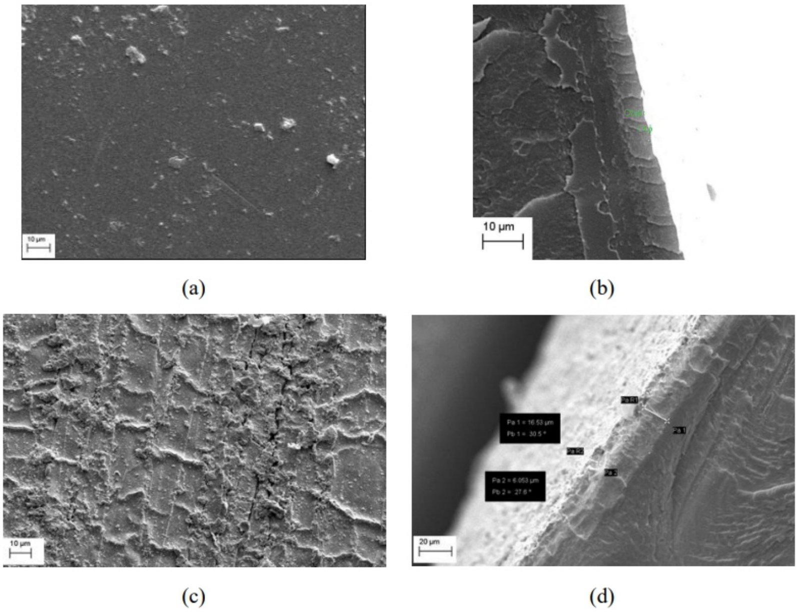

(a) (b)

(c) (d)

Figure 2. SEM images of surface and cross-sectional view of IP^{2}C/1h (a, b) and IPMC (c, d).

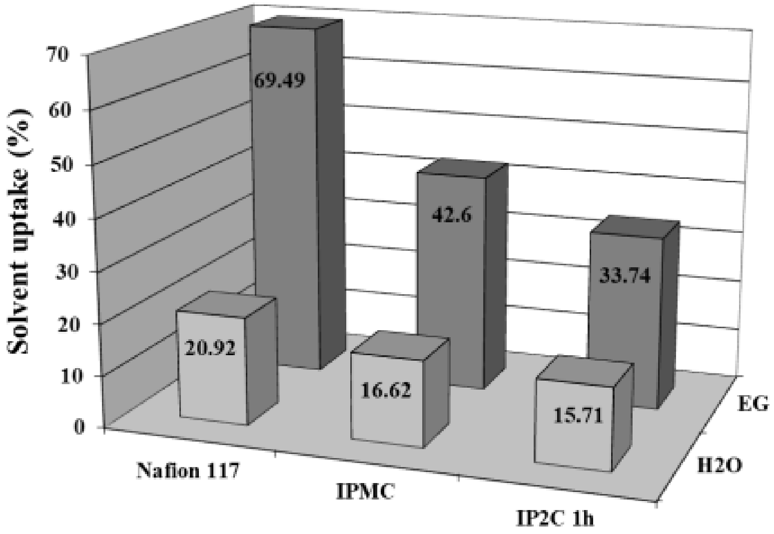

Figure 3. Solvent uptake of Nafion®117, IPMC and IP^{2}C with different inner solvent (H_2O and EG).

When such composite are investigated TGA and young modulus determination are routinely performed. In fact TGA can give information on the amount and nature of the solvent and on the degradation step of the membrane. Also, the low temperature region of the TGA scan can give information on the capability of the device in retaining the solvent because of the porous nature of the electrodes [34,35]. The DMA, through the modulus determination can give insight on the electromechanical transduction performance of the composite [36].

In TGA, the sample is heated in a furnace and the weight loss is measured as a function of the temperature. The thermal stability of IP^{2}C and IPMC, in H_2O and EG as solvent, has been studied. The results have been reported as percentage of undegraded sample and derivative weight loss (DrTGA) as function of temperature. Such an investigation allows for obtaining some information relatively to thermal stability of the devices and, by comparison with the Nafion®117, to the effect that the kind of electrode determines for what concerns the rate of solvent loss from the device as the temperature increases. As shown in Figure 4, in Nafion®117/H_2O membrane it is possible to individuate different step relative to mass loss: the first (range 25–290 °C) can be attributed mainly to the loss of free water or physically adsorbed water; the second (range 290–400 °C) is associated with a desulfonation process (H_2O(g), SO_2(g) and CO_2(g) are liberated during the thermolysis); the third stage (range 400–470 °C) is related to side-chain decomposition and, at last (470–560 °C), the one due to PTFE backbone decomposition (with HF, SiF4 and COF2, typical gases liberated) [19,37,38,39].In IP^{2}C and IPMC, the electrode (PEDOT/PSS and platinum, respectively) exerts a barrier effect which slows the loss of water thereby extending the operating temperatures of the device and determining an increase of the “thermal stability” of the system. Moreover, regarding the degradation processes, the obtained results show that the processes of thermal degradation of the Nafion®117 overlap with those of the conductive polymer PEDOT/PSS in IP$_2$C and of platinum in IPMC. In particular, when H_2O is used as solvent, in the devices (Figure 4a) is firstly noted that, on increasing the temperature virgin Nafion®117 film shows a progressive increase in the rate of water loss (that reaches the maximum speed at about 70 °C). On the contrary, IP^{2}C and IPMC loss the solvent with a constant speed throughout the temperature range of 25–290 °C (no peak in DrTG). These results can be interpreted in terms of electrode uniformity and compactness. Conductive polymer in IP$_2$C and platinum in IPMC produce electrodes that more efficiently act as a barrier, making more difficult for water to pass through (granular damming effect). Consequently, the rate of the water leakage out the surface electrode is reduced. Relatively to DrTGA data, it is possible to observe that, in IP^{2}Cs, in the range 290–400 °C the decomposition is associated with a desulfonation process and interests both sulfonic functions of Nafion®117 and PEDOT/PSS. In IPMC, the presence of platinum instead of PEDOT/PSS, determines a higher stability of the device probably because the desulfonation process is limited only to sulfonic function of Nafion®117. At temperature higher than 550 °C the metallic layer in IPMC still acts as a barrier for degradation products. In Figure 4b, TGA and DTG of IPMC and IP^{2}Cs are reported when EG is used as solvent. In the range 100–200 °C, due to the extremely hygroscopic nature of EG and to the mass loss of free or physically adsorbed EG, it is possible to observe a large weight loss in Nafion®117/EG, IPMC/EG and IP^{2}C 1 h/EG with respect to ones with H_2O (Figure 4a). As can be observed from the DrTG of the devices containing EG, there are two steps in solvent loss: the first is relate to the hygroscopically adsorbed water and shows a maximum rate of loss at about 90 °C. The second, with a maximum rate of weight loss at about 150 °C, it is relative to the EG loss.

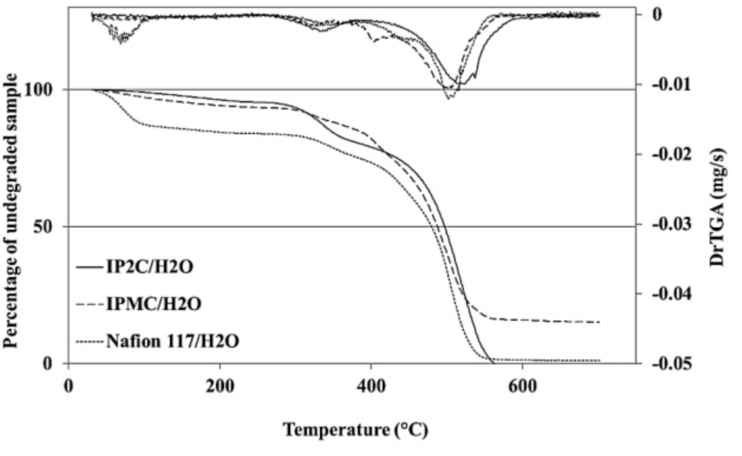

(a)

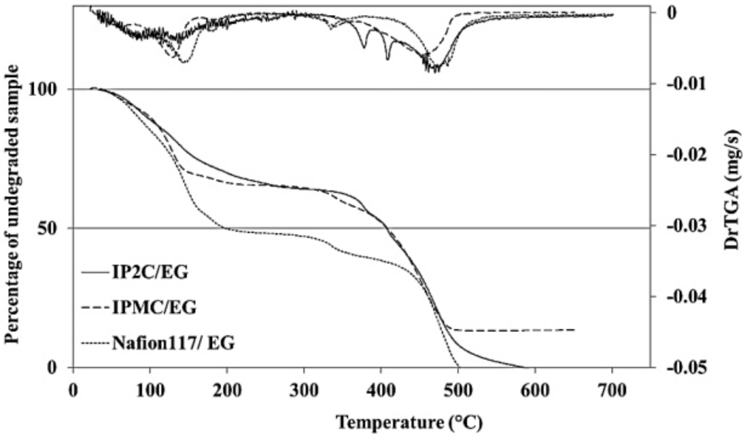

(b)

Figure 4. TGA and DrTGA of Nafion®117, IP^{2}C/1 h and IPMC with H_2O (a) and EG (b) as solvent.

Regarding the dynamical mechanical analyses, in most cases, the moduli values measured by DMA do not agree well with that obtained from mechanical testing methods [40], so they are utilized only for screening the material properties for the purposes of research and optimization of processing conditions. In this work, the results relative to a native Nafion membrane (Young's modulus 0.09–0.25 GPa) are in good agreement with those reported in the literature [41–44]. For DMA measurements of the samples, the tension mount (particularly useful for fibres, elastomers and films) has been used and a sinusoidal tensile force has been applied to the rectangular samples in the range from 0.1 to 100 Hz, at a working temperature of 25 °C, in hydrated condition. DMA measures stiffness and damping, so measurements of storage modulus (E'), loss modulus (E'') and tan delta (tan δ = E''/E') have been obtained and compared to determine the influence of the different kind of electrode and solvent on the mechanical properties of IPMCs and IP^{2}Cs In Figure 5, a comparison of the frequency response of storage modulus in IP^{2}Cs and IPMCs in presence of H_2O and EG is reported using as reference Nafion®117 membrane. In all devices, the presence of the electrode (Pt in IPMC and PEDOT/PSS in IP^{2}C) determined an increase of the storage modulus respect to one of Nafion®117. In particularly, using H_2O as solvent, at low frequencies, IP^{2}C shows a higher storage modulus than IPMC, while at frequencies superior to 1 Hz an inversion is observed. Moreover, IPMC shows high storage and loss modulus simultaneously (generally the relationship is inverse) revealing both stiff and damping characteristics.

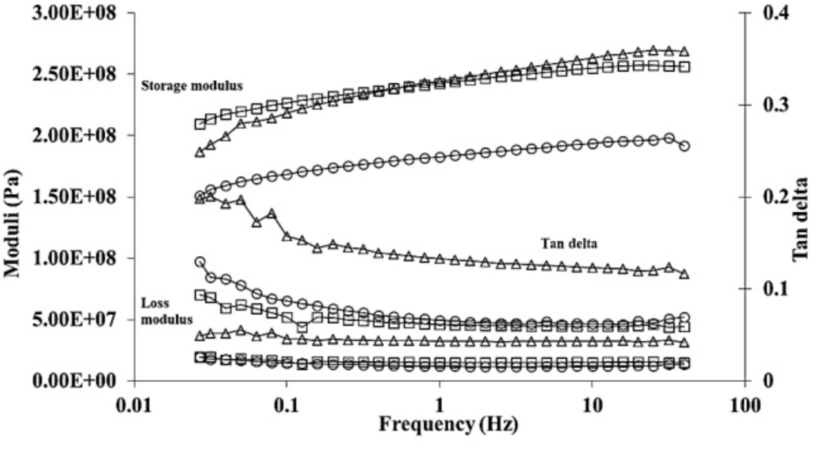

(a)

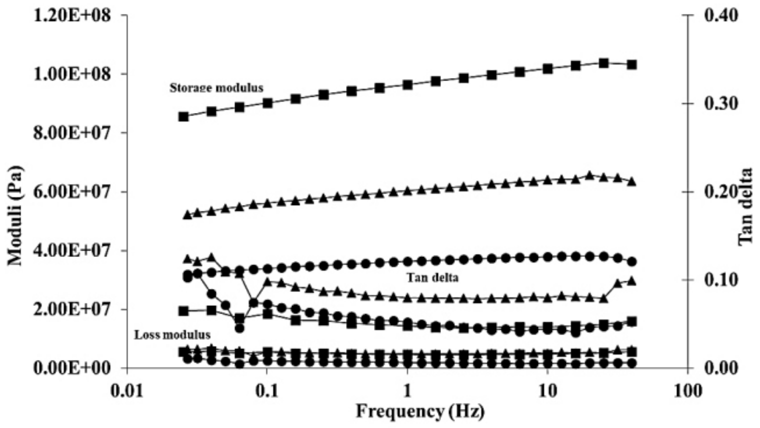

(b)

Figure 5. A comparison of storage modulus, loss modulus and tan delta for Nafion®117 (○), IP²C/1 h (□) and IPMC ( ) in H_2O (a) and EG (●, ■ and ▲ respectively) (b) as a function of frequency.

It is important to observe as the kind of solvent influences the mechanical properties of a device. In fact, a solvent acts as a plasticizer, with the consequence that the flexibility and elasticity of the film increase. The plasticizer works by reducing the interactions among the macromolecules and thereby increasing chain mobility, which, in turn, leads to a softening or plasticization of the polymeric material. In our devices, the solvent present in the polymeric matrix interferes with chain-to-chain secondary bonding and the chains acquire greater mobility, increasing the free volume [45]. The samples with water as solvent exhibit higher storage modulus than those with EG. It is due to the fact that EG has a higher plasticizing effect with respect to H2O. It depends on the fact that EG has a lower vapour pressure and therefore it has greater permanence in the Nafion membrane leading to a clear decrease of the storage modulus values for the devices with EG as solvent compared to the hydrates ones (Figure 5). Regarding the electromechanical characterization of the devices, it has been carried out through the setups described in the methods section. The devices were tested in a cantilever configuration: one end has been fixed in a clamp fitted with copper foil electrodes to contact the conductive metal surface of the sample, while the other end is free in the case of deflection measurement. In particular, the free deflection, produced when a voltage signal has been imposed across the strip thickness, has been detected in order to compare the performances of the different devices as motion actuators. The obtained data are reported in Table 2.

Table 2. Obtained values of absorbed current, deformation and resonance frequency of IPMCs and IP²Cs using different solvent (H_2O or EG).

	Absorbed current (A)	Maximum deformation (mm)	Resonance frequency (Hz)
IP²C/H_2O	0.62	2.4	37.8
IPMC/H_2O	0.1	1.8	19.8
IP²C/EG	0.05	0.1	42.1
IPMC/EG	0.08	0.7	17.95

When H_2O is used as solvent, IP^2C shows higher absorbed current than IPMC with a consequent higher deformation. It has to be noted that using H_2O as solvent, due to evaporation and electrolysis processes, the content of water inside the membranes changes during the measurements, generating a decreasing trend in the deformation thus changing the actuator performances (Figure 6). The consequence is that for the IP^2Cs and IPMC with H_2O as solvent, it is always necessary to re-hydrate the devices after the utilization.

In Figures 6 and 7, the Bode diagrams of the fabricated devices are reported: they permit to examine the frequency response of a system. In particular, by these diagrams, it is possible to determine the frequency at which the response amplitude is a relative maximum (resonance frequency). The diagrams report both the magnitude and the phase as a function of the investigated frequency range. From the diagrams and the data in Table 2 it is possible to observe that IP^2C are characterised, with respect to IPMC, by a larger value of the resonance frequency. Such a trend is shown by both water and EG based devices.

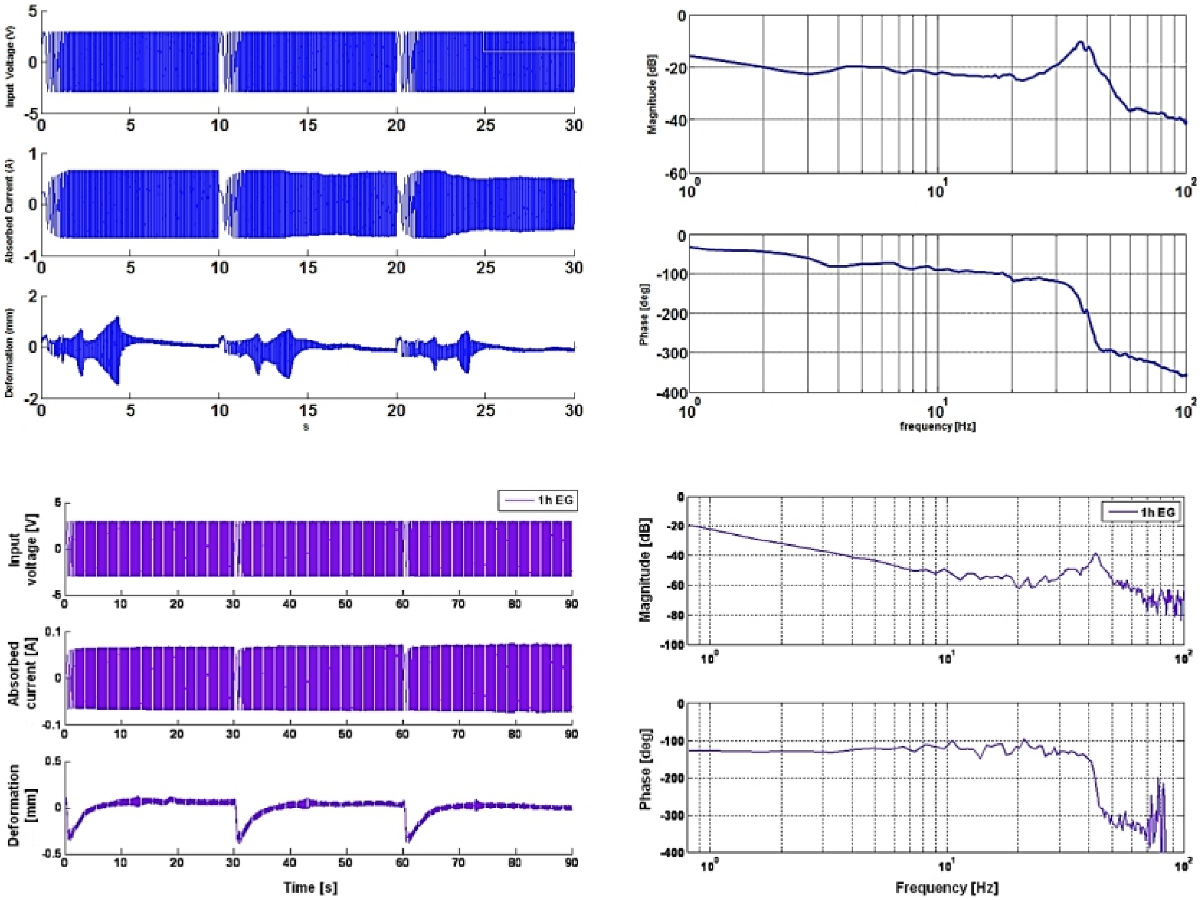

Figure 6. Actuator frequency sweep measurement (input and output signal) and Bode diagram of IP^2C in H_2O (blue) and EG (violet).

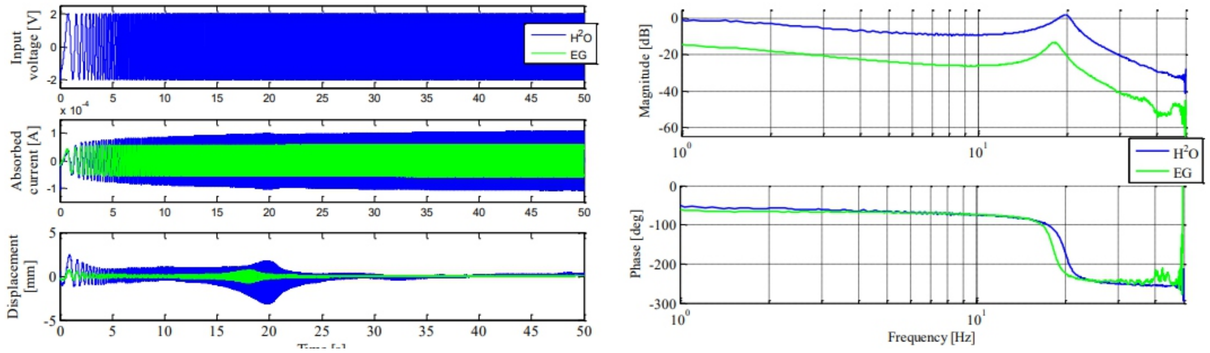

Figure 7. Actuator frequency sweep measurement (input and output signal) and Bode diagram of IPMC/H_2O (blue) and IPMC/EG (green).

When EG is used as solvent (Table 2), it is possible to observe that the absorbed current and, consequently, the deformation of devices, are lower with respect to the ones obtained using H_2O. These results can be explained taking into account several factors: EG has a viscosity higher than water (about 16 times), higher boiling point (197.6 °C) (no evaporation during the measurements) and electrolysis phenomena are absent. Moreover, the surface resistance increases also because the electrode, after swelling with EG, could be degraded due to expansion phenomena [27]. Finally, EG containing devices show lower capacity to accumulate charges close to the electrodes (as indicated by the magnitude of the absorbed currents). This consideration is in agreement with observed deformation values that are higher for devices containing water regardless of the device type. The unusually high value of absorbed current recorded in the case of the IP^2C/H_2O sample can be attributed to the presence at membrane/conductive polymer interface of pseudocapacitive phenomena [46]. Consequently, the actuation response is lower than that with H_2O but they have higher durability. Moreover, while samples with water cannot be retested after a first measurement set, unless after soaking them again in water for rehydration, the EG containing ones do not need to be rehydrated, and thus the samples can be tested to obtain their complete characterization. Actuator frequency swept measurements and Bode diagram of the devices EG are reported in Figure 7.

4. Conclusion

In this paper, the fabrication processes, the mechanical, thermal and electromechanical behaviour of IPMCs and all organic electroactive transducers (IP^2Cs), fabricated starting from Nafion®117, have been studied and compared. Regarding the manufacturing procedures, the one required to produce IPMC is complex, long and expensive while for IP^2Cs it is easier, faster and cheap. In fact, only 1 day is required to fabricated IP^2C instead of 5 days necessary for IPMC; moreover the manufacturing cost is 0.37 €/cm^2 for IP^2C against 7.55 €/cm^2 for IPMC.Regarding the influence of the kind of electrode (Pt in IPMC and PEDOT/PSS in IP2C), it exerts a barrier effect influencing the solvent loss in the devices during the operating times. It is possible to observe, by solvent uptake data, that in IPMC there is a higher loss of solvent due probably to the fractures present in the surfaces of Pt electrode with respect to the unbroken PEDOT/PSS film in IP^2Cs. Comparing the TGA data, the thermal properties of both the devices don't show differences up to 150 °C while, at higher temperatures, IPMC shows higher thermal stability due to the presence of platinum on the surface.

DMA results show that storage modulus of IPMC is lower than the one of IP^2C. Also in this case it can be attributed to the broken and not uniform surface of Pt electrode in IPMC as shown by SEM. Relatively to the electromechanical transduction, EG based devices absorb much less current with a negative effect on the corresponding deformation. Such a clear change is not, anyway, observed in the comparison of IP^2Cs with IPMCs.If EG is used as solvent instead of water, the solvent uptake, the thermal stability and the storage modulus decrease both in IPMC and IP^2C with respect to the ones obtained using water but, when used as actuators, the devices show higher durability, there is not necessary to rehydrate and it is possibility to reach a constant deformation.In summary, the performances of IPMCs and IP^2Cs based on Nafion® 117 are function of kind of electrode and solvent, without highlighting a significant superiority in the overall performance of one of the two technologies. Nevertheless, the lower production times and costs suggest that IP^2Cs are a possible alternative to IPMCs.

Acknowledgments

The authors gratefully acknowledge the support of this work Dr. Roberta Puglisi for DMA analysis and Ing. Alberta Latteri for SEM microphotographs.

Conflict of Interest

All authors declare no conflicts of interest in this paper.

References

1. Shahinpoor M, Bar-Cohen Y, Simpson JO, et al. (1998) Ionic polymer-metal composites (IPMCs) as biomimetic sensors, actuators and artificial muscles—review. Smart Mater Struct 7: R15.
2. Shahinpoor M, Kim KJ (2001) Ionic polymer-metal composites: I. Fundamentals. Smart Mater Struct 10: 819.
3. Pak JJ, Cha SE, Ahn HJ, et al. (2001) Fabrication of Ionic Polymer Metal Composites by Electroless Plating of Platinum. Proceedings of the 32nd ISR (International Symposium on Robotics).
4. Kim KJ, Shahinpoor M (2003) Ionic polymer-metal composites: II. Manufacturing techniques.Smart Mater Struct 12: 65.
5. Shahinpoor M, Kim KJ (2005) Ionic polymer-metal composites: IV. Industrial and medical applications. Smart Mater Struct 14: 197.
6. Bonomo C, Fortuna L, Giannone P, et al. (2006) A model for ionic polymer metal composites as sensors. Smart Mater Struct 15: 749.
7. Bonomo C, Fortuna L, Giannone P, et al. (2006) A nonlinear model for ionic polymer metal composites as actuators. Smart Mater Struct 16: 1.
8. Del Bufalo G, Placidi L, Porfiri M (2008) A mixture theory framework for modeling the mechanical actuation of ionic polymer metal composites. Smart Mater Struct 17: 045010.
9. Punning A, Johanson U, Anton M, et al. (2009) A distributed model of ionomeric polymer metal composite. J Intel Mat Syst Str 20: 1711–1724.
10. Pugal D, Jung K, Aabloo A, et al. (2010) Ionic polymer-metal composite mechanoelectrical transduction: review and perspectives. Polym Int 59: 279–289.
11. Kruusamae K, Brunetto P, Graziani S, et al. (2010). Self-sensing ionic polymer-metal composite actuating device with patterned surface electrodes. Polym Int 59: 300–304.

12. Bonomo C, Bottino M, Brunetto P, et al. (2010) Tridimensional ionic polymer metal composites: optimization of the manufacturing techniques. Smart Mater Struct 19: 055002.

13. De Luca V, Digiamberardino P, Di Pasquale G, et al. (2013) Ionic electroactive polymer metal composites: Fabricating, modelling, and applications of postsilicon smart devices, review. J Polym Sci Pol Phys 51: 699–734.

14. Di Pasquale G, Fortuna L, Graziani S, et al. (2008) All organic actuation and sensing devices.2008 IEEE Instrumentation and Measurement Technology Conference.

15. Di Pasquale G, Fortuna L, Graziani S, et al. (2009) All-Organic Motion Sensors: Electromechanical Modeling. IEEE T Instrum Meas 58: 3731–3738.

16. Fortuna L, La Rosa M, Nicolosi D, et al. (2009) Demonstrators and multifunctional testbeds for organic semiconductor characterization. Eur Phys J Appl Phys 46: 12512.

17. Di Pasquale G, Fortuna L, Graziani S, et al. (2011) A study on IP2C actuators using ethylene glycol or EmI-Tf as solvent. Smart Mater Struct 20: 045014.

18. Di Pasquale G, Graziani S, La Rosa M, et al. (2013) IP2C sensor modeling. IEEE T Instrum Meas62: 1284–1291.

19. Di Pasquale G, Graziani S, Messina FG, et al. (2014) An investigation of the structure-property relationships in ionic polymer polymer composites (IP2Cs) manufactured by polymerization in situ of PEDOT/PSS on Nafion®117. Smart Mater Struct 23: 035018.

20. Kim KJ, Shahinpoor M (2001) The Synthesis of Nano-Scaled Platinum Particles (NSPP)—Their Role in Performance Improvement of Ionic Polymer-Metal Composite (IPMC) Artificial Muscles.Proc SPIE 4329, Smart Structures and Materials 2001: Electroactive Polymer Actuators and Devices.

21. Wu SH, Chen DH (2004) Synthesis of high-concentration Cu nanoparticles in aqueous CTAB solutions. J Colloid Interf Sci 273: 165–169.

22. Song X, Sun S, Zhang W, et al. (2004) A method for the synthesis of spherical copper nanoparticles in the organic phase. J Colloid Interf Sci 273: 463–469.

23. Kim KD, Han DN, Kim HT (2004) Optimization of experimental conditions based on the Taguchi robust design for the formation of nano-sized silver particles by chemical reduction method. Chem Eng J 104: 55–61.

24. Di Pasquale G, Graziani S, Pollicino A, et al. (2015) A vortex-shedding flowmeter based on IPMCs. Smart Mater Struct 25: 015011.

25. Bonomo C, Fortuna L, Giannone P, et al. (2005) A method to characterize the deformation of an IPMC sensing membrane. Sensor Actuat A-Phys 123: 146–154.

26. Nemat-Nasser S, Zamani S (2003) Experimental study of Nafion- and Flemion-based ionic polymer metal composites (IPMCs) with ethylene glycol as solvent. Proc SPIE 5051, Smart Structures and Materials 2003: Electroactive Polymer Actuators and Devices (EAPAD).

27. Pandita SD, Lim HT, Yoo YT, et al. (2006) The actuation performance of Ionic Polymer Metal Composites with mixture of ethylene glycol and hydrophobic ionic liquids as an inner solvent. J Korean Phys Soc 49: 1046–1051.

28. Akle BJ, Leo DJ (2004) On the relationship between the electric double layer and actuation in ionomeric polymer transducers. MRS Proceedings 855.

29. Groenendaal L, Jonas F, Freitag D, et al. (2000) Poly(3,4-ethylenedioxythiophene) and its derivatives: past, present and future. Adv Mater 12: 481–494.

30. Lin YJ, Ni WS, Lee JY (2015) Effect of incorporation of ethylene glycol into PEDOT:PSS on electron phonon coupling and conductivity. J Appl Phys 117: 215501.

31. Higgins SJ, Lovell KV, Gamini Rajapakse RM, et al. (2003) Grafting and electrochemical characterisation of poly-(3,4-ethylenedioxythiophene) films, on Nafion and on radiation-grafted *polystyrenesulfonate–polyvinylidene fluoride composite surfaces. J Mater Chem 13: 2485.*

32. Cho MS, Seo HJ, Nam JD, et al. (2007) An electroactive conducting polymer actuator based on NBR/RTIL solid polymer electrolyte. Smart Mater Struct 16: S237.

33. Li L, Drillet JF, Dittmeyer R, et al. (2006) Formation and characterization of PEDOT-modified Nafion 117 membranes. J Solid State Electr 10: 708–713.

34. Yue L, Xie Y, Zheng Y, et al. (2017) Sulfonated bacterial cellulose/polyaniline composite membrane for use as gel polymer electrolyte. Compos Sci Technol 145: 122–131.

35. Kim J, Bae SH, Kotal M, et al. (2017) Soft but Powerful Artificial Muscles Based on 3D Graphene–CNT–Ni Heteronanostructures. Small 13: 1701314.

36. Duncan AJ, Leo DJ, Long TE (2008) Beyond Nafion: Charged Macromolecules Tailored for Performance as Ionic Polymer Transducers. Macromolecules 41: 7765–7775.

37. Suroweic J, Bogoczek R (1988) Studies on the thermal stability of the perfluorinated cation-exchange membrane Nafion-417. J Therm Anal Calorim 33: 1097–1102.

38. Samms SR, Wasmus S, Savinell RF (1996) Thermal Stability of Nafion® in Simulated Fuel Cell Environments. J Eletrochem Soc 143: 1498–1504.

39. De Almeida SH, Kawano Y (1999) Thermal behaviour of Nafion membranes. J Therm AnalCalorim 58: 569.

40. Lee-Sullivan P, Dykeman D (2000) Guidelines for performing storage modulus measurements using the TA Instruments DMA 2980 three-point bend mode I. Amplitude effects. Polym Test 19:155–164.

41. Tang Y, Karlsson AM, Santare MH, et al. (2006) An experimental investigation of humidity and temperature effects on the mechanical properties. Mater Sci Eng A 425: 297–304.

42. Abuin GC, Nonjola P, Franceschini EA, et al. (2010) Characterization of an anionic-exchange membranes for direct methanol alkaline fuel cells. Int J Hydrogen Energ 35: 5849–5854.

43. Zhu Z, Chen H, Li B, et al. (2010) Characteristics and Elastic Modulus Evaluation of Pd-Nafion Ionic Polymer-Metal Composites. Adv Mater Res 97: 1590–1594.

44. Kim JD, Oba Y, Ohnuma M, et al. (2010) Physico-chemical properties of temperature tolerant anhydrous nafion-benzimidazole blend membrane. Solid State Ionics 181: 1098–1102.

45. Immergut EH, Mark HF (1965) Principles of Plasticization, In: Platzer NAJ, Plasticization and Plasticizer Processes, American Chemical Society, 1–26.

46. Aabloo A, De Luca V, Di Pasquale G, et al. (2016) A new class of ionic electroactive polymers based on green synthesis. Sensor Actuat A-Phys 249: 32–44.

·ISSN : 2372-0484

Optical and structural characterization of ZnSe thin film fabricated by thermal vapour deposition technique

Mohammed Tareque Chowdhury 1, Md. Abdullah Zubair 2,*, Hiroaki Takeda 3 , Kazi Md.Amjad Hussain 1, and Md. Fakhrul Islam 2
1Experimental Physics Division, Atomic Energy Centre, Bangladesh Atomic Energy Commission,Dhaka, Bangladesh
2 Department of Glass and Ceramic Engineering, Bangladesh University of Engineering andTechnology (BUET), Dhaka, Bangladesh
3School of Materials and Chemical Technology, Tokyo Institute of Technology, Tokyo, Japan

ABSTRACT

Zinc-selenide thin film was prepared on a soda-lime glass substrate by thermal vapor deposition technique. The X-ray diffraction data confirmed the cubic zincblende structure with apreferred orientation along (111) plane. Different models such as Debye-Scherrer, Size-Strain plot,Williamson-Hall, uniform stress deformation model and uniform deformation energy density modeland the so called approximation model were adopted to analyse the XRD data. Detailedmicrostructural parameters such as crystallite size, strain, stress, isotropic energy density, dislocationdenstiy were reported and discussed in comparison with scanning electron microscopy data. Thetransmission spectra was obtained by UV-Vis-NIR spectrometer in the range of 250–2500 nm atroom temperature. Important optical constantssuch as refractive index and dielectric constant wasestimated using Swanepoel’s envelope method. The same method was used to check the thin filmthickness which was found to be 374.9 nm and this thickness was further confirmed by ScanningElectron Microscopy (368.3 ± 19.1 nm). The optical band gap was estimated to be 2.64 eV. Thedispersion of refractive index was discussed interms of empirical Cauchy dispersion relation and thedispersion was further analysed by Wemple-DiDomenico Single oscillator model which providephysically meaningful parameters such as static refractive index, oscillator energy and dispersionenergy. Both the structural and optical data not only complemented each other but also implied thatgood quality Zinc-selenide thin film could be deposited on ordinary glass substrates.

Keywords: Zinc-selenide; thin film; texture analysis; pole-figure; transmission spectra; interference fringes; optical band gap; optical constants

1. Introduction

Zinc-selenide (ZnSe) is a II-VI group direct band gap compound semiconductor which is one of the most famous mono-chalcogenides because of its superior optical and semiconducting properties.Due to large band gap and optical transparency in the visible and infrared region, ZnSe can be usedas a window layer in thin film solar cells [1,2,3]. It can also be used for other optoelectronic devicessuch as, light emitting and laser diodes, luminescent devices etc. [4–7]. Many chemical and physical vapour processes are used for deposition of ZnSe thin films [8,9].

Sol-gel, spray pyrolysis, chemical bath deposition method involve complicated chemical reactions and at the same time chemicalprecursors have to be optimised to prepare single phase ZnSe thin film. In the chemical depositionprocess, the crystallinity and the surface morphology was not always suitable for optoelectronic andmany memory devices. The main advantage of thermal vapour deposition in comparison withchemical process is that stoichiometry can be directly transferred from the source powder to thesubstrate by evaporating source material. Numerous articles were published in the recent yearsregarding the optical and structural characterization of thermal vapour deposited (TVD) ZnSe thin film on different types of substrates: Si (100), fused silica glass, borosilicate glass, indium-tin-oxidecoated glass and soda-lime glass [6,10–20]. The vacuum pressure was also varied from a very largevalue (1 Pa for close space sublimation) to a very small value (3×10^{-5} Pa for PLD) depending onthe selection of different deposition systems [6,10–18,20,21,22]. The evolution of structural andoptical properties of the ZnSe thin films have been found to depend greatly on substrate specificationand vacuum pressure as well as on the substrate temperature and post-deposition thermal treatmentconditions. In a nutshell, a careful selection of process-parameters plays a pivotal role in attaining thedesired properties of thin films. Thus research opportunities in this arena are yet to be explored.

Recently, Hassanien et al. reported an elaborate optical characterization with in-depth quantitative model analysis for pulsed laser annealed TVD ZnSe where crystallinity was found toimprove significantly with increase in laser power from 10 to 30 W [6]. However, the major focus oftheir report was not concentrated towards the detailed crystallographic, geometrical, structural andmicrostructural parameter analysis in correlation with the optical response of the film. Similarly,Desai et al. discussed the details of the optical characteristics of a single TVD ZnSe film on glasssubstrate, where no structural data was presented in connection with the observed opticalparameters [12]. Khan et al. also reported the annealing temperature dependent XRD data of theTVD ZnSe thin film on borosilicate glass. Although (111) peak intensity was found to increase withthe annealing temperature from 350 to 500 °C, no (220) or (311) peak was observed in any of the thin film [13]. Hence, it was rather difficult to make any conclusive remark on the structure propertyrelation based on only a single peak. Absence of (220) and (311) peaks in ZnSe thin film was alsoreported elsewhere [21,22]. Similar type of structural data was also observed for TVD ZnSe thin filmon soda-lime glass substrate by Gullu et al.. Faint peaks corresponding to (220) and (311) planesappeared in the diffraction pattern only for post-deposition annealing treatment at 500 °C [23].However, temperature as high as 500 °C could have detrimental impacts on the thermo-mechanicaland chemical properties of soda-lime glass. Post-deposition annealing of TVD ZnSe thin film onglass substrate by Ashraf et al. was reported to substantially enhance the intensity of the (111) peakwith little effect on the existing (220) and (311) peaks at high angles with negligible intensities [20].Inadequate vacuum pressure could be the possible reason for (220) and (311) peaks to be faint. Aqiliet al. also reported similar XRD data for ZnSe thin film deposited by closed sublimation method [18].

Khairnar reported XRD data of TVD ZnSe on glass substrate where only (111) peak was observed [19]. No other structural data were reported in connection to the optical properties of thethin film. However, Zhang et al. reported excellent XRD patterns for pulsed laser deposited ZnSethin film on fused quartz and GaAs substrates, where all three (111), (220) and (311) peaks wereobserved for pure ZnSe thin film [16]. In their report, phase transformation from zincblende towurtzite structure with nitrogen-doping was rather elegantly elucidation by explicating theappearance of Raman peaks using the 1st principle calculations. However, Kalita et al.

performed some detailed structural parameter analysis on TVD ZnSe thin films where substrate temperaturewas varied from 30 to 350 °C during deposition. There, the (220) and (311) peak-intensities appearedto increase rather noticeably above 300 °C substrate temperature. Recently, Mittal et al. depositedZnSe thin film using thermal vapour deposition and magnetron sputtering techniques on Si, SiO_2-glass and Ge substrates, where the reported XRD pattern of the TVD ZnSe thin film on Si substrateshows the existence of all three peaks [10]. In their report, elaborate microstructural and surface morphological analyses were done for the structural characterization and the major emphasis was putparticularly on the wave-guide application of the ZnSe thin films. Generally XRD data of manynanoparticles, nanocomposites and thin films were used for structural characterization adopting notonly the simple Debye equation but also the modified Debye relation, modified Williamson-Hallrelation named as uniform stress density model (USDM), uniform deformation energy density model(UDEDM) and size-strain plot (SSP) [24–30]. In addition to that, Bushroa et al. used semi analyticalfunction to extract size, strain data for TiSiN thin film deposited by magnetron sputteringtechnique [31]. However, reports are yet to be published for ZnSe thin film adopting all theseaforementioned models.

Although in the recent years, a considerable amount of studies have been carried out either on the optical or structural properties of ZnSe thin films prepared under different conditions, a littleemphasis has been given on both the optical and structural properties together, which is vital forfilm-quality assurance and device applications. Thus, there is an ample of room for conductingelaborate studies that tends to bridge the two aspects of the concerned thin film. Therefore, theprimary objective of this paper is to study the TVD ZnSe thin film on a common soda-lime glasssubstrate through detailed structural analysis including crystallographic, geometrical andmicrostructural parameters using XRD, SEM and different deformation models. At the same time,various optical parameters have been analysed using the interference patterns present in the opticaltransmission spectra, so as to establish any meaningful correlation between the structural featuresand optical parameters of a single TVD ZnSe thin film on an ordinary substrate. The study will alsoacts as a catalyst to conduct further detailed research on the influence of process variables andchemical compositions on the properties chalcogenide based thin films.

2. Materials and Method

ZnSe thin film is prepared by thermal evaporation of ZnSe powder on a normal inexpensive soda-lime glass substrate which was at first, thoroughly cleaned ultrasonically in acetone bath for an hour followed by rinsing with de-ionized water numerous times. Then the substrate was left inside avacuum desiccator filled with moisture absorbing fresh silica-gel for 24 hrs to dry. Coarse ZnSeaggregates were crushed into fine powder which was then directly put in a molybdenum boat insidethe vacuum chamber of a thermal evaporator (model: EU300).The clean substrate was clamped directly on top of the boat together with a custom-designed tin-mask to control the deposition area.The evaporation process was carried out at a vacuum pressure of approximately 10^{-4} Pa. Thedeposition rate was controlled by adjusting the Variac manually. During the deposition process, thesubstrate was kept at 300 °C. The thickness and deposition rate were monitored by quartz crystaloscillator. The deposition rate was kept around 0.2 nm/sec. The deposited thin film was thenannealed at an elevated substrate temperature of 350 °C for 1 hour under the same vacuumatmosphere in order to ensure that no oxidation of the film could take place and at the same time thesource was allowed to cool down.

The crystal structure and the initial phase identification of the thin film was performed by PANalytical X-ray diffractometer (Model: EMPYREAN, PANalytical, Almelo, Netherland) adoptingBragg-Brentano geometry with parallel beam optics configuration. The diffractometer was operatedat 45 kV and 40 mA and the experiment was carried out at room temperature. For crystallographicorientation analysis, a special diffractometer optical configuration required by the Schulz reflectionmethod was adopted for the X-ray intensity-data collection and the commercial X'pert TEXTUREsoftware (Version 1.2, PANalytical B.V., Almelo, Netherlands) supplied by PANalytical was utilized to construct 3D pole-figures. thin film surface morphology and cross-section were observed by FieldEmmission Sanning Electron Microscope (FESEM) (model: JSM 7600F, JEOL, JAPAN).Transmission spectra of both ZnSe film deposited glass substrate and clean substrate without the filmwere collected within a wavelength range of 250–2500 nm with respect to air at room temperatureusing a dual beam UV-Vis-NIR spectrophotometer (model: LAMBDA 1050, Perkin-Elmer, USA)equipped with three detector module. The diffuse reflectance spectra of ZnSe source powder wasalso collected at room temperature by replacing the three detector module with 150 mm integratingsphere, where spectralon standard supplied by Perkin-Elmer was used as a reference sample.

3. Results and Discussion

3.1. Structural Characterization

Figure 1(a) shows the X-ray diffraction (XRD) spectra of ZnSe thin film. The most intense peak was identified for (111) plane at 2θ = 27.20°and the crystal strcuture was nicely matched with cubiczincblende structure (ICDD 01-071-5978). The other two peaks were observed at 2θ = 45.23°and53.15°correspond to (220) and (311) planes repectively. Although a similar preffered orientation hadalso been observed in a previous report [6] the observed relative intensity of (311) peak with respectto (220) peak appear to be different. At the same time, in Figure 1, the (311) to (220) peak intensity ratio appears to be greater and smaller than one for the film and the source powder respectively. Suchanomalies have been dealt-with through thin film texture analysis at the end of this section.Moreover, in contrast to our observation, the existence of purely hexagonal wurtzite structure or amixture of cubic zincblende and hexagonal wurtzite structures were also reported for ZnSe thin filmsdeposited by different methods indicating the influence of deposition technique on phaseformation [13,16]. The absence of any peak other than those for ZnSe in the diffraction pattern of ourthin film suggests that the applied vacuum during the deposition process was good enough to preventthe formation of any stable oxide like ZnO as reported to form earlier [32].

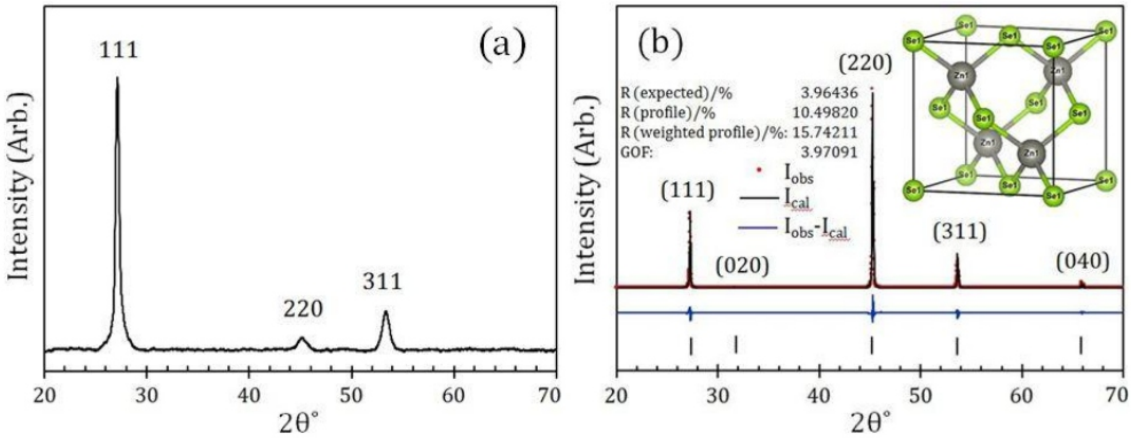

Figure 1. (a) X-ray diffraction spectra of ZnSe thin film; (b) Powder XRD pattern for ZnSe corresponds to red dot, black solid line refers to calculated (Rietveld fitting) andsky-blue solid line refers to the difference between observed and Rietveld fitting data.

However, it is worth mentioning that in a previous report by M. Ashraf et al. [20] where ZnSe thin films were thermally deposited on soda-lime glass substrate with 25 °C substrate temperature,(111) peak intensity gradually increased with increasing post-annealing temperature from 100 to300 °C, which was attributed a gradual increase in crystallinity of the thin films. In contrast to that,(220) and (311) peak intensities remained either quite low or nonexistent [13] irrespective of postannealing temperature. However, the XRD pattern of pulse laser deposited ZnSe thin film on fusedquartz substrate at 400 °C reported by Zhang et al. [16] exactly matches the peak intensity pattern asobserved in our case (Figure 1(a)), where the (111), (311) and (220) peak-intensities can be found tochange in a descending order. Additionally, the relative intensities of all the three peaks in both ofour studies appear to be rather noticeable. This observation is in fact rather promising in a sense thatit allowed us to perform crystallographic orientation analysis of the film with respect to all threeplanes observed (as shown at the end of this section), which has not yet been reported in anyscientific literature for the TVD ZnSe films to the best of our knowledge.

Figure 1(b) shows Rietveld analysis results obtained from X'Pert HighScore Plus (Version 4.1, PANalytical B.V., Almelo, Netherlands) software for ZnSe source powder, with various fittingparameters listed in the upper left corner of the figure. Both goodness of fit (GOF) and R-factorsappear to fall within acceptable range. The source powder has been found to have cubic symmetrywith F-43m space group. Since Rietveld refinement method cannot be used to estimate the latticeparameters from thin film XRD data due to poor signal to noise ratio, an alternative approach wasadopted to estimate the lattice parameter known as Nelson-Riley relation given in the equationbelow [33]:

$$f(\theta) = \frac{1}{2}\left[\frac{cos^2\theta}{sin\theta} + \frac{cos^2\theta}{\theta}\right] \tag{1}$$

Figure 2 shows the lattice parameter "a" as a function of Nelson-Riley error function $f(\theta)$, where "a" is given by the following equation for cubic system:

$$\mathrm{a} = \frac{\lambda\sqrt{h^2+k^2+l^2}}{2sin\theta} \tag{2}$$

The least square fitted line equation is given at the bottom right corner of the figure. The accurate lattice parameter of the thin film corresponds to the value of at which x (= f (θ) =0. Asimilar approach was adopted to calculate the ZnSe thin film lattice parameter by Kalita et al. [4].The corrected lattice parameter estimated from Figure 2 is, = 5.683 Å shows good agreement withpreviously reported result [4].

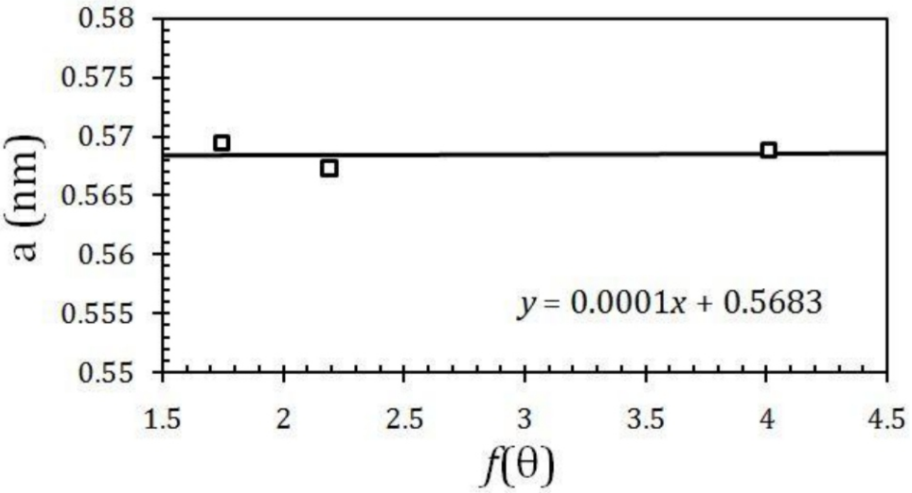

Figure 2. Nelson-Riley error function (*f*(θ)) relation to estmate the lattice parameter of ZnSe thin film.

Lattice parameter of ZnSe powder estimated using Rietveld refinement method exhibites smaller value than what we have obtained from Nelson-Riley relation. The powder diffractionpattern and the corresponding Rietveld refinement are shown in Figure 1(b) along with the ZnSe unitcell in inset. The structural parameters obtained from Rietveld refinement confirms F-43m spacegroup with cubic zincblende symmetry for ZnSe powder, where the Se atoms reside in all the face centered cubic positions and the Zn atoms occupy one-half of the tetrahedral sites in an alternating manner axially. The lattice parameters for powder and thin film are given in Table 1 below.

Table 1. Lalttice parameters ZnSe source powder and thin film.

Lattice constant	Rietveld refinement (source powder)	Nelson-Riley method (ZnSe thin film)	Lattice volume strain
a (Å)	5.663	5.683	0.0106

Thus it is also possible to estimate the lattice volume strain given in the 4th column of Table 1using the following equation:

$$\frac{\Delta V}{V} = \frac{(a+\Delta a)(b+\Delta b)(c+\Delta c)-abc}{abc} \tag{3}$$

where, *a*, *b* and *c* are the dimensions of the unit cell and *Δa*, *Δb* and *Δc* are the changes in lattice dimensions. Now, equation (3) can be written as:

$$\frac{\Delta V}{V} = (1+\varepsilon_1)(1+\varepsilon_2)(1+\varepsilon_3) - 1 \tag{4}$$

where, $\varepsilon_1 = \Delta a/a$, $\varepsilon_2 = \Delta b/b$, $\varepsilon_3 = \Delta c/c$. When, $\varepsilon_{1,2,3} \ll 1$, then equation (4) can be approximated as:

$$\frac{\Delta V}{V} \approx 3\varepsilon \tag{6}$$

Assuming isotropic strain in the cubic lattice we get: $\varepsilon_1 = \varepsilon_2 = \varepsilon_3 = \varepsilon$. Hence, equation (5) can be simplified to:

$$\frac{\Delta V}{V} \approx 3\varepsilon \tag{6}$$

where, $\varepsilon = \frac{a_{thinfilm} - a_{sourcepowder}}{a_{sourcepowder}}$.

The XRD data can also be used to estimate the crystallite size and the average strain generated in the thin film. XRD profile is a convolution of instrumental line broadening and physical orstructural broadening. The structural line broadening is in turn is associated with size broadening and strain broadening.

Now, assuming Lorentzian XRD line profile we can write,

$$\beta_T = \beta_{struct.} + \beta_{inst.} \tag{7}$$

$$\beta_{struct.} = \beta_{cryst.} + \beta_{str.} \tag{8}$$

$$\beta_T = \beta_{cryst.} + \beta_{str.} + \beta_{inst.} \tag{9}$$

where, β_T , $\beta_{struct.}$, $\beta_{cryst.}$, $\beta_{str.}$ and $\beta_{inst.}$ are spectral width (FWHM) of the observed peak, structural line broadening, size broadening, strain broadening, and instrumental line broadening respectively. Here, $\beta_{inst.}$ is obtained from NIST (National Institute of Science and Tech) standard sample: Lanthanum hexaboride (LaB_6). Therefore, $\beta_{struct.}$ can be extracted from β_T using equation (7). The most well-known relation between crystalline size and line broadening is the Debye-Scherrer relation which is given by (12):

$$\beta = \frac{k\lambda}{D\cos\theta} = \frac{k\lambda}{D}\frac{1}{\cos\theta} \tag{10}$$

where, *D* is the crystallite size, β is equivalent to FWHM for structural broadening ($\beta_{struct.}$) obtained from equation (7) for low index and high intensity peak, k is approximated as 0.9 and λ = 1.54 Å is X-ray wavelength. Therefore, *D* estimated from (111) peak in Figure 1(a) in the present case comes out to be 13.3 nm.

In principle, the crystallite size should be independent of $\beta\cos\theta$ in the equation (10). However, experimentally $\beta\cos\theta$ can be found to vary as 0.010, 0.013, 0.012 for (111), (220) and (311) planes, respectively. It means that for each reflection plane, the crystallite size varies according to equation (10), which cannot be true. Therefore, an error is introduced in the crystallite size estimation. To minimise the error, equation (10) can be modified as follows [28]:

$$\ln\beta = \ln\frac{k\lambda}{D} + \ln\frac{1}{\cos\theta} \tag{11}$$

A plot of $\ln\beta$ against $\ln(1/\cos\theta)$ along with the corresponding least square fitted equation is depicted in Figure 3(a). In principle, if there is no systematic error that is, if equation (10) holds for experimental data, the slope of the fitted line should be 1. However, in case of present experimental data the slope has been found to be greater than 1 (~3.4) due to a more pronounced θ dependence of $\beta\cos\theta$ than that required for maintaining a fixed *D* value.

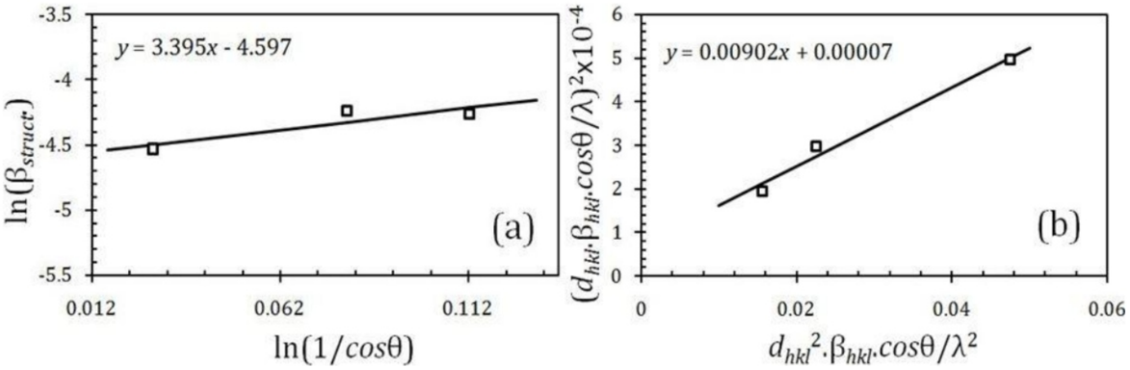

Figure 3. (a) Modified Debye-Scherrer model, (b) SSP method, along with the corresponding equations required for linear fit.

Now following equation (11), at $\ln(1/\cos\theta) = 0$, the Y -axis intercept can be related to the size of the crystallite as follows:

$$\ln\beta = \ln\frac{k\lambda}{D} = -4.597$$

$$\text{or, } D = \frac{k\lambda}{e^{\ln\beta}} \tag{12}$$

The crystallite size estimated from equation (12) is 13.7 nm. However, lattice strain cannot be calculated from the modified Debye-Scherrer relation. The size and strain have been estimated usingSize-strain plot (SSP). In this estimation, the peak profiles due to strain were assumed to be Gaussianand crystallite size as Lorentzian. The SSP relation is expressed as [30]:

$$(d_{hkl}\beta_{hkl}cos\theta/\lambda)^2 = \frac{k}{D}(d_{hkl}^2\beta_{hkl}cos\theta/\lambda^2) + \left(\frac{\varepsilon}{2}\right)^2 \tag{13}$$

where,d_{hkl} is the interplanner spacing calculated using the standard Bragg's law, β_{hkl} is the FWHM for structural broadening, k is approximated to 3/4 for spherical shape, ε is the average strain, θ is the Bragg angle and D is the crystal size. The standard plot for SSP model is shown in the Figure 3(b).Here, the crystallite size has been estimated as 12.8 nm and the strain in the film has been determinedto be $1.70 \times 10^{-2}$from the slope and Y-intercept of the least square fitted solid line given by theequation at the top left corner of the figure, respectively.

The size and strain have further been estimated adopting the basic Williamson-Hall (W-H) relation [15], which can be directly derived by combining the basic Scherrer formula (equation (10), where,$\beta = \beta_{cryst.}$), the equation for strain broadening given by: $\beta_{srt.} = 4\varepsilon \cdot \tan\theta$ and the relation for structural broadening (equation (8)) as below:

$$\beta_{struct.} = \beta_{cryst.} + \beta_{str.} = \frac{k\lambda}{Dcos\theta} + 4\varepsilon \cdot \tan\theta \tag{14}$$

The above equation can simply be rearranged as:

$$\beta_{hkl}cos\theta = \frac{k\lambda}{D} + 4\varepsilon\, sin\theta \tag{15}$$

Here, $\beta_{hkl}(\equiv \beta_{struct.})$ is the FWHM for structural broadening, *D* s the size of the crystal, ε is the strain, λ is the X-ray wavelength and is a constant approximated to 0.9. This equation is also known as the uniform deformation model (UDM) and it is assumed that the strain is uniform in all crystallographic directions.

Figure 4(a) depicts the plot of $\beta_{hkl}cos\theta$ vs. $4sin\theta$ along with the least square fitted linear equation in the inset. The slope of the fitted equation corresponds to strain and the Y-intercept corresponds to the size of the crystallite as λ and are already known. The basic W-H relation (UDM) can be modified using the Hooke's law with the assumption of uniform stress (σ) and theanisotropic strain ε_{hkl} as follows:

$$\varepsilon_{hkl} = \frac{\sigma}{E_{hkl}} \tag{16}$$

The modified model is known as the uniform stress deformation model (USDM). The analytical function for the USDM can be expressed by replacing ε with ε_{hkl} in equation (15) and then equating

$$\beta_{hkl}cos\theta = \frac{k\lambda}{D} + 4\varepsilon_{hkl}\, sin\theta = \frac{k\lambda}{D} + 4\frac{\sigma}{E_{hkl}}\, sin\theta \tag{17}$$

However, for cubic systems, the elastic modulus E_{hkl} is related to elastic compliance S_{11}, S_{12}, S_{44} and *hkl* index of the corresponding plane by the following relation:

$$\frac{1}{E_{hkl}} = \frac{S_{11}-2(S_{11}-S_{12}-S_{44})\left(h^2k^2+k^2l^2+l^2h^2\right)}{\left(h^2+k^2+l^2\right)^2} \tag{18}$$

Here, the elastic compliances are calculated from elastic stiffness (C_{mn}) values using the following relations:

$$S_{11} = \frac{C_{11}+C_{12}}{(C_{11}-C_{12})(C_{11}+2C_{12})};\ S_{12} = \frac{-C_{12}}{(C_{11}-C_{12})(C_{11}+2C_{12})};\ S_{44} = \frac{1}{C_{44}} \tag{19}$$

where C_{11}, C_{12} and C_{14} are 80.7, 48.8 and 44.1 GPa, respectively. In Figure 4(b), $\beta_{hkl}cos\theta$ is plotted against $(4/E_{hkl})\ sin\theta$. The slope of the plot after least square fitting the data with linear equation given in the inset corresponds to the stress, which is 103.17 MPa and the Y-intercept of the fitted line is related to the size of the crystal which is estimated as 13.7 nm. The W-H relation can be further modified to calculate the isotropic deformation energy density of a crystal by assuming both thestress and strain to be anisotropic according to:

$$u = \frac{1}{2}\varepsilon_{hkl}\sigma_{hkl} = \left(\frac{{\varepsilon_{hkl}}^2 E_{hkl}}{2}\right) \tag{20}$$

This model is known as uniform deformation energy density model (UDEDM) and can be expressed by combining equations (17) and (20) as:

$$\beta_{hkl}cos\theta = \frac{k\lambda}{D} + 4\varepsilon_{hkl}\, sin\theta = \frac{k\lambda}{D} + 4\left(\frac{2u}{E_{hkl}}\right)^{\frac{1}{2}} sin\theta \tag{21}$$

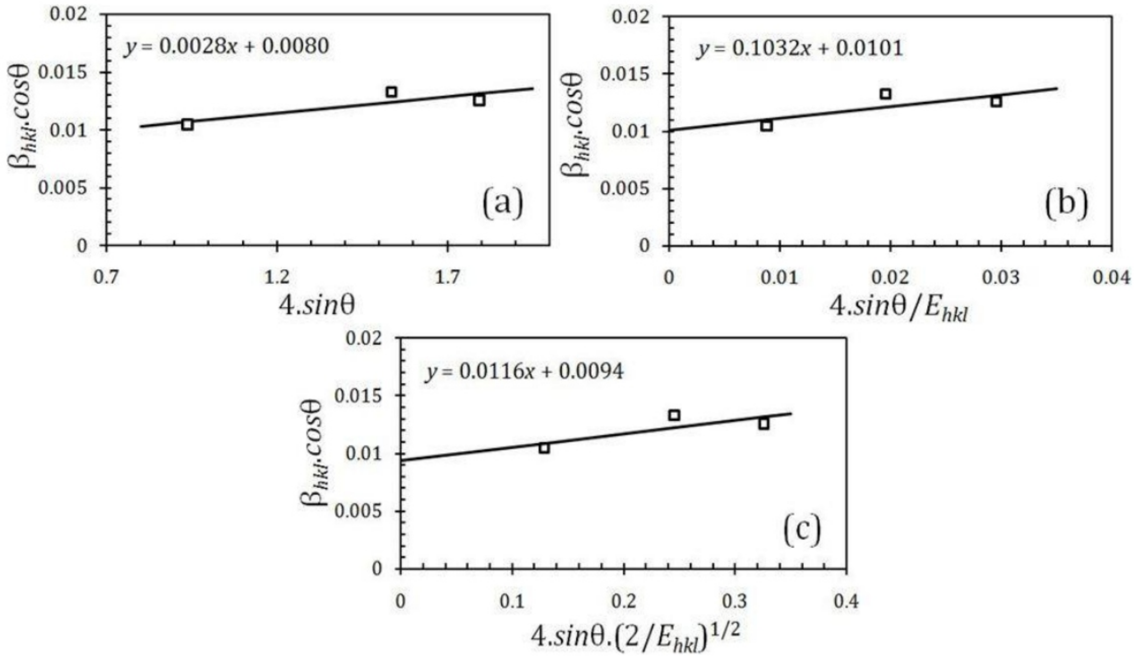

Figure 4. (a) Basic W-H model: UDM, (b) modified W-H model: USDM, (c) modified W-H model: UDEDM for ZnSe thin film along with correspond equations required for the linear fits.

In Figure 4(c), $\beta_{hkl}cos\theta$ is plotted as a function of $4(2u/E_{hkl})^{\frac{1}{2}} \cdot sin\theta$. The slope of the line after least square fitting the data, represented by the linear equation in the inset determines the deformation energy density of the crystal and it is estimated as 134.53 kJ/m^3. The size of thecrystallite has been estimated as 14.8 nm from the Y-intercept of the fitted line. The dislocationdensity has also been calculated using the relation:

$$\rho = \frac{1}{D^2} \tag{22}$$

However, according to a recently proposed approximation method [31], the experimental XRD peak profile width is a convolution of size and strain broadening. Here the size and strain broadeningprofile was approximated using two analytical functions $M(x)$ and $N(x)$, given by [31]:

$$M(x) = (1 + \gamma x^2)^{-1} \tag{23}$$

$$N(x) = (1 + \gamma x^2)^{-2} \tag{24}$$

where γ is a constant coefficient.

Here, the structural broadening was calculated by subtracting the instrumental broadening from the total broadening at different Bragg angles. For structural characterization two peaks wereselected: (111) and (311) at 2θ = 27.13°and 53.32°respectively. For these two observed peaks theexperimental structural line broadening β_1 and β_2 were estimated in tems of FWHM. Now following some manipulations of equations (23) and (24) it was shown [31]:

$$\frac{m_1}{\beta_1} = \frac{1}{2}\left[1 - 4\frac{n_1}{\beta_1} + \sqrt{1 + 8\left(\frac{n_1}{\beta_1}\right)}\right] \tag{25}$$

$$\frac{\beta_2}{\beta_1} = \frac{\left\{\left[V\left(\frac{m_1}{\beta_1}\right)\right]+\left[2\left(\frac{n_1}{\beta_1}\right)W\right]\right\}^2}{\left[V\left(\frac{m_1}{\beta_1}\right)\right]+\left[4\left(\frac{n_1}{\beta_1}\right)W\right]} \tag{26}$$

$$\frac{n_2}{\beta_2} = \frac{n_1}{\beta_1} \times \frac{W}{\beta_2/\beta_1} \tag{27}$$

where, $m_1$and m_2 are the size broadening contributions to (111) and (311) peaks respectively and n_1 and n_2 are the strain broadening contributions to (111) and (311) peaks, respectively.Here, V and W are expressed as [31]:

$$V = \frac{m_2}{m_1} = \frac{Cos\theta_{111}}{Cos\theta_{311}} \tag{28}$$

$$W = \frac{n_2}{n_1} = \frac{tan\theta_{311}}{tan\theta_{111}} \tag{29}$$

Now, Figure 5 shows m_1/β_1 as a function of β_2/β_1calculated using equations (25) and (26). From this plot experimental m_1/β_1 can be extracted from the corresponding experimental β_2/β_1 ratio as shown by the dotted line intersecting the left-hand-side vertical axis. Since m_1 is the size broadening contribution to experimental β_1, the crystal size could be calculated using Scherrer formula given as:

$$D = \frac{k\lambda}{m_1 cos\theta_{111}} \tag{30}$$

Here, m_1 = (experimental m_1/β_1 ratio) x β1, D is the size of the crystal, k is a constant equal to 0.9, λ is the wavelength of the X-ray radiation and θ111 is the Bragg angle for (111) peak. Following equation (30), the crystal size can found to be 15.4 nm.

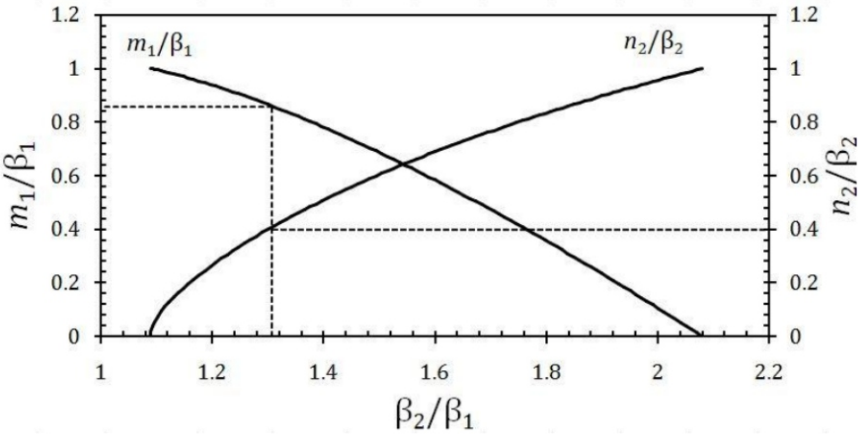

Figure 5. m_1/β_1 and $n_2/\beta_1$was plotted as a function of β_2/β_1.

Figure 5 also shows n_2/β_2 as a function of β_2/β_1 calculated using equations (26) and (27), where, the experimental n_2/β_2 can also be extracted from the corresponding experimental β_2/β_1 ratio as shown by the dotted line intersecting the right-hand-side vertical axis. Since n_2 is the strain broadening contribution to experimental β_2, the strain could be calculated using the following formula given as:

$$\varepsilon = \frac{n_2}{4tan\theta_{311}} \tag{31}$$

Here, n_2 = (experimental n_2/β_2 ratio) × β_2 , ε is the strain and θ_{311} is the Bragg angle for (311) peak. Following equation (31), the strain has been estimated to be 5.90×10^{-3}. Figure 6(a) shows scanning electron microscopic (SEM) image of the ZnSe thin film surface and the corresponding particle size distribution determined from several such micrographs using the ImageJ software (Version 1.46r) is also given in Figure 6(b).

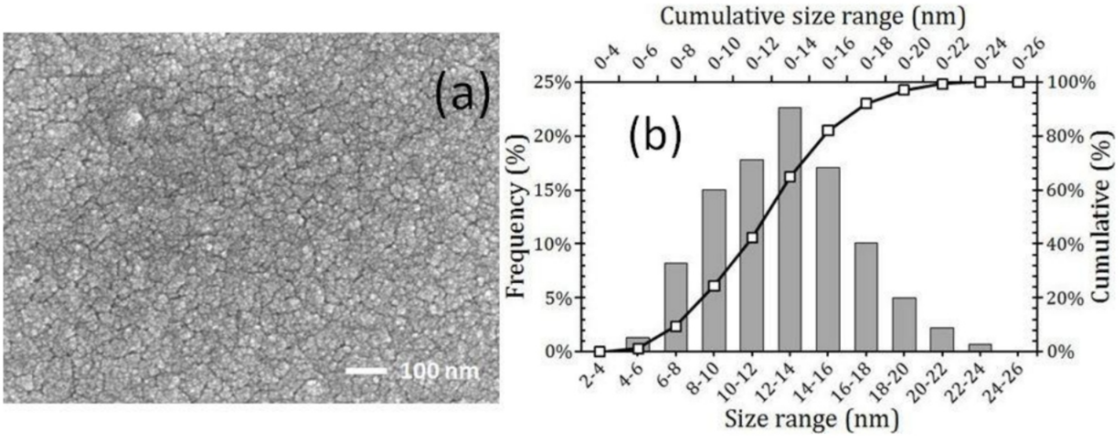

Figure 6. (a) ZnSe thin film SEM micrograph with 100 nm scale bar, (b) particle size distribution estimated from the SEM micrograph.

The most probable particle size can be found to be around 12–14 nm from the size distribution histogram. Table 2 shows the detailed structural and geometrical parameters obtained from the XRDdata analysis using different models and SEM.

Table 2. List of microstructural and geometrical parameters.

Method	D (nm)	ε	σ (MPa)	u (kJ m^{-3})	ρ (nm^{-2})	R^2
Debye-Scherrer	13.3				5.68×10^{-3}	
Modified Debye-Scherrer	13.7				5.29×10^{-3}	0.80
SSP	12.8	1.70×10^{-2}			6.09×10^{-3}	0.98
UDM	17.2	2.84×10^{-3}			3.36×10^{-3}	0.73
USDM	13.7	$*1.33 \times 10^{-3}$	103.17		5.29×10^{-3}	0.54

UDEDM	14.8	*1.85×10^{-3}	*147.29	134.53	4.57×10^{-3}	0.62
Approximation technique	15.4	5.90×10^{-3}			4.18×10^{-3}	
SEM	12–14				$(5.1–6.22)\times10^{-3}$	

* Average value calculated from three different crystallographic directions: (111), (220) and (311).

It is worth mentioning that a step-size of 0.05°has been used for the thin film XRD line scanning which is less than 1/10 of the observed FWHM (β_T) of the sharpest peak in Figure 1(a).This configuration gives us more than 10 data points for determining β_T with reasonable accuracy. In addition to that, the correlation coefficients (R^2) for least square fitting the structural broadening data with different models (Figures 3(a), 3(b) and 4(a–c)) appear to fall within the range 0.60–0.98, whichis quite reasonable when compared with previously published data for CsI thin film [27].

It can be found that the results obtained from the XRD analysis show reasonable agreement with SEM. From the SEM image analysis (Figures 6) a range of particle size varying from 2 to26 nm has been observed. It can also be found that around 80% of the particles have size within therange of 10 to 18 nm (Figure 6(b)) which is quite agreeable as far as the XRD data is concernedwhere the average crystal size has been found to fluctuate within a narrow range of 12 to 17 nmdepending on the models adopted for size calculation. However, any marked difference betweencrystal/particle size range measured by XRD and micrographic analysis could be associated withformation of defects in a certain manner that gives rise to different crystallographic orientations inindividual particles. This is particularly true in case the particle size obtained from electronmicroscopy is reasonably larger than the crystal size of the same sample obtained from XRD peakbroadening effect since; the X-ray diffraction peaks under Bragg-Brentano configuration arise fromcoherently scattering domains with congruent orientations, parallel to the diffraction plane. Whenindividual particles form by agglomeration of such coherent domains separated by interfaces eitherwith sharp orientation contrast ideally represented by grain boundaries or small orientation mismatch(low angle interface) typically represented by a 2D region consisting of regularly spaced dislocations,the crystal size from XRD always comes out to be smaller than the particle size from micrograph.Although with SEM the high-angle boundaries are sometimes easily identifiable from surfacemorphology it is rather unlikely to locate any low angle interface. Hence, as in case of the presentthin film sample the particle size range agrees with crystal size range, it can be assumed that the individual particles in the SEM image are in general coherent in terms of crystallographic orientation.Therefore the dislocation densities calculated from equation (22) as tabulated in the 3rd column ofTable 2 represents the dislocation population along the high angle grain boundaries with somedislocations distributed possibly in a random manner within the coherent crystals without forming any low angle interface.

The SEM micrograph in Figure 6(a) further reveals the existence of numerous micro-cracks brunching throughout film surface. Such formations could be associated with strain relaxationphenomenon. From the lattice parameter data listed in Table 1, it can be found that lattice parameterof the thin film is slightly larger than that of the strain-free source powder by 0.023 Å. This corresponds to a lattice volume strain of 1.06×10^{-2} in the thin film as estimated using equation (6).This volume-change of the unit cell of the crystal can be attributed to the local lattice strain. On theother hand the average thin film strain has been estimated as 1.70×10^{-2}, 5.90×10^{-3}, 2.84×10^{-3},$1.33\times10^{-3}$and 1.85×10^{-3}using SSP, Approximation method, UDM, USDM and UDEDM respectively. Except for average internal strain estimated from SSP, the average internal strain valuesobtained from the other models are at least 47% less than the local lattice volume strain. This implies that the thin film could become relaxed by reducing its strain through formation of surface micro cracks during cooling after deposition. Therefore, under the above circumstances, it can be presumedthat the average film strains obtained from either the basic and modified W-H models or theapproximation method are more self-explanatory compared to that obtained from SSP method in ourcase. However, a more detailed study is required to reach to any definite or decisive conclusion onthe above issue, which is underway. Nevertheless, it can safely be said that estimated crystallite size,strain and dislocation density show good agreement with previously reported data [4].

For further crystallographic characterization, it is important to find out the orientation distribution of the diffracting planes/crystallites with respect to substrate-normal. The orientationdistribution of any particular crystallographic plane can be determined by constructing pole-figure,which is regarded as an essential visual tool for examining the texture of crystalline samples. In caseof thin films, pole-figure is also used to check the quality of the surface in terms of the preferredcrystallite orientation. For collecting the diffracted beam intensity data corresponding to a certainplane, the film was subjected to an in-plane rotation (represented by Φ-angle) from 0 to 360°at 3°interval at any given sample-surface tilt (represented by χ-angle) and the χ-angle was varied from 0 to 75°at same interval as Φ-angle. Then the intensity profile was further modelled up to a χ-angle of90°to construct complete 3D pole-figures and the standard commercial X'pert TEXTURE softwarewas used for that purpose. Three planes: (111), (220) and (311) were originally identified (Figure1(a)) in the TVD ZnSe thin film XRD pattern under Bragg-Brentano configuration represented by 0°χ-angle and pole-figures corresponding to all three crystallographic planes were constructed asshown in Figure 7. The spherically anisotropic shape of the 3D pole-figures clearly indicates theexistence of some sort of texture in our thin film sample. From the (111) pole-figure, it can be foundthat a major share of (111) plane is oriented at around 15°and 60°angles with the substrate planenormal. Contrary to that, the most intense peak has been observed for (111) plane in Figure 1(a).Such apparent discrepancy can be explained by the fact that even though the intensity count of (111)pole-figure at $\chi = 0°$is lower than that at $\chi = 15°$or 60°irrespective of Φ-angle it's absolute value israther high compared to its (220) and (311) counterparts at 0°χ-angle, at least numerically. Inaddition to that, by comparing the XRD patterns of the ZnSe thin film (Figure 1(a)) and the sourcepowder (Figure 1(b)), it can also be found that the (311) peak intensity in the film is quite significant relative to that of the (220) peak, whereas the trend is exactly the opposite in the source powder.Such anomalous variation in relative peak intensity could be attributed to a distinctively sharp rise inintensity count observed in (311) pole-figure compared to that in (220) pole-figure around 0°χ-anglerepresenting the Bragg-Brentano geometrical configuration used for collecting the XRD patterns in Figure 1.

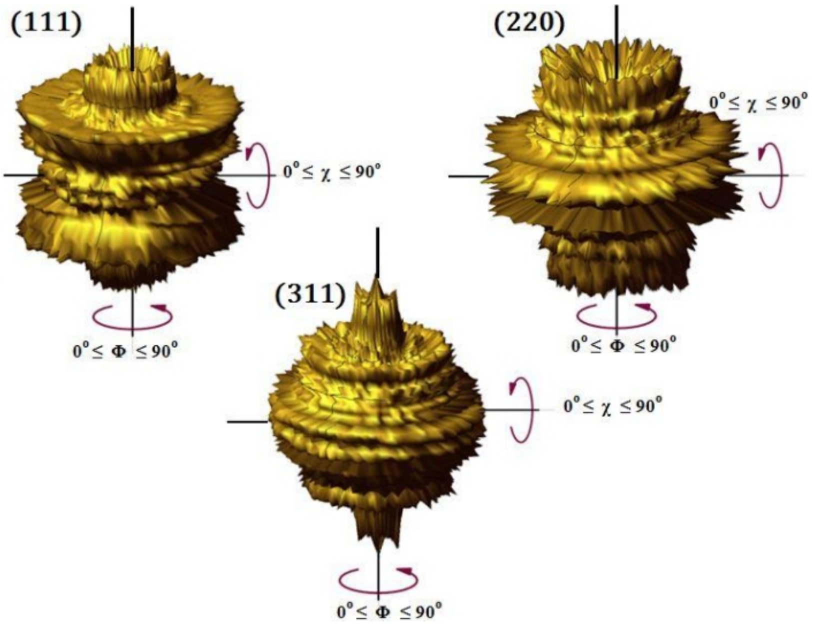

Figure7. Three dimensional pole-figure of ZnSe thin film.

However, to our knowledge, this is for the first time to report the orientation distributions of the three different planes so far. Previously, different groups have published pole-figure data for ZnSethin films [34,35,36] but only for (111) plane, since it exhibited the most intense and legible peakunder Bragg-Brentano configuration, which is consistent with our XRD data as well.

3.2. Optical Properties of ZnSe Thin Film

Figure 8(a) shows the transmittance spectra of ZnSe thin film. Two regions are found in the transmittance spectra. Region-I extending from 600 to 2500 nm, corresponds to transparent regionsince the incident wave passes through the thin film sample without being absorbed. The energy of the photon corresponding to these wavelengths is smaller than the band gap energy of ZnSe thin film.In this region a wavy nature in the spectra is observed. This is called the interference fringe or FECO(Fringes of Equally Chromatic Order). These interference pattern-like fringes are produced due toback and forth bouncing of the incident wave between three interfaces: film–air, film–substrate andsubstrate–air. In Region-II below 600 nm the transmittance drops sharply due to absorption ofincident photon. The optical band gap can be estimated from this region.

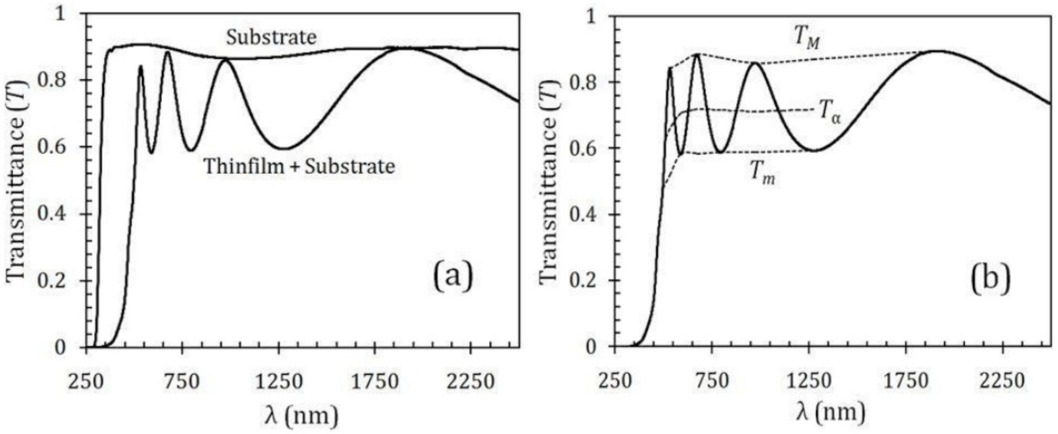

Figure 8. (a) Transmittance of ZnSe thin film deposited on soda-lime glass substrate, (b) Swanepoel's envelopes T_M and T_m; T_α refers to the geometric mean of T_M and T_m.

Figure 8(b) shows the three envelopes T_M, T_m and T_α in the transmittance spectra where $T_\alpha = \sqrt{T_M \cdot T_m}$. Since the FECO fringes give maxima and minima in transmittance spectra, the T_M and T_m corresponding to the top and bottom envelopes are obtained by interpolating the interference maxima and minima of the FECO fringes respectively using spline interpolation technique. Using Swanepoel's envelope method (SWEM), the refractive index of the thin film was estimated [37]. The refractive index has been calculated using the following equation [38]:

$$n_1^2 = \left[N(\lambda) + \{N(\lambda)^2 - S(\lambda)^2\}^{\frac{1}{2}}\right] \tag{32}$$

where, n_1 is the 1st approximation of the thin film refractive index and the parameter $N(\lambda)$ is expressed as follows;

$$N(\lambda) = 2S(\lambda) \cdot \left(\frac{T_M - T_m}{T_M T_m}\right) + \left\{\frac{S(\lambda)^2 + 1}{2}\right\} \tag{33}$$

where, $S(\lambda)$ is the substrate refractive index and can be expressed as:

$$S(\lambda) = \frac{1}{T_S} + \left(\frac{1}{T_S^2} - 1\right)^{\frac{1}{2}} \tag{34}$$

Here, T_S is the substrate transmittance which is a function of wavelength as shown in Figure 8(a). Knowing the n_1 value, a rough estimation of the thin film thickness (d_1) has been obtained using the following equation:

$$d_1 = \frac{\lambda_1 \lambda_2}{2[n_1(\lambda_2).\lambda_1 - n_1(\lambda_1).\lambda_2]} \tag{35}$$

where, λ_1 and λ_2 are the two wavelengths corresponding to two adjacent maxima (or minima) and $n_1(\lambda_1)$ and $n_1(\lambda_2)$ are the two corresponding refractive index values estimated from equations (32–34). Using the average value of d_1 and calculated n_1 it is possible to calculate the FECO order number m_o from basic interference equation given below:

$$2nd = m_o \lambda \tag{36}$$

T_M, T_m, n_1, d_1 and m_o at corresponding wavelength are listed in Table 3. Here, the thickness d_1 estimated using equation (35) shows strong wavelength dependence. The average d_1 is estimated to be 428.16 ± 56.17 nm. However, this fluctuation in thickness value can greatly be reduced by amending the calculated FECO order m_o values to the nearest exact integer for interference maxima and half integer for interference minima and then by using the revised FECO order M along with n_1 values in equation (36). The refined thickness values are now represented as d_2. Finally, a set of more refined refractive index (n_2) has been obtained by using corrected FECO order M and the average refined thickness in equation (36). The values of M, d_2 and n_2 are listed in Table 3. The average refined thickness ($d_{2(\text{avg})}$) of the thin film is estimated as 374.94 ± 16.47 nm. Nonetheless, the film thickness measured from cross-sectional SEM image shown in Figure 9 can be found to be 368.26 ±19.12 nm which is in good agreement with the thickness value obtained by optical method.

Table 3. Optical constants of ZnSe thin film using SWEM model.

λ	T_S	T_M	T_m	n_1	d_1	$d_{1(\text{avg})}$	m_0	M	d_2	$d_{2(\text{avg})}$	n_2
496	0.90		0.47								
532	0.90	0.84	0.51	2.78			4.49	4	381.43		2.83
588	0.90	0.85	0.58	2.56	379.27		3.74	3.5	400.39		2.74
672	0.89	0.88	0.58	2.63	504.35	428.16	3.36	3	382.16	374.94	2.68
793	0.87	0.87	0.58	2.67	435.72		2.89	2.5	369.89		2.64
972	0.86	0.85	0.58	2.69	393.31		2.37	2	360.03		2.59
1275	0.86	0.87	0.59	2.68			1.80	1.5	355.77		2.55
1912	0.89	0.89									

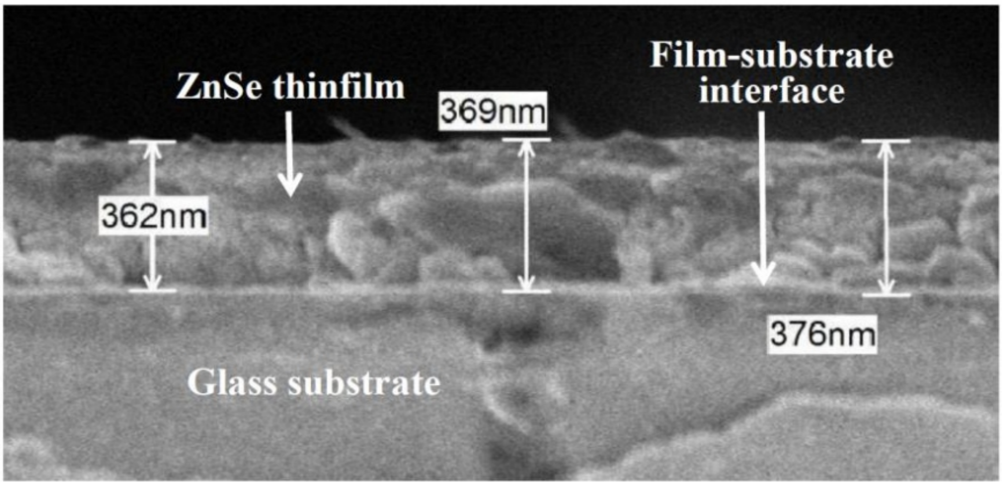

Figure 9. The SEM cross-sectional image of ZnSe thin film deposited on glass substrate.

Figure 10(a) shows the refractive index as a function of wavelength. The dispersion of refractive index follows the Cauchy dispersion relation with two fitting parameters: $a = 2.49$ and $b = 93714.88$ given by equation below [38,39]:

$$n(\lambda) = a + \frac{b}{\lambda^2} \tag{37}$$

Since the refractive index data fitted well with Cauchy dispersion relation, it is possible to estimate refractive index data in wide wavelength region.

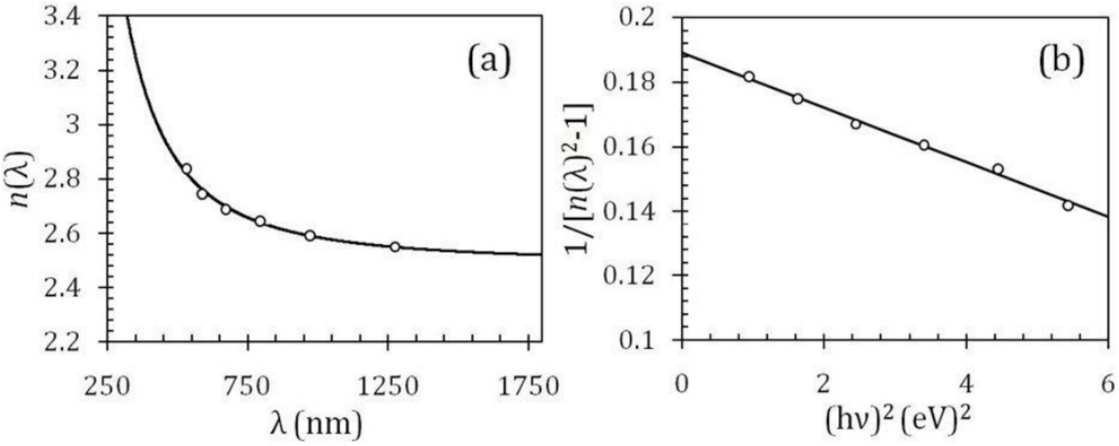

Figure 10. (a) Empty circles correspond to refractive index estimated from SWEM; solid line corresponds to Cauchy dispersion relation, (b) empty circles correspond to refractive index estimated from SWEM; solid line corresponds to WDD single oscillator model.

Although the Cauchy dispersion relation successfully represents the experimental dispersion of refractive index data, it does not give much physical information. Therefore, Wemple-DeDomenico(WDD) single oscillator model has been adopted to explain the dispersion of the refractiveindex [35,36]. It can be approximated that inter-band transitions are contributed by individualoscillator and each valence band electron is an oscillator. Generally, in the transparent region the realpart of the dielectric constant can be expressed as a summation of all possible inter-band oscillatorstrength in the Brillouin zone of crystalline materials. Wemple and DeDomenico suggested that ifone such oscillator's strength is stronger than the summation of that of the other oscillators, thenbelow the band gap (in the transparent region) the real part of refractive index can be expressedas [40]:

$$\varepsilon_1 - 1 = n(\lambda)^2 - 1 = \frac{E_d E_o}{\left[E_o^2 - (\mathrm{h}\nu)^2\right]} \tag{38}$$

where, E_d, E_o and hν are the dispersion energy, oscillator energy and incident photon energy respectively. Figure 10(b) shows refractive index data as a function of the incident photon energy, where the refractive index data has been plotted in $[n(\lambda)^2 - 1]^{-1}$ form. The first equality sign appeared in equation (38) originated from the fact that in the low energy region below the absorption edge with negligible absorption, the real part of the dielectric constant can be expressed as: $\varepsilon_1 = n(\lambda)^2 - k(\lambda)^2 \sim n(\lambda)^2$. Figure 10(b) shows a least square fitted straight line with a correlation coefficient $R^2 = 0.998$. The slope (m) of the fitted line is equal to the reciprocal of the product of E_d and E_o and the Y-intercept (C) corresponds to E_o/E_d. Using the slope and the intercept, the dispersion and the oscillator energies have been estimated using equations; $E_d = \sqrt{m/C}$ and $E_o = \sqrt{m \cdot C}$ respectively. The oscillator energy is related to the band gap and the dispersion energy is related to the dielectric loss. Most importantly, E_d and E_o can be related to the moments of the optical spectra given by the following relations [41]:

$$E_o^2 = \frac{M_2}{M_3};\ E_d^2 = \frac{M_2^3}{M_3} \tag{39}$$

Equation (39) relates the real and imaginary parts of the dielectric constants. M_2 and M_3 are the 2nd and 3rd moments of the optical spectra $\varepsilon_2(E)$ given by equation; $M_r = \int_{E_g}^{\infty} E^{3-2r}\varepsilon_2(E)dE$, where $\varepsilon_2(E)$ is also the representative of the imaginary part of dielectric constant [21]. On the other hand, E_d, E_o along with the real part of the dielectric constant $\varepsilon_1(E)$ can be estimated from $n(\lambda)$ data below the optical absorption edge using equation (38). However, a relation between $\varepsilon_1(E)$ and $\varepsilon_2(E)$ can also be established directly from Kramers-Kronig relation which is beyond the scope of this paper. However, the values of M_2 and M_2 can be determined simply by rearranging equation (39) as: $M_2 = E_d/E_o$ and $M_3 = E_d/E_o^3$.

E_o, E_d, M_2, M_3 for our ZnSe thin film are given in Table 4. M_2 is a measure of spectral width of the absorption spectra which is estimated as 5.28 and it is found to be smaller than the previously reported data [6]. It means that the variance around the optical band gap is smaller in our case. This could be attributed to the better crystallinity and good surface morphology associated with the reduced defect states in the forbidden zone. This assumption is further supported by smaller dispersion energy of 24.95 eV obtained in the present study, compared to that of 30.88 eV obtained in the previous study for ZnSe thin film under extreme laser annealing condition [6]. Since dispersion energy E_d increases with dielectric loss, the lower the E_d the better the crystallinity in terms of surface morphology and defect-states.

The E_d value obtained from WDD model has been used to estimate the inter-atomic bond characteristic using the following equation [27]:

$$E_d = \beta_o N_C Z_a N_e \text{ (e}V\text{)} \tag{40}$$

Here, N_e is the number of effective valence electrons per anion, N_C is the number of the nearest neighbouring anion for a cation, which is 4 for ZnSe since each Zn ion is situated in a tetrahedral site formed by Se ion (see inset of Figure 1(b)) and Z_a = 2 is the chemical valency of Se anion.

Therefore, N_e can be calculated using the following relation:

$$N_e = \frac{A_{Se}\times V_{Se}+A_{Zn}\times V_{Zn}}{A_{Se}} \tag{41}$$

Here, A_{Se} and A_{Zn} are atom% of Se and Zn respectively in the ZnSe; A_{Se} and A_{Zn} are 59.85 and 41.15 respectively experimentally obtained from SEM-EDX analysis; $V_{Se} = 6$ and $V_{Zn} = 2$ are the valence electron numbers of Se and Zn respectively. Thus, following equation (40),β_o has been evaluated as 0.42, suggesting the nature of the chemical bonds in ZnSe to be covalent. Our β_o value also shows excellent agreement with the classic paper of Wemple et al. [25], where the β_o has been calculated for the bulk material. However, our result shows larger value for β_o than recently reported result for ZnSe thin film [6]. This could possibly be attributed to a better bond ordering in the presentsample due to the high temperature deposition and post deposition annealing. From the WDD relation it is possible to estimate the static dielectric constant in very long wavelength region by replacing h$\nu\rightarrow 0$ (which is equivalent to $\lambda \rightarrow\infty$) in equation (38):

$$n(\infty) = \sqrt{1+\frac{E_d}{E_o}} \tag{42}$$

where, $\varepsilon_{\propto 1} = n(\infty)^2$ is the Static dielectric constant and it takes account of electronic, ionic and space charge polarizations altogether. The experimental refractive data can also be used to estimatethe carrier concentration to effective mass ratio using the following equation [39,42]:

$$n(\lambda)^2 = \varepsilon_{\propto 2} - \left(\frac{e^2}{\pi c^2 \epsilon_0}\right)\left(\frac{N}{m^*}\right)\lambda^2 \tag{43}$$

Figure 11(a) shows $n(\lambda)^2$ as function of λ^2 . Strong dispersive behaviour can be observed in high energy (short wavelength) region. At energy larger than the band gap, the incident photon iscompletely absorbed and thereby the electromagnetic wave cannot propagate through the thin film.In the low energy (long wavelength) region, normal dispersion is observed and the extrapolation ofthe low energy slope to $\lambda^2=0$ provides $\varepsilon_{\propto 2}$ which corresponds to the electronic dielectric constant at high frequency region since, only electrons can respond to the high energy photon through inter band optical transition. The values of $\varepsilon_{\propto 1}$ and $\varepsilon_{\propto 2}$ are listed in Table 4.

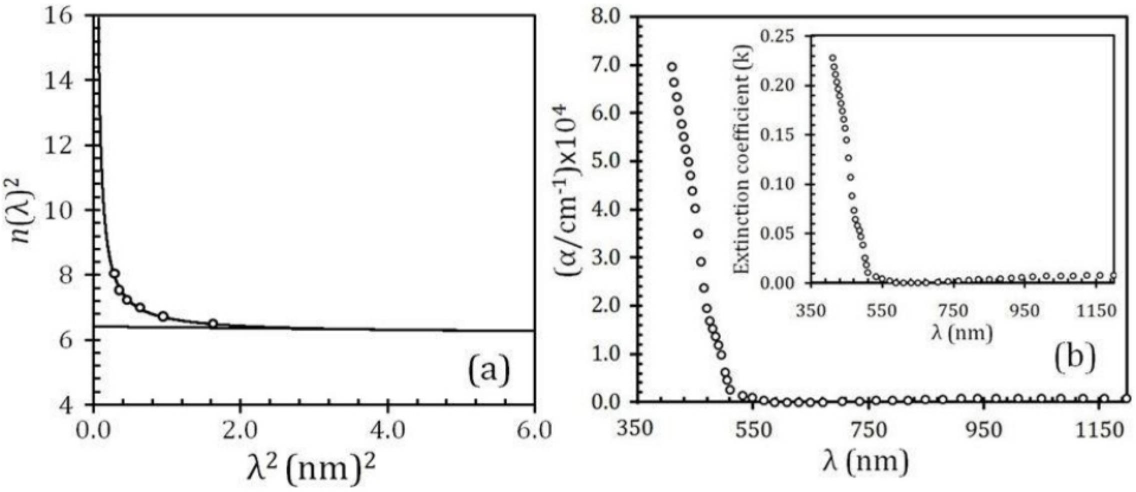

Figure 11. (a) Dispersion of dielectric constant, (b) Absorption coefficient α as a function of incident photon wavelength λ and the inset shows the corresponding extinction coefficient spectrum.

Table 4. Electro-optical parameters for ZnSe thin film.

Electro optical parameter	value
Optical Energy gap, E_g (eV)	2.64
Oscillator Energy, E_o (eV)	4.72
Dispersion Energy, E_d (eV)	24.95
The energy Ratio, $E_o/2E_g$	0.90
The momentum, M_2	5.28
The momentum, M_3	0.23
The static Refractive Index, $n(\infty)$	2.53
The dielectric constant, $\varepsilon_{\propto 1}$	6.28
The dielectric constant, $\varepsilon_{\propto 2}$	6.41

From the transmittance data, absorption coefficient and extinction coefficient have been calculated. Absorbance is related to absorption coefficient (by following relation [42]:

$$\alpha = \frac{1}{d}\ln(A) \tag{44}$$

Here, *A* is the absorbance and *d* is the thickness of the thin film. Absorbance can be calculated from the *Ta* envelope obtained from the experimental transmittance data (Figure 8(b)), using the following equations [38]:

$$A = \frac{B+\left[B^2+2qT_\alpha(1-R_2R_3)\right]^{\frac{1}{2}}}{q} \tag{45}$$

$$B = (R_1-1)(R_2-1)(R_3-1); \tag{46}$$

$$q = 2T_\alpha(R_1R_2-R_1R_3-R_1R_2R_3) \tag{47}$$

where, R_1, R_2 and R_3 are the reflectance values of the air-film, film-substrate and substrate-air interfaces respectively and are given by following equations:

$$R_1 = \left[\frac{1-n(\lambda)}{1+n(\lambda)}\right]^2; R_2 = \left[\frac{n(\lambda)-S(\lambda)}{n(\lambda)+S(\lambda)}\right]^2; R_3 = \left[\frac{S(\lambda)-1}{S(\lambda)+1}\right]^2 \tag{48}$$

Here, $n(\lambda)$ and $S(\lambda)$ are the refractive indexes of the thin film and the glass substrate respectively. Figure 11(b) shows the absorption coefficient as function of wavelength calculated using equations (44–48).

From Figure 11(b), the absorption edge can be found to occur around 510 nm. This wavelength is slightly smaller than the previously reported value for ZnSe thin film [6]. This discrepancy could be an indication of better crystallinity associated with more uniform and possibly coherent crystallites in case of the present sample when compared to the previous report. However, in order to establish such argument on a solid ground it is rather imperative to conduct optical and structural study on a series of thin film samples having different thermal histories prepared under same experimental setup, which is underway. The absorption coefficient is directly proportional to the extinction coefficient (k) by following relation:

$$k = \frac{\alpha\lambda}{4\pi} \tag{49}$$

The inset of Figure 11(b) shows the extinction coefficient as function wavelength. Extinction coefficient has significant practical importance since it represents the loss of electromagnetic wave inside the thin film of interest. From Figure 11(b) it is clear that this thin film can function as a good optical material at relatively low wavelengths (down to 510 nm) of the visible spectrum.

Another important parameter to characterize a semiconductor is its band gap (E_g) which has been estimated from the energy dependent absorption coefficient data at the absorption edge using the Tauc's relation [43] as follows:

$$\alpha\mathrm{h}\nu = \alpha_{\mathrm{o}}(\mathrm{h}\nu - E_g)^m \tag{50}$$

Here, α is the absorption coefficient, E_g is the band gap, α_o is the band tailing parameter and m is the power factor of the transition mode which depends on crystal structure of the materials and the type of electronic transition that leads to formation of absorption edge in the optical transmission spectrum. The values of m for indirect allowed, direct allowed, indirect forbidden and direct forbidden transitions are 2, 0.5, 1.5 and 3 respectively. Now equation (50) can be slightly rearranged as: $\ln(\alpha h\nu) = \ln\alpha_o + m \cdot \ln(h\nu - E_g)$. Hence, the slope of the plot $\ln(\alpha h\nu)$ vs. $\ln(h\nu - E_g)$ around the absorption edge gives the value of m which has been found to be $m = 0.508 \approx 0.5$ from the linearly fitted line-equation shown in the inset-plot of Figure 12(a). Therefore, the Tauc's relation can safely be written for the present sample as:

$$(\alpha h\nu)^2 = \alpha_o(h\nu - E_g) \tag{51}$$

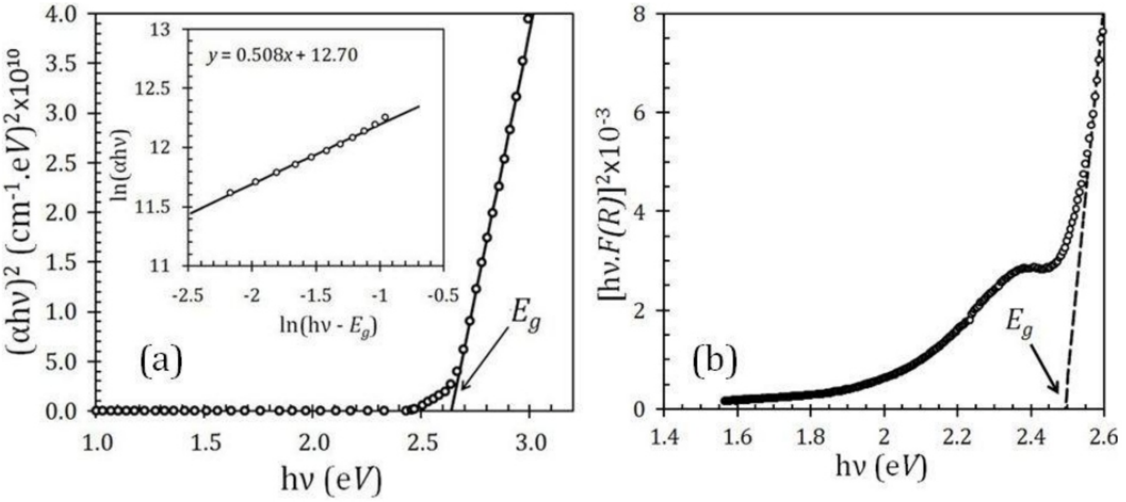

Figure 12. (a) The Tauc's plot for the determination optical band gap. The inset shows $\ln(\alpha h\nu)$ vs. $\ln(h\nu - E_g)$ plot along with the equation for linear fit, (b) The Tauc's plot for the determination optical band gap of powder using the Kubelka-Munk function.

Figure 12(a) shows the plot of $(\alpha h\nu)^2$ as a function of photon energy also known as the Tauc's plot. From the plot, optical band gap can now be determined firstly by fitting a straight line around the absorption edge of the plot and then by estimating the point of intersection of the fitted line with the -axis at $(\alpha h\nu)^2 = 0$. The band gap obtained from the Tauc's plot has been found to be 2.64 eV which appears to be a quite reasonable value when compared with previously reported results [2,6,12,13,16,20,23].

Moreover, it is rather interesting to compare the band gap required for optical absorption of the deposited film with that of the pulverized source powder. In order to determine the band gap of opaque powder material for direct transition, it is a common practice to use the Tauc's relation givenby equation (51) provided that the absorption coefficient is now given by the following equation [44]:

$$\alpha = \tau_o F(R)/(2v_p) \tag{52}$$

where, τ_o is the scattering coefficient, v_p is the volume fraction of the absorbing species and $F(R)$ is the Kubelka-Munk function given by:

$$F(R) = (1 - R)^2/(2R) \tag{53}$$

where, R is the measured diffuse reflectance of powder sample. Now, neglecting the dependence of τ_o and v_p on incident wavelength, the absorption coefficient can be written as;

$$\alpha = \{\tau_o/(2v_p)\} \cdot F(R) = A \cdot F(R) \tag{54}$$

Here, A is a constant. Therefore, combining equation (51) and (54), we get:

$$[\mathrm{h}\nu \cdot F(R)]^2 = \alpha_o^{/}(\mathrm{h}\nu - E_g) \tag{55}$$

where, $\alpha_o^{/}$ is a constant. According to equation (55), at the absorption edge, $[\mathrm{h}\nu \cdot F(R)]^2$ should vary linearly with (hν) and the optical band gap could be obtained by linearly extrapolating the most steep, linear portion of $[\mathrm{h}\nu \cdot F(R)]^2$ vs. (hν) plot to $[\mathrm{h}\nu \cdot F(R)]^2 = 0$ where, $\mathrm{h}\nu = E_g$. Figure 12(b) depicts such a plot for our ZnSe source powder, where the diffuse reflectance data were taken within a wavelength range of 200–600 nm at 1 nm interval. From the extrapolation represented by the dotted line, it can be found that our powdered ZnSe source has an optical band gap of 2.5 e*V* for deposited ZnSe thin film by 0.14 e *V* when compared to that of the source powder. Similar behaviour was reported for thermally evaporated ZnSe thin films from bulk ZnSe [6], which could bequalitatively comprehended in terms of 3D quantum confinement effect associated withcrystal/particle size reduction to nano or below nano-scale as a first approximation. The basic 3Dquantum confinement model is actually based on effective mass approximation relation for quantumdots given by:

$$\Delta E_g = E_g^{nano} - E_g^{bulk} = \{\mathrm{h}^2/(2m_o D^2)\} \cdot (1/m_e^* + 1/m_h^*) - \{(3.6\mathrm{e}^2)/(4\pi\epsilon_r\epsilon_o D)\} \tag{56}$$

where, ΔE_g is the blue shift in band gap energy; h, e, m_o, m_e^*, m_h^*, ϵ_r, ϵ_o and D are the Plank's constant, electron charge, electron rest mass, effective mass of electron, effective mass of hole, relative permittivity of the medium, vacuum permittivity and particle/crystallite size respectively. The above equation clearly entails for a blue shift in band gap with a decrement in crystallite size.Having said that, a careful comparison between Figure 1(a) and 1(b) reveals that the actual film issubjected to a significant peak broadening in relation to that of the source powder. As a matter of fact,the instrumental broadening is around 80% of the observed peak width in case of our source powderindicating only a minute size broadening effect. Hence, the crystal size of the source ZnSe obtainedfrom the standard Debye-Scherrer model comes out to be 321 nm, which is way beyond themaximum reliable size-limit (100 nm) that can be calculated from the model itself, suggesting thatthe average particle/crystallite size of the source powder has to be above 100 nm. Henceforth, wecould safely infer that the reduction in particle/crystallite size from above 100 nm to a range of2–26 nm after the film deposition is the most conceivable catalyst at hand to induce the observedblue shift in band gap in our case.

Additionally, it has been shown by K. Tanaka [45] that there exits an approximate relation between the band gap and oscillator energy given by the form: $E_o/2E_g{\sim}1$. For our sample this ratio reported to fall within an excellent range of 1–1.04 for pulsed laser annealed ZnSe thin films [6] the standard WDD model analysis by Gullu et al. [23] indicated this ratio to vary from 0.5 to 0.6 forTVD ZnSe thin film annealed at 300 °C to 500 °C. From a more contemporary study on TVD ZnSe thin film any post-deposition annealing treatment [12], this energy ratio can be calculated to be around 0.7. In view of the above findings, we can only state that for our vacuum annealed TVDthin film sample, the energy ratio appears to be close to 1. However, the observed deviation fromunity might be associated with some structural and morphological disorders, which could lead to adistribution of oscillator energies instead of a single-valued one as originally proposed by the idealWDD model.

It is evident from the detailed structural and optical study that our thermal vapour deposited ZnSe thin film is structurally sound regardless the quality of the substrate used. All the structural andoptical parameters appear to be rather reasonable and even sometimes better. The low opticaldispersion energy and optical moment as well as the observed β_o value indicate high degree of crystallinity. This observation is further supported by the combined SEM and XRD analysis whichindicate the possible absence of interfaces within the particles formed from defect ordering.

4. Conclusion

ZnSe thin film was prepared on a readily available soda-lime glass substrate by thermal evaporation technique. Detailed structural characterization of ZnSe thin film using XRD wasreported. X-ray diffraction data confirmed the polycrystalline nature of the film with (111), (220) and(311) peaks having zincblende structure. Texture analysis of ZnSe thin film was performed by pole figure measurement. (111) plane showed strong orientation around 15°and 60°with substratenormal and also explained some anomalous variations observed in the relative intensity ratios of thediffraction peaks of the thin film. Crystallite size was estimated from the width of the diffractionpeaks using Debye-Scherrer, Size-Strain plot, Williamson-Hall, modified Williamson-Hall model and the so called approximation model based on the separate contribution from the size and strain broadening. The crystallite size was found to fall within a narrow range of 12–17 nm depending on the model used which exhibited good agreement with the particle size range of 10–18 nm obtained from SEM image analysis. This is an indication that most of the observed particles arecrystallographically coherent. The change of lattice volume in thin film is attributed to local latticestrain. The deviation of average internal strain obtained from W-H method by $\sim 10^{-3}$ from that of the local lattice strain obtained from Nelson-Riley relation is believed to be associated with thin filmstrain relaxation through micro-crack formation. The other mechanical and thermodynamicparameters such as stress, dislocation density and anisotropic energy density were reported. The filmthickness estimated using Swanepoel's envelope method was 374.9 nm which exhibited goodagreement with the thickness obtained from SEM image within the experimental standard deviation.Refractive index data exhibited strong dispersive behaviour in the short wavelength region,suggesting optical absorption in the short wavelength range. The most important parameter opticalband gap was estimated to be 2.64 eV. WDD single oscillator model was used to estimate dispersionenergy and Oscillator energy from the low energy refractive index data. Low dispersion energy andsmaller optical moments suggest that better crystallinity has been obtained in the present samplewhich is also supported by the observed crystallographic coherency of individual particles obtainedfrom crystal-size measurement data. The observed blue-shift in optical transition energy of the thin film by 0.14 eV with respect to that of the source powder was attributed to quantum size effect.

Conflict of Interest

The authors declare that there is no conflict of interest in this paper.

Reference

1. Mehta C, Saini GSS, Abbas JM, et al. (2009) Effect of deposition parameters on structural, optical and electrical properties of nanocrystalline ZnSe thin films. Appl Surf Sci 256: 608–614.

2. Venkatachalam S, Jeyachandran YL, Sureshkumar P, et al. (2007) Characterization of vacuum evaporated ZnSe thin films. Mater Charact 58: 794–799.

3. Xia M, Liu C, Zhao Z, et al. (2015) Formation and optical properties of ZnSe and ZnS nanocrystals in glasses. J Non-Cryst Solids 429: 79–82.

4. Kalita PKR, Sarma BK, Das HL (2000) Structural characterization of vacuum evaporated ZnSe thin films. B Mater Sci 23: 313–317.

5. Subbaiah YPV, Prathap P, Devika M, et al. (2005) Close-spaced evaporated ZnSe films:Preparation and characterization. Physica B 365: 240–246.

6. Hassanien AS, Aly KA, Akl AA (2016) Study of optical properties of thermally evaporated ZnSe thin films annealed at different pulsed laser powers. J Alloy Compd 685: 733–742.

7. Lokhande CD, Patil PS, Tributsch H, et al. (1998) ZnSe thin films by chemical bath deposition method. Sol Energ Mat Sol C 55: 379–393.

8. Sagadevan S, Das I (2016) Chemical bath deposition (CBD) of zinc selenide (ZnSe) thin films and characterisation. Aust J Mech Eng 1–6.

9. Patidar D, Rathore KS, Saxena NS, et al. (2008) Determination of optical and electrical properties of ZnSe thin films. J Mod Optic 55: 3041–3047.

10. Mittal V, Sessions NP, Wilkinson JS, et al. (2017) Optical quality ZnSe films and low loss wave guides on Si substrates for mid-infrared. Opt Mater Express 7: 712–725.

11. Ismail ME, Shaaban ER, Hagary ME (2016) A new method for calculating the refractive index of semiconductor thin films retrieved from their transmission spectra. J Alloy Compd 663: 20–29.

12. Desai HN, Dhimmar JM, Modi BP (2016) Optical and dispersion analysis of Zinc Selenide thin film. Mater Today Proc 3: 1650–1657.

13. Khan NA, Saleem A, Satti AR, et al. (2016) Post deposition annealing: a route to band gap tailoring of ZnSe thin films. J Mater Sci-Mater El 27: 9755–9760.

14. Yuvaraj D, Kumar RR, Selvan VT, et al. (2014) Growth of ZnSe nano and microstructures at high vacuum by thermal evaporation. Appl Nanosci 4: 469–475.

15. Lohar GM, Shinde SK, Fulari VJ (2014) Structural, morphological, optical and photoluminescent properties of spray-deposited ZnSe thin film. J Semiconduct 35: 113001.

16. Zhang X, Wang D, Beres M, et al. (2013) Zincblende-wurtzite phase transformation of ZnSe films by pulsed laser deposition with nitrogen doping. Appl Phys Lett 103: 082111.

17. Khanand TM, BiBi T (2012) Compatibility and optoelectronic of ZnSe nano crystalline thin film. Chinese Phys B 21: 3097303.

18. Aqili A, Ali Z, Hussain Z (2012) Optical and structural properties of silver doped ZnSe thin films prepared by CSS and ion exchange process. Thin Film Solar Technology IV, Proc. Of SPIE 8470:84700H.

19. Khairnar U, Behere S, Pawar P (2012) Optical properties of polycrystalline Zinc Selenide thin films. Mater Sci Appl 3: 36–40.

20. Ashraf M, Akhtar SMJ, Khan AF, et al. (2011) Effect of annealing on structural and optoelectronic properties of nanostructured ZnSe thin films. J Alloy Compd 509: 2414–2419.

21. Ismail ME, Hagary ME, Shaab ER, et al. (2012) Microstructure and optical studies of electron beam evaporated ZnSe1−xTex nanocrystalline thin films. J Alloy Compd 532: 16–24.

22. Ahamed MGSB, Nagarethinam VS, Balu AR, et al. (2010) Influence of substrate temperature on the properties of electron beam evaporated ZnSe films. Cryst Res Technol 45: 421–426.

23. Güllü HH, Coşkun E, Parlak M (2015) Investigation of optical parameters of thermally evaporated ZnSe thin films. Phys Status Solidi C 12: 1224–1228.

24. Kalita A, Kalita MPC (2017) Williamson-Hall analysis and optical properties of small sized ZnO nanocrystals. Physica E 92: 36–40.

25. Kumar BR, Hymavathi B (2017) X-ray peak profile analysis of solid-state sintered alumina doped zinc oxide ceramics by Williamson-Hall and size-strain plot methods. J Asian Ceram Soc 5: 94–103.

26. Prabhu YT, Rao KV, Kumar VSS, et al. (2014) X-Ray analysis by Williamson-Hall and sizestrain slot methods of ZnO Nanoparticles with fuel variation. World J Nano Sci Eng 4: 21–28.

27. Garg P, Rai R, Singh BK, et al. (2014) Structural characterization of "as-deposited" cesium iodide films studied by X-ray diffraction and transmission electron microscopy techniques. Nucl Instrum Meth A 736: 128–134.

28. Monshi A, Foroughi MR, Monshi MR (2012) Modified Scherrer equation to estimate more accurately nano-crystallite size using XRD. World J Nano Sci Eng 2: 154–160.

29. Sivasankaran S, Sivaprasad K, Narayanasamy R, et al. (2011) X-ray peak broadening analysis of AA 6061100−x–x wt.% Al2O3 nanocomposite prepared by mechanical alloying. Mater Charact 62: 661–672.

30. Zak AK, Aulmajid WH (2011) X-ray analysis of ZnO nanoparticles by Williamson-Hall and Size strain plot method. Solid State Sci 13: 251–256.

31. Bushroa AR, Rahbari RG, Masjuki HH, et al. (2012) Approximation of crystallite size and the microstrain via XRD line broadening analysis in TiSiN thin films. Vacuum 86: 1107–1112.

32. Ou K, Wang S, Wan G, et al. (2017) Structural, morphological and optical properties of ZnO films by thermal oxidation of ZnSe films. Thin Solid Films 634: 51–55.

33. Nelson JB, Riley PD (1945) An experimental investigation of extrapolation methods in the derivation of accurate unit-cell dimensions of crystals. Proc Phys Soc 57: 160–177.

34. Kim MJ, Lee SH, Kim HT, et al. (2013) Physical properties of ZnSe thin films depending on the process parameters. Mol Cryst Liq Cryst 586: 129–137.

35. Morales M, Chateigner D, Lutterotti L (2009) X-ray textural and microstructural characterizations by using the combined analysis approach for the optical optimisation of microand nano-structured thin films. Thin Solid Films 517: 6264–6270.

36. Rizzoa A, Taglientea MA, Caneveb L, et al. (2000) The influence of the momentum transfer on the structural and optical properties of ZnSe thin films prepared by r.f. magnetron sputtering.Thin Solid Films 368: 8–14.

37. Swanepoel R (1983) Determination of the thickness and optical constants of amorphous silicon. J Phys E Sci Instrum 16: 1214–1222.

38. Dahshan A, Amer HH, Aly KA (2008) Compositional dependence of the optical constants of amorphous GexAs20Se80−x thin films. J Phys D Appl Phys 41: 215401.

39. Aly KA (2010) Optical band gap and refractive index dispersion parameters of AsxSe70Te30−x (0 ≤ x ≤ 30 at.%) amorphous films. Appl Phys A-Mater 99: 913–919.

40. Wemple SH, DeDomenico M (1971) Behaviour of electronic dielectric constant in covalent and ionic materials. Phys Rev B 3: 1338–1351.

41. Wemple SH, DiDomenico M (1969) Optical dispersion and the structure of solids. Phys Rev Lett 23: 1156–1160.

42. Connell GAN, Lewis AJ (1973) Comments on the evidence for sharp and gradual optical absorption edges in amorphous germanium. Phys Status Solidi B 60: 291–298.

43. Tauc J (1974) Amorphous and Liquid Semiconductors, New York: Plenum Publishing Corporation.
44. Venugopal B, Nandan B, Ayyachamy A, et al. (2014) Influence of manganese ions in the band gap of tin oxide nanoparticles: structure, microstructure and optical studies. RSC Adv 4: 6141–6150.
45. Tanaka K (1980) Optical properties and photoinduced changes in amorphous AsS films. Thin Solid Films 66: 271–279.

Instructions for Authors

Essentials for Publishing in this Journal

1 Submitted articles should not have been previously published or be currently under consideration for publication elsewhere.

2 Conference papers may only be submitted if the paper has been completely re-written (taken to mean more than 50%) and the author has cleared any necessary permission with the copyright owner if it has been previously copyrighted.

3 All our articles are refereed through a double-blind process.

4 All authors must declare they have read and agreed to the content of the submitted article and must sign a declaration correspond to the originality of the article.

Submission Process

All articles for this journal must be submitted using our online submissions system. http://enrichedpub.com/ . Please use the Submit Your Article link in the Author Service area.

Manuscript Guidelines

The instructions to authors about the article preparation for publication in the Manuscripts are submitted online, through the e-Ur (Electronic editing) system, developed by **Enriched Publications Pvt. Ltd**. The article should contain the abstract with keywords, introduction, body, conclusion, references and the summary in English language (without heading and subheading enumeration). The article length should not exceed 16 pages of A4 paper format.

Title

The title should be informative. It is in both Journal's and author's best interest to use terms suitable. For indexing and word search. If there are no such terms in the title, the author is strongly advised to add a subtitle. The title should be given in English as well. The titles precede the abstract and the summary in an appropriate language.

Letterhead Title

The letterhead title is given at a top of each page for easier identification of article copies in an Electronic form in particular. It contains the author's surname and first name initial .article title, journal title and collation (year, volume, and issue, first and last page). The journal and article titles can be given in a shortened form.

Author's Name

Full name(s) of author(s) should be used. It is advisable to give the middle initial. Names are given in their original form.

Contact Details

The postal address or the e-mail address of the author (usually of the first one if there are more Authors) is given in the footnote at the bottom of the first page.

Type of Articles

Classification of articles is a duty of the editorial staff and is of special importance. Referees and the members of the editorial staff, or section editors, can propose a category, but the editor-in-chief has the sole responsibility for their classification. Journal articles are classified as follows:

Scientific articles:

1. Original scientific paper (giving the previously unpublished results of the author's own research based on management methods).
2. Survey paper (giving an original, detailed and critical view of a research problem or an area to which the author has made a contribution visible through his self-citation);
3. Short or preliminary communication (original management paper of full format but of a smaller extent or of a preliminary character);
4. Scientific critique or forum (discussion on a particular scientific topic, based exclusively on management argumentation) and commentaries. Exceptionally, in particular areas, a scientific paper in the Journal can be in a form of a monograph or a critical edition of scientific data (historical, archival, lexicographic, bibliographic, data survey, etc.) which were unknown or hardly accessible for scientific research.

Professional articles:

1. Professional paper (contribution offering experience useful for improvement of professional practice but not necessarily based on scientific methods);
2. Informative contribution (editorial, commentary, etc.);
3. Review (of a book, software, case study, scientific event, etc.)

Language

The article should be in English. The grammar and style of the article should be of good quality. The systematized text should be without abbreviations (except standard ones). All measurements must be in SI units. The sequence of formulae is denoted in Arabic numerals in parentheses on the right-hand side.

Abstract and Summary

An abstract is a concise informative presentation of the article content for fast and accurate Evaluation of its relevance. It is both in the Editorial Office's and the author's best interest for an abstract to contain terms often used for indexing and article search. The abstract describes the purpose of the study and the methods, outlines the findings and state the conclusions. A 100- to 250-Word abstract should be placed between the title and the keywords with the body text to follow. Besides an abstract are advised to have a summary in English, at the end of the article, after the Reference list. The summary should be structured and long up to 1/10 of the article length (it is more extensive than the abstract).

Keywords

Keywords are terms or phrases showing adequately the article content for indexing and search purposes. They should be allocated heaving in mind widely accepted international sources (index, dictionary or thesaurus), such as the Web of Science keyword list for science in general. The higher their usage frequency is the better. Up to 10 keywords immediately follow the abstract and the summary, in respective languages.

Acknowledgements

The name and the number of the project or programmed within which the article was realized is given in a separate note at the bottom of the first page together with the name of the institution which financially supported the project or programmed.

Tables and Illustrations

All the captions should be in the original language as well as in English, together with the texts in illustrations if possible. Tables are typed in the same style as the text and are denoted by numerals at the top. Photographs and drawings, placed appropriately in the text, should be clear, precise and suitable for reproduction. Drawings should be created in Word or Corel.

Citation in the Text

Citation in the text must be uniform. When citing references in the text, use the reference number set in square brackets from the Reference list at the end of the article.

Footnotes

Footnotes are given at the bottom of the page with the text they refer to. They can contain less relevant details, additional explanations or used sources (e.g. scientific material, manuals). They cannot replace the cited literature.

The article should be accompanied with a cover letter with the information about the author(s): surname, middle initial, first name, and citizen personal number, rank, title, e-mail address, and affiliation address, home address including municipality, phone number in the office and at home (or a mobile phone number). The cover letter should state the type of the article and tell which illustrations are original and which are not.